

Monitoring Fireline Construction in Near Real-Time with Sentinel-1

by

Lukas Schreiber

B.Sc., Delft University of Technology, 2016

A THESIS SUBMITTED IN PARTIAL FULFILLMENT OF
THE REQUIREMENTS FOR THE DEGREE OF

MASTER OF SCIENCE

in

THE FACULTY OF GRADUATE AND POSTDOCTORAL STUDIES
(Forestry)

THE UNIVERSITY OF BRITISH COLUMBIA
(Vancouver)

August 2019

© Lukas Schreiber, 2019

The following individuals certify that they have read, and recommend to the Faculty of Graduate and Postdoctoral Studies for acceptance, a thesis entitled:

Monitoring Fireline Construction in Near Real-Time with Sentinel-1

submitted by Lukas Schreiber in partial fulfillment of the requirements for
the degree of Master of Science
in Forestry

Examining Committee:

Nicholas Coops, Forest Resources Management
Supervisor

Lori Daniels, Forest and Conservation Sciences
Supervisory Committee Member

William Parkinson, Urthecast Corp.
Supervisory Committee Member

Ken Day, Alex Fraser Research Forest (retired)
Supervisory Committee Member

Sarah Gergel, Forest and Conservation Sciences
Additional Examiner

Additional Supervisory Committee Members:

Supervisory Committee Member

Supervisory Committee Member

Abstract

Near real-time mapping of anthropogenic linear networks (e.g. roads, seismic lines and fireguards) in forests has a range of applications including monitoring rapid management responses to disturbances such as fire. Synthetic aperture radar imagery is well suited for near real time monitoring because microwaves penetrate clouds and smoke, and satellite images are acquired weekly in many parts of the world, assuring regular coverage.

In this study, we created maps of fireguard networks constructed during the 2017 wildfires in Alex Fraser Research Forest in interior British Columbia, Canada based on Sentinel-1 SAR image time series and Sentinel-2 image pairs.

I developed two methods to summarize the Sentinel-1 backscatter time series in a single summary raster suitable for human interpretation in Google Earth Engine. The first method is to fit a trend line to the backscatter time series for each pixel, and display the value of this line at the start and end of the observation window in red and green. The second is to fit a single-step function and display the left and right tail values along with the R^2 value of the fit as red, green and blue values.

I assessed the utility of these summary images for manual delineation of fireguard networks by simulating the accuracy and timeliness of fireguard detection based on acquisition in near real-time. For reference, I compared these methods with a straightforward before-after analysis of Sentinel-2 multispectral images and with ground truth maps.

From the trend line and step function summary images, interpreters detected 22–41% and 24–55% of fireguard length respectively while delineation from multispectral imagery attained a detection rate of 84–86%. Delineation from Sentinel-2 images was most precise with an average deviation of 5–6 metres from the ground truth, followed by the trend image with 8–15 metres deviation and the step image with 11–16 metres. In the best case, a change was detected based on a step image within 6 days. The developed method can be used to monitor linear feature construction where more accurate methods are unavailable.

Lay summary

To respond effectively to forest disturbance such as wildfires, windthrow, or logging,

it is essential to assess the extent and structure of a disturbance in a timely manner.

Synthetic aperture imagery from the European Space Agency's two Sentinel-1 satellites is well suited for timely disturbance monitoring because it is acquired every six days, and the radar waves are not obstructed by clouds. This thesis is a case study of how a time series of Sentinel-1 images could have been used to monitor how firefighters cleared fireguards to contain four wildfires that burned near Williams Lake in central British Columbia in 2017.

For the study I condensed the time series of multiple SAR images to a single red-green-blue image. This single image served as a summary of the time series of images and was given to a human interpreter who used it to monitor fireguard construction.

Preface

This study forms part of a larger research project called Advanced Earth Observation Technologies, funded by the Consortium for Aerospace Research and Innovation in Canada (CARIC) under the project number CARIC MDO-714_TRL4+”. It was conducted in liaison with CARIC, UrtheCast Corp., 3VGeomatics Inc, Imstrat Corporation, The University of British Columbia, and University of Victoria. The topic was initially given as “Advanced research on Optical / SAR combinations as they relate to Forestry and Agriculture applications” and later narrowed down to SAR applications for forestry.

The research presented in this thesis was devised and conducted by myself. The supervisory committee provided valuable advice and comments on subsequent drafts of my thesis. My supervisor helped edit the thesis.

Table of contents

Abstract	iii
Lay summary	v
Preface.....	vi
Table of contents.....	vii
List of tables	xii
List of figures	xii
Glossary and abbreviations	xvi
List of symbols	xxiii
Acknowledgements	xxv
Dedication	xxvii
Chapter 1: Background	1
1.1 Introduction	1
1.2 Basics of synthetic aperture radar	4
1.2.1 C-band microwaves	4
1.2.2 SAR imaging geometry.....	7
1.2.3 SAR images of fireguards	11

1.3	Wildland fire fighting.....	14
1.4	SAR and landscape monitoring	16
1.5	Planetary-scale data analysis in Google Earth Engine.....	17
1.6	The mission: visualizing SAR time series	18
	Chapter 2: The science of fireline monitoring.....	19
2.1	Materials	19
2.1.1	Study area.....	19
2.1.2	Remotely Sensed Images	23
2.1.3	Ground Truth	26
2.2	Methods.....	27
2.2.1	Overview.....	27
2.2.2	Preparing the SAR time series	30
2.2.3	Patterns in the SAR time series.....	34
2.2.4	Generating the trend composite image.....	35
2.2.5	Generating the step composite image.....	37
2.2.6	Sentinel-2 images	40
2.2.7	Manual image interpretation	40

2.2.8 Accuracy Assessment	44
2.3 Results	49
2.3.1 Example maps	49
2.3.2 Fire severity	55
2.3.3 Detection success	57
2.3.4 Spatial accuracy.....	57
2.3.5 What influenced detection rates?	61
2.3.6 How quickly were fireguards detected?	66
2.3.7 How much time was required for delineation?	70
2.4 Discussion	71
2.4.1 Accuracy	71
2.4.2 Fire severity	72
2.4.3 What influenced detection rates?	72
Chapter 3: Conclusion	75
3.1 Answers to the research questions	75
3.2 Limitations	77
3.3 Potential applications	81

3.4	Recommendations	82
3.5	Designing a landscape monitoring system based on SAR time series.....	84
3.5.1	Dialog with users	84
3.5.2	Definition of requirements.....	84
3.5.3	Concept design of the monitoring system	85
3.5.4	Building the monitoring system.....	87
3.5.5	Testing	88
3.5.6	Delineation	88
3.5.7	Accuracy assessment	89
	References	90
	Appendices	97
Appendix A	Literature table.....	97
Appendix B	Image interpreter's instructions	106
Appendix C	Image interpreter's logs	113
Appendix D	Image interpreter's maps	120
Appendix E	Slope steepness data	128

List of tables

Table 1. Mapping of linear feature categories in the Shapefile provided by AFRF onto the two categories used in the study	26
Table 2. Interpreter experience and spatial division of interpretation tasks	41

List of figures

Figure 1. Structure of electromagnetic waves	4
Figure 2. Polarization of electromagnetic waves	6
Figure 3. Operating principle of side-looking radar	7
Figure 4. Types of reflectors of radar waves	8
Figure 5. Terrain relief effects	9
Figure 6. Ascending and descending orbits and orbital inclination with right-looking SAR.....	10
Figure 7. SAR reflectance model of a north-south aligned fireguard.....	13
Figure 8. Fire suppression and the fire triangle	14
Figure 9. Photograph of a fireguard with backfire.....	15
Figure 10. Map of the study area near Williams Lake, British Columbia	20
Figure 11. Climate normals for Spokin Lake weather station, about 30 km south of AFRF	21
Figure 12. 2017 weather summary for Spokin Lake weather station, about 30 km south of AFRF	20
Figure 13. Progression of the Prouton Lake fires over time as seen by Sentinel-2..	23

Figure 14. Illustration of pixel-based time series compositing	27
Figure 15. Change detection flowchart	29
Figure 16. Histograms of one VV-image clipped to the study area.....	31
Figure 17. Geometry of ascending/descending pass filtering.....	32
Figure 18. Composite images resulting from different types of ascending/descending pass filtering	32
Figure 19. Graph of fitting a trend line to a time series.....	36
Figure 20. Graph of fitting a single-step function to a time series	39
Figure 21. Timeline of imagery employed for fireguard delineation	43
Figure 22. Example detail of how the algorithm decided which lines on the interpreters' maps corresponded to real new features on the ground and which were interpretation artefacts.....	46
Figure 23. Example detail of how the algorithm decided what fireguard segments were delineated and what segments were missed.....	46
Figure 24. Example detail showing how the 'correct' lines were split into ≤ 10 m segments and how the distance from the reference fireguard map was calculated ...	48
Figure 25. Example of composite images shown to Dan and the map of linear features he produced	52

Figure 26. Example of the trend composite image, step composite image and multispectral image pair for disturbance interpretation zoomed into a small area ..	54
Figure 27. Fire severity map compared to step composite image	56
Figure 28. Column chart of detection accuracies	58
Figure 29. Crosshair plots of the offsets of detected fireguard center geometry from the reference geometry measured with GPS.	60
Figure 30. Examples of situations that led to delineation of linear features that did not correspond to firelines	62
Figure 31. Spider plots of deviation success as a function of fireguard direction....	64
Figure 32. Detection accuracy stratified by slope steepness bins for each combination of AoI and image interpreter.....	65
Figure 33. Timeline analysis of the detection efforts for a small area 1	67
Figure 34. Timeline analysis of the detection efforts for a small area 2	69
Figure 35. Bar chart of the average time it took an interpreter to create a map of new features from on change composite image (or before-after pair of multispectral images in the case of Erin).....	70

No part of Figures 1, 3, 4 and 5 may be reproduced, stored in a retrieval system or transmitted in any form or by any means, electronic, mechanical, photocopying, recording, scanning or otherwise, except as permitted under Sections 107 or 108 of the United States Copyright Act, without either the prior written permission of the Publisher, or authorization through payment of the appropriate per-copy fee to the Copyright clearance Center, 222 Rosewood Drive, Danvers, MA 01923, (978) 750-8400, fax (978) 750-4470. Requests to the Publisher for permission should be addressed to the Permissions Department, John Wiley & Sons, Inc., 605 Third Avenue, New York, NY 10158-0012, (212) 850-6008, E-Mail: PERMREQ@WILEY.COM. To order books or for customer service call 1-800-CALL-WILEY (225-5945)

Glossary and abbreviations

a.k.a.	also known as
AFRF	Alex Fraser Research Forest, one of UBC's research forests
Airbus	a European aerospace and defence company
ALOS	Advanced Land Observing Satellite, a Japanese satellite with an L-band SAR instrument called PALSAR on board
ALS	airbourne laser scanning, aircraft-mounted LiDAR for three-dimensional terrain scanning
AoI	area of interest
ascending pass	satellite moving roughly South to North
azimuth direction	the moving direction of the satellite (Lillesand & Kiefer, 2000, p. 621)
backscatter	the portion of the radar signal sent out by a satellite which is reflected and received by that satellite (European Space Agency, n.d.-b)
BFAST	Breaks for Additive Season and Trend, a time series decomposition tool (Verbesselt, Zeileis, & Herold, 2012)

biogeoclimatic zone	class of geographically related ecosystems (Pojar, Klinka, & Meidinger, 1987)
CARIC	Consortium for Aerospace Research and Innovation in Canada
C-band	band of microwaves with wavelengths between 37.5 mm and 75 mm (Lillesand & Kiefer, 2000, p. 637)
commission error	proportion of false positives among delineated lines
corner reflector	landscape feature that reflects microwaves on a horizontal and a vertical surface (Lillesand & Kiefer, 2000, p. 646)
DEM	digital elevation model
descending pass	satellite moving roughly North to South
detection rate	proportion of fireguards that were detected (complement to omission error)
duff	a.k.a. forest floor, the layer of dead plant parts such as leaves, bark, roots, branches, and step on top of the soil
Earth Engine	see Google Earth Engine

EMISAR	An airborne C- and L-band fully polarimetric SAR system operated by the Technical University of Denmark (Christensen et al., 1998)
ERS-1	European Remote-Sensing Satellite, a C-band SAR satellite
ESA	European Space Agency
fireguard	linear forest clearing created to keep wildfires from spreading (see Section 1.3)
foreshortening	the contraction of SAR imagery on slopes facing the satellite (Lillesand & Kiefer, 2000, p. 633)
GIS	geographic information systems
Google Earth Engine	a cloud computing service for global analysis of spatial data (Gorelick et al., 2017)
GPS	Geographic Positioning System
ground range	the length of the microwave beam (slant range) projected onto the Earth geoid.
HH	radar waves transmitted and received horizontally polarized (Lillesand & Kiefer, 2000, p. 639–641)
IDE	interactive development environment

InSAR	interferometric SAR
JavaScript	a high-level programming language, often used for web applications
Landsat	a program of consecutive satellites with up to 11 spectral bands and a spatial resolution of 30 metres (Barsi et al., 2014)
L-band	band of microwaves with wavelengths between 150 mm and 300 mm (Lillesand & Kiefer, 2000, p. 637)
LiDAR	light detection and ranging, a three-dimensional remote sensing technology
look angle	the angle of the radar beam with respect to the vertical line between radar antenna and Earth center (Lillesand & Kiefer, 2000, p. 623)
m	metre
mm	millimetre
MODIS	Moderate Resolution Imaging Spectroradiometer, a constellation of two NASA satellites with 36 bands of resolutions ranging from 250 metres to 1 kilometre
MulTiFuse	Multi-sensor Time-series correlation and Fusion (Reiche, Verbesselt, Hoekman, & Herold, 2015)

multispectral	imagery composed of multiple bands across the visible and infrared spectrum
n.d.	no date, added to a reference where no date is available
NASA	National Aeronautics and Space Administration
NBR	normalized burn ratio
NDVI	normalized difference vegetation index, the normalized difference of between the near infrared and red band
near real-time	within several days
omission error	proportion of undetected fireguards (complement to the detection rate)
orbit	the angle between the orbital plane and the equatorial plane
inclination	
PALSAR	Phased Array type L-band SAR, a Japanese spacebourne L-band SAR instrument
polarization	orientation of the oscillations in an electromagnetic wave
Python	a high-level programming language
radar	radio detection and ranging

RADARSAT-2	a C-band SAR satellite operated by the Canadian Space Agency
radiometric calibration	conversion of the digital number to actual backscatter (European Space Agency, 2018)
range direction	the direction of the radar beam projected onto the Earth's surface (Lillesand & Kiefer, 2000, p. 621)
RdNBR	relative differenced normalized burn ratio
RGB	red-green-blue, the channels of display imagery
SAR	synthetic aperture radar
Seninel-2	a constellation of two 13-band multispectral satellites with a spatial resolution of 10 m
Sentinel-1	a constellation of two C-band SAR satellites
slant range	the length of the microwave beam (Lillesand & Kiefer, 2000, p. 621)
speckle	grainy image appearance caused by interference of the radar waves (see Section 1.2.2)
SPOT 6	a 4-band multispectral imaging satellite with a spatial resolution of 6 metres (Satellite Imaging Corporation, n.d.-a)

SPOT 7	a 4-band multispectral imaging satellite with a spatial resolution of 6 metres (Satellite Imaging Corporation, n.d.-b)
SRTM	Shuttle Radar Topography Mission
SWIR	short wave infrared
TanDEM-X	a European X-band SAR satellite
terrain correction	conversion of image data from slant-range geometry to geographic geometry (European Space Agency, 2018)
TerraSAR-X	a European X-band SAR satellite
thermal noise	additive noise in SAR imagery caused by electron movement in the antenna (Suneela Mishra & Misra, 2016)
UBC	The University of British Columbia
UTM	Universal Transverse Mercator (a map projection)
VH	radar waves transmitted vertically and received horizontally polarized (Lillesand & Kiefer, 2000, p. 639–641)
VV	radar waves transmitted and received vertically polarized (Lillesand & Kiefer, 2000, p. 639–641)
X-band	band of microwaves with wavelengths between 75 mm and 24 mm (Lillesand & Kiefer, 2000, p. 637)

List of symbols

c	m/s	speed of light
E	V/m	electric field strength
f	1	index of the first value in the observation period
$h_{t < t_s}$	dB	value of the single-step function before the step
$h_{t \geq t_s}$	dB	value of the single-step function after the step
i	degrees	inclination, the angle between the satellite's orbital plane and the equatorial plane
i	1	running index of time series observations
M	A/m	magnetic field
n	1	number of observations in a time series
N	1	sample size
R^2	1	coefficient of determination
s	1	observation index of the first observation after the discontinuity
\overline{SR}	m	slant range (distance between SAR sensor and land cover)

t	days or seconds	time
t_s	days	time of the first observation after the discontinuity in the step function
w_i	1	weight of an observation
α	dB	trendline intercept
β	dB/day	trendline slope
σ	dB	backscatter coefficient
$\hat{\sigma}$	dB	modelled backscatter coefficient (trend or step function)
$\bar{\sigma}$	dB	mean backscatter coefficient

Acknowledgements

This research was supported by funds from Mitacs, the Consortium of Aerospace Research and Innovation in Canada and the University of British Columbia. This funding was secured by Urthecast Inc. I am grateful that these organizations enabled me to learn about my exciting thesis topic.

I was lucky to have such a smart supervisory committee. Thanks to Ken Day for keeping the connection to the research forest and making the best jokes. Thanks to William Parkinson for helping me learn the SAR fundamentals. Thanks to Lori Daniels for looking at my research from an outside perspective. Thanks to Nicholas Coops for always being available and responding fast. Many thanks for all the other support I received from my committee!

Thanks to my colleagues in the lab, whom I learned a thing or two from and who were always fun to hang out with. I am grateful that Agatha, George, Jeremy, Marco and Max did the image interpretation for this thesis. Thanks to Meaghan for her help with digitizing figures.

Many thanks go to my friends who were there for me along the way, especially: Jack, Michael and Nico from my village, the Bananarama crew that I grew close with dreaming up spaceships and aircraft at Delft University of Technology, and the folks in the UBC Varsity Outdoor Club. I could not have done it without them!

I am grateful for the support and advice I received from my big family.

Special thanks goes to my father, who took me as a child on long walks through the forest, and who showed me how the trees, the fungi, the plants, the game, the soil, the weather, and all the other parts of a forest interact to make up this incredibly complex system which provides so much value for us people. In doing so, he inspired my passion for forestry.

Dedication

To the Spirit and Opportunity rovers. May they rest in peace. To the teams who built and operated these Mars Exploration Rovers. May they live happily ever after.

Chapter 1: Background

1.1 Introduction

Sustainable forest management requires timely and accurate information to react to natural and anthropogenic forest disturbance effectively. However, near real-time monitoring of changes to forest cover and condition can be difficult due to remote access, making field based assessments logically and financially prohibitive (Sannier, McRoberts, Fichet, & Makaga, 2014). Currently, globally remote forest monitoring is primarily based on multispectral optical satellite images (Reiche et al., 2016) and aerial imagery. However, this imagery is poorly suited to near real-time monitoring (Reiche et al., 2016), as cloud cover frequently obscures optical images, leading to situations where it may take many months until a forest disturbance can be detected or characterized from optical imagery (Potapov et al., 2012).

Synthetic aperture radar (SAR) satellites acquire data by illuminating the landscape with a microwave beam pointed diagonally at the ground and recording the intensity and arrival time of the backscattered signal. This imagery has advantages over optical images for short-interval time series analysis, as image results are independent of weather and sun angle, and hence subsequent images with identical viewing geometry are consistent except for actual changes on the ground (Aronoff & Petrie, 2005). Drawbacks of SAR imagery include difficulties in rugged terrain due to the side-looking imaging geometry (hill-shadow, layover and foreshortening), the complicated microwave scattering processes, and speckle interference (Bruzzone, Marconcini, Wegmüller, & Wiesmann, 2004; Oliver & Quegan, 1998). The European

Space Agency's two Sentinel-1 satellites acquire C-band (55.5 mm wavelength) SAR imagery (European Space Agency, n.d.-a) at a 6-day repeat cycle over much of the globe (European Space Agency, 2016). This data is provided under open and free access making low-cost near real-time forest disturbance monitoring a potential reality.

Monitoring the construction of networks of roads and other linear features provides an ideal opportunity to assess the potential of disturbance detection from SAR imagery. Linear features, such as roads are easy to recognize on SAR images because of their particular geometry. Preliminary investigations for this thesis have shown that the trees on the sides of a linear feature often cause radar shadow and exhibit a corner reflector effect. These two effects feature prominently on SAR imagery. The use of SAR for near real-time linear feature detection has many real-world applications. Forest access is a pre-requisite for most forest management activities, and is typically undertaken through the building of roads. In many cases, road trajectory locations are mapped by ground-based Global Positioning System (GPS) receivers as they are built, providing a map for future reference. However, sometimes ground mapping is impractical. For instance, to combat illegal logging effectively, authorities have an interest in being alerted to new operations swiftly (Lynch, Maslin, Balzter, & Sweeting, 2013). As the construction of access roads and skid trails is the first observable change on the ground, detecting them is essential to detect logging operations in near real-time. Second, in emergencies such as wildfires, relief crews are required to construct roads (or fireguards in the case of fires) quickly without detailed or accurate mapping either prior to or after their construction. For

instance, after the 2017 wildfires in BC, the BC wildfire service (Bev Atkins, Cariboo Fire District, personal communications, September 2017) and forest managers (Ken Day, Alex Fraser Research Forest, personal communications, August 2017) struggled to map the vast network of fireguards built by fire fighters over just a few weeks to contain the wildfires that ultimately burned 1.2 million hectares (Province of British Columbia, n.d.) in British Columbia.

For this thesis, I simulated the use of SAR imagery from the Sentinel-1 satellites to monitor the firefighting efforts during the 2017 wildfires at Alex Fraser Research Forest (AFRF), British Columbia. In particular, image interpreters monitored the construction of fireguards, which were positioned to contain the wildfires. In addition to Sentinel-1, one interpreter looked at multispectral images from Sentinel-2. That way I could compare the efficacy of SAR-based monitoring with surveying based on multispectral images.

1.2 Basics of synthetic aperture radar

In this section, I review the basics of spacebourne SAR imaging, from the perspective of a data user. I describe relevant properties of microwaves, explain how the viewing geometry works, and highlight a few characteristics of the resulting imaging products relevant for this study. A technical description of how SAR sensors work is given in Lillesand & Kiefer, 2000, Chapter 8.

1.2.1 C-band microwaves

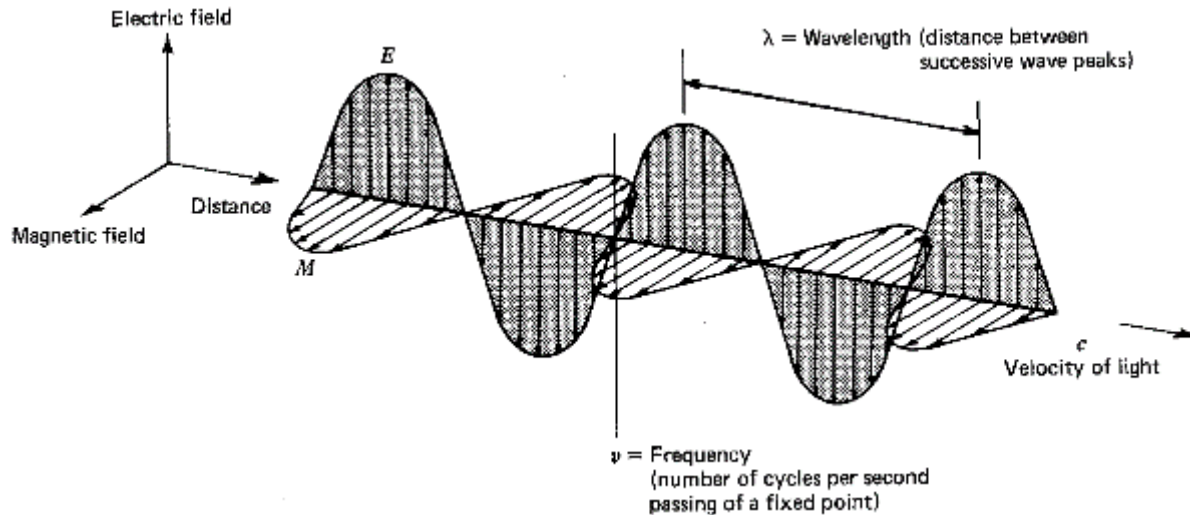


Figure 1. Structure of electromagnetic waves. Sinusoidal electric and magnetic fields travel at the speed of light. Figure source: Lillesand & Kiefer, 2000. Reprinted with permission of John Wiley & Sons, Inc.

SAR sensors work by transmitting short pulses of microwave energy to the Earth's surface and recording the microwaves reflected back (Aronoff & Petrie, 2005, p.198).

Like any other electromagnetic wave, a microwave consists of sinusoidal electric and magnetic fields travelling at the speed of light. The distance between two adjacent

wave peaks is known as the wavelength. See **Figure 1** (Lillesand & Kiefer, 2000, p. 4).

Microwaves are electromagnetic waves with a wavelength between 1 mm and 1 metre. SAR satellites typically operate in the X-band (24–37.5 mm), C-band (37.5–75 mm), or L-band (150–300 mm) (Aronoff & Petrie, 2005, p. 198). Sentinel-1 uses the 55.5 mm wavelength which lies in the C-band (European Space Agency, n.d.-a).

The reflection, transmission and absorption properties of C-band microwaves differ significantly from those of optical waves. The former penetrate clouds, haze, smoke, rain, and snowfall, allowing for all-weather operation of SAR (Lillesand & Kiefer, 2000, p. 616). The reflection properties of the land cover are related to its dielectric properties and geometric structure at the scale of the wavelength. While the colour of optical images is determined by the land cover's molecular structure, the Sentinel-1 SAR backscatter is determined by land cover structure at a scale around 55.5 mm.

Electromagnetic waves can be polarized. That means that the electric and magnetic fields of the wave have a specific orientation with respect to the direction of travel. In a vertically polarized wave, the electric field is vertical to the ground. In a horizontally polarized wave, the electric field is normal to the vertical plane. SAR sensors emit polarized microwaves and receive either the vertically or the horizontally polarized quanta of the return wave. This results in four polarization combinations a SAR sensor can utilize. For instance, images created by transmitting and receiving vertically polarized waves are known as VV (vertical-vertical) images. VV and HH (horizontal-horizontal) are called the co-polarized acquisition modes.

VH and HV are the cross-polarized acquisition modes (see **Figure 2**). (Lillesand & Kiefer, 2000, pp. 638)

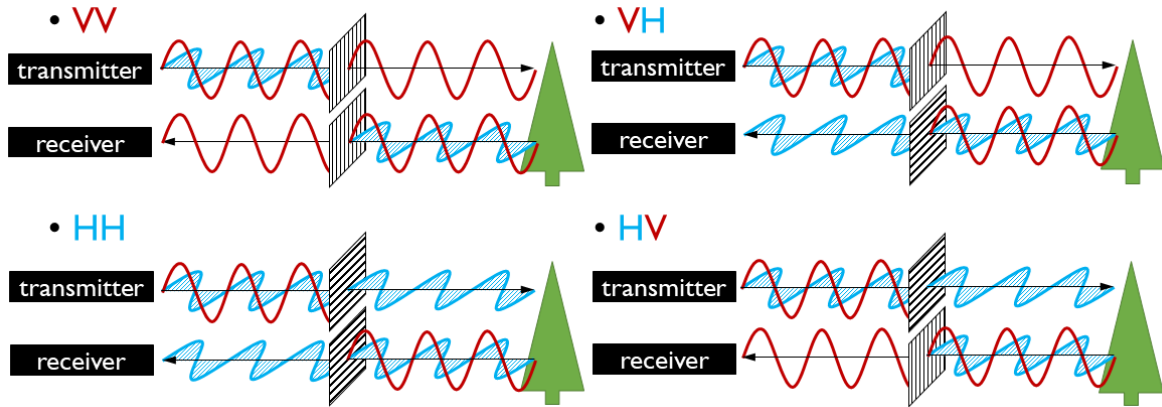
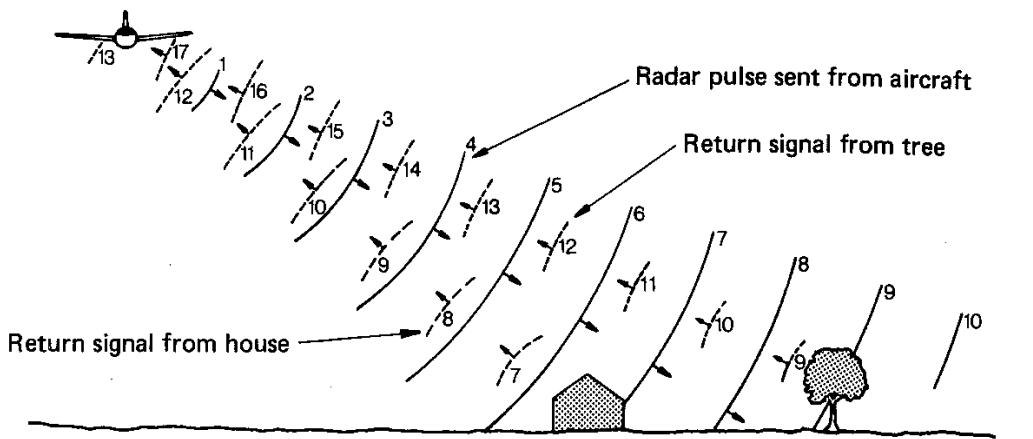


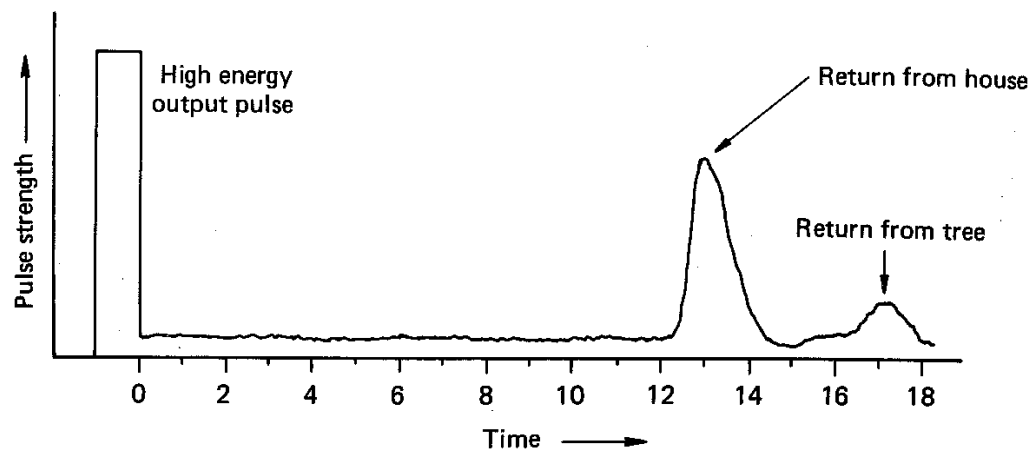
Figure 2. Electromagnetic waves can be polarized vertically or horizontally. A polarization filter (symbolized by the slanted square in the middle) can separate these. SAR sensors like the one on Sentinel-1 typically transmit polarized microwaves, and filter the received microwaves. There are four types of polarization combinations, indicated by two letters, the first of which stands for the transmission polarization, and the second for the received polarization. The waves in the Figure show the electric field.

Side-looking SAR imaging systems are mounted on the bottom of aircraft or spacecraft and pointed to the side. **Figure 3** shows how a SAR system images one strip of land. The SAR antenna transmits short pulses of microwave energy in a narrow beam at the land surface. One line of the raster image is formed by recording the time response of each reflected microwave pulse. (Lillesand & Kiefer, 2000, pp. 616)

1.2.2 SAR imaging geometry



(a) Propagation of one radar pulse (indicating the wavefront location at time intervals 1-17)



(b) Resulting antenna return

Figure 3. Operating principle of side-looking radar. An image is formed by recording the time response of a radar pulse transmitted at the Earth surface. As the tree is less reflective than the house, its return pulse is weaker. Figure source: Lillesand & Kiefer, 2000. Reprinted with permission of John Wiley & Sons, Inc.

From the time response, the slant range \overline{SR} or the distance between object and sensor is calculated as follows:

$$\overline{SR} = \frac{c \cdot t}{2}$$

Here, c is the speed of light, t is the return time, and the 2 takes into account that the microwave pulse travels the slant range twice (Lillesand & Kiefer, 2000, p. 620). As the satellite (or aircraft) moves ahead, the next pulse is used to image the next strip of land. By stitching the resulting scan lines together, one obtains the raster image in slant range–azimuth geometry. This can later be converted to geographic coordinates, using a digital elevation model (DEM) to account for the difference between slant range and ground range.

The reflectance, transmission and absorption properties of land cover types are complex. Simplified types of reflectors are shown in **Figure 4**.

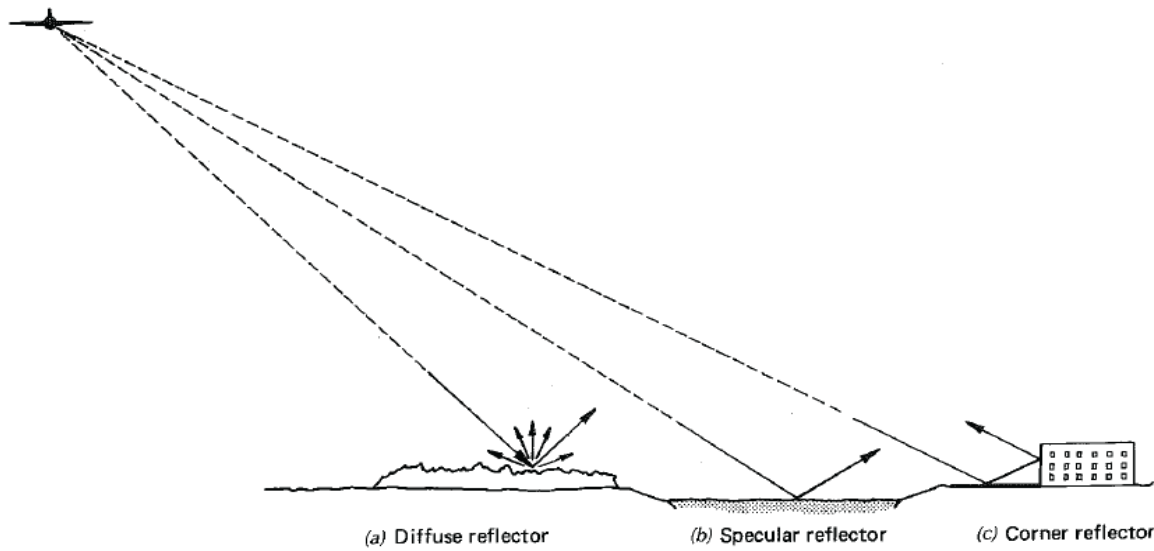


Figure 8.22 Radar reflection from various surfaces.

Figure 4. a) A diffuse reflector reflects the microwaves in all directions. The surface reflects some of them back to the sensor, leading to a faint image. b) A specular reflector reflects all energy away from the sensor, resulting in a dark image. c) A corner reflector reflects most of the radar pulse back to the sensor, creating a bright image. Figure source: Lillesand & Kiefer, 2000. Reprinted with permission of John Wiley & Sons, Inc.

Diffuse reflectors such as forests scatter the incoming microwave energy in all directions. Specular reflectors such as water surfaces reflect the energy away from the sensor. Corner reflectors in cities reflect most of the pulse back to the sensor. However, energy is not just reflected as many real land cover types also transmit or absorb microwave energy.

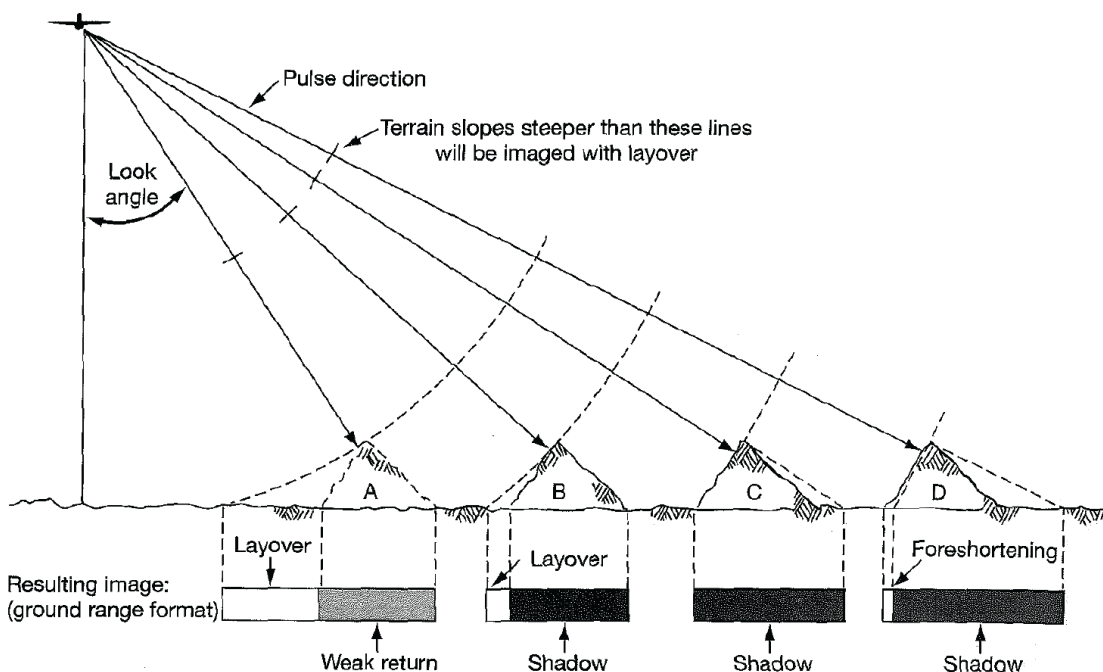


Figure 5. Terrain relief effects. *Layover:* A sensor-facing hillside is overlaid with the terrain in front of it. A weak return signal is recorded on a hillside facing away from the sensor. *Radar shadow* happens when the radar beam cannot reach a hillside facing away from the sensor. *Foreshortening* is the contraction of mellow sensor-facing hillsides. Figure source: Lillesand & Kiefer, 2000. Reprinted with permission of John Wiley & Sons, Inc.

The side-looking imaging geometry leads to terrain artefacts (a.k.a. relief displacement) such as layover, weak return, shadow, and foreshortening when the image is projected from slant range (the distance between land cover and sensor) geometry to ground range geometry (**Figure 5**). That is, the slant range is projected

onto the Earth geoid, an oval simplification of the Earth surface. This relief displacement is the reverse of what is observed in oblique photography. That is, while in oblique photos high objects are displaced away from the sensor, in SAR imaging they are displaced towards the sensor because the radar beam reflection reaches the sensor earlier than it would for flat terrain. (Lillesand & Kiefer, 2000, pp. 632)

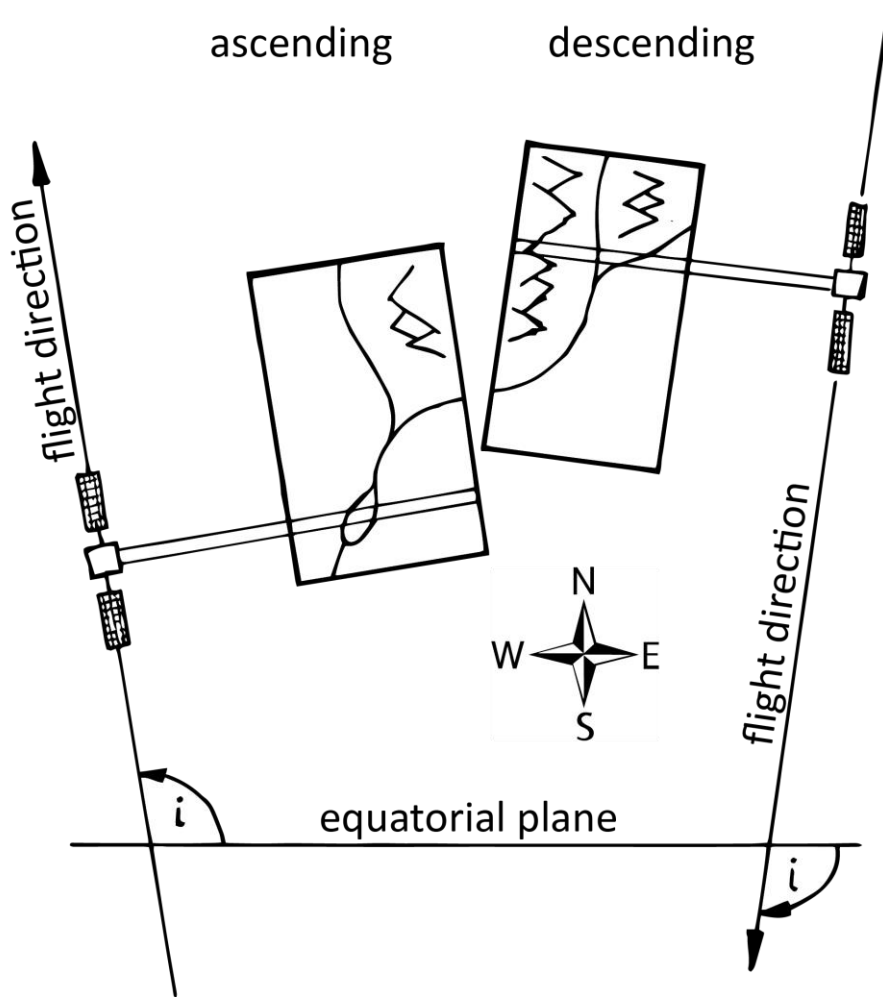


Figure 6. Ascending and descending orbits and right-looking SAR. Here, the inclination i is the angle between the satellite's orbital plane and the equatorial plane. The mountains at the top of the images show relief displacement towards the satellite.

The effects of relief displacement depend on the direction of the imaging beam and hence on the flight direction of the satellite. An orbit can be divided into two parts: the ascending node is the semi-circle when the satellite flies approximately south to north and the descending node is when the satellite flies north to south. The imaging direction of a right-looking satellite is illustrated in **Figure 6**.

Speckle interference causes SAR images to have a grainy appearance, which is produced by a seemingly random combination of constructive and destructive interference of the SAR microwaves with each other. That is, the microwaves are reflected at different phase angles, causing the electromagnetic waves to add up or attenuate each other. The result is a grainy salt-and-pepper structure of the images. This pattern can be reduced by multi-look processing or time-series averaging, but it cannot be completely removed. (Lillesand & Kiefer, 2000, pp. 641)

1.2.3 SAR images of fireguards

Fireguards can be thought of as consisting of three structural components. The forest canopy is a near-perfect diffuse reflector (Ackermann, 2015). The fireguard surface (mineral soil) is an imperfect specular reflector. The tree stems together with the fireguard surface may form a corner reflector.

In terms of imaging physics, east-west aligned linear features may appear as different backscatter patterns than north-south aligned features on SAR imagery. The Sentinel-1 satellites overfly British Columbia roughly from South to North when in an ascending orbit and from North to South when in a descending orbit. Specifically, the orbit inclination is 98.18 degrees. The imaging beam is directed

towards the satellite's right, spanning from 18.3 to 46.8 degrees from vertical. This is the range of look angles. On an ascending pass, the imaging beam looks approximately towards East, whereas in descending mode, the satellite looks towards West. As a result, fireguards are likely to appear differently depending on whether they are oriented west–east or south–north. Let us consider simplified models of fireguard geometry. East–west oriented fireguards are aligned with the radar beam and as a result, the reflected backscatter signal is solely determined by the different surface geometry and the dielectric properties of the fireguard surface compared to the surrounding forest. For a south–north aligned fireguard, the backscatter model is more complicated with the difference in reflectance properties between forest and fireguard surface playing less of a role as the forest edge on the fireguard that faces the radar beam shadows the ground surface. Additionally, a corner reflector effect may be present on the far side of the fireguard where the ground and adjacent forest form a corner. See **Figure 7**.

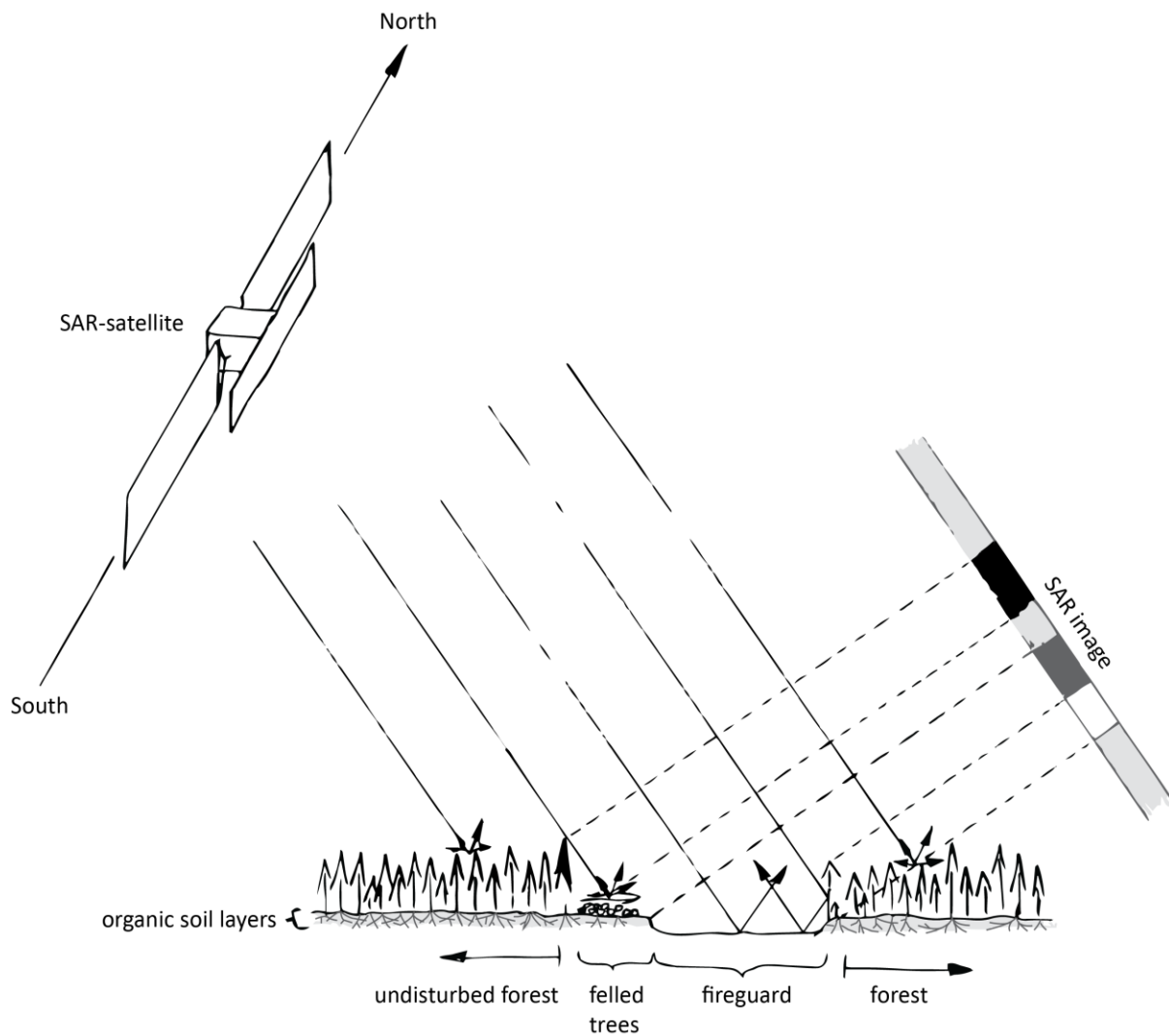


Figure 7. SAR reflectance model of a north–south aligned fireguard. The forest and felled trees appear bright in the SAR image. On the left side, radar shadow creates a black image edge. The fireguard surface appears dark. On the right side, the stems form a corner reflector with the surface and hence, appear very bright.

1.3 Wildland fire fighting

Wildland fires play an important role in BC, affecting forest ecology, public health, livelihoods, and the economy. Wildland fires burn 12 000 to 1.35 million hectares of forest every year. In 2017, the worst fire season on record up to then, the province spent C\$ 568 million and engaged about 4 700 personnel to fight fires on a total area of 1.2 million hectares. In 2018 a new record area of 1.35 hectares was burned. (Province of British Columbia, n.d.)

Three elements are required for fires to burn. These are oxygen, heat, and fuel. Together they form the fire triangle. To suppress a fire, fire fighters remove one of these elements. **Figure 8** lists three different ways of suppressing a fire: removing fuel from the path of the fire, suffocating the fire with soil, and cooling it with water (British Columbia Ministry of Forests, 2000).



Remove fuel by cutting a path or trail between the fuel supply and the fire. Ignite unburned fuel.

Remove oxygen by shoveling soil on spots.

Remove heat by applying water at the base of the flames.

Figure 8. Fires can be suppressed by removing one element of the fire triangle. Figure adapted from British Columbia Ministry of Forests, 2000.

Fireguards are used in wildland fire fighting to contain and suppress fires.

Fireguards are linear clearings in the forest that serve as fuel break, as a space to lay water hoses, and as a makeshift road to move fire fighters and equipment. During the firefighting effort, fireguards are created by removing all surface fuels and exposing mineral soil. The latter is to avoid the spread of fire through roots in the organic soil horizons, including the forest floor and duff layers. Fireguards can be constructed adjacent to a slow burning fire or away from the perimeter in the case of fast burning fires. In the latter case, firefighters often set fire on the inside of the fireguard to burn off fuel and stop the advancing fire (**Figure 9**). (British Columbia Ministry of Forests, 2000)



Figure 9. Firefighters set a backfire on the left side of this fireguard to burn fuel in advance of an approaching wildfire. Source: 570 News/B.C. Wildfire Management Branch [PNG Merlin Archive]

1.4 SAR and landscape monitoring

Currently, a few projects have tackled the problem of monitoring forest cover loss in near real-time based on SAR imagery (Appendix A). One of the most advanced is Reiche's Bayesian modelling approach. Reiche et al., 2018 used dense Sentinel-1 time series and active fire alerts to map forest cover loss in Riau, Indonesia. They used a probabilistic approach called Bayesian Updating (Reiche, Bruin, et al., 2015) to assign a forest/non-forest probability to each observation in the time series based on all the earlier observations. They achieved producer's and user's accuracies over 95% and could confirm a disturbance in natural forest within 22 days.

Airbus, the European aerospace and defence company, has also developed SAR technology to monitor deforestation. Their commercial Starling service combines optical imagery from SPOT 6, SPOT 7, Sentinel-2, and Landsat satellites with SAR imagery from the TerraSAR-X satellite to produce deforestation maps for its customers (Airbus, 2019). Starling is used in everyday operations by the food and agriculture companies, Nestlé (Nestlé Global, 2018) and Ferrero (Ferrero Corporate, 2017) who both use it to monitor their no-deforestation commitments. In addition, Ivory Coast's forestry agency uses Starling to monitor deforestation by cocoa planters and planting under the forest canopy (Earthworm, 2018).

To my knowledge, no research has been published on near real-time monitoring of the construction of linear features such as fireguards.

1.5 Planetary-scale data analysis in Google Earth Engine

The study presented in this thesis makes ample use of Google Earth Engine (hereafter shortened to ‘Earth Engine’), a geospatial cloud-computing platform. Earth Engine provides Petabytes of publicly available remote sensing data such as the Landsat archive and imagery from the European Space Agency’s Sentinel satellites, together with super-computing capacity. This enables users to analyze large amounts of remotely sensed data at global and local scales without having to invest in local hardware and data management. (Gorelick et al., 2017)

For this study, I relied on Earth Engine’s interactive development environment, where one can program the data processing steps with JavaScript, and which displays the computation results (spatial imagery and graphs) on screen. The screen image can be panned and zoomed, with Earth Engine computing the appropriate display values on the fly. (Gorelick et al., 2017)

1.6 The mission: visualizing SAR time series

The mission of my thesis is to:

*Make SAR-based near real-time disturbance monitoring accessible to forest
managers!*

To fulfil this mission, I developed an application to visualize SAR time series in a single red-green-blue (RGB) image. I developed two algorithms for computing that RGB image, a “trend composite image” and the “step composite image” (Sections 2.2.4 and 2.2.5). I aim to answer the following research questions to compare these approaches:

- 1. What spatial accuracy is achieved when delineating fireguards based on a trend composite image, step composite image or multispectral image pair?*
- 2. What factors influenced detection success?*
- 3. How quickly could new fireguards be detected based on a trend composite image or step composite image?*

Chapter 2: The science of fireline monitoring

2.1 Materials

2.1.1 Study area

The subject of this study is the firefighting response to four wildfires that burned through a part of the northern Gavin Lake block of The University of British Columbia's Alex Fraser Research Forest (AFRF) in central British Columbia (Canada) in the summer of 2017.

The west portion of the Gavin Lake block is located in the *Dry Warm Sub Boreal Spruce – Horsefly variant* (SBSdw1) biogeoclimatic zone, while the east portion lies in the *Moist Cool Interior Cedar Hemlock – Horsefly variant* (ICHmk3) zone. The major tree species are interior Douglas-fir (*Pseudotsuga menziesii var. glauca* (Beissn.) Franco, 56%), hybrid spruce (*Picea glauca* (Moench) Voss x *engelmannii* Perry ex Engelmann, 15%), western redcedar (*Thuja plicata*, 10%), lodgepole pine (*Pinus contorta var. latifolia* Douglas ex Loudon, 9%), and trembling aspen (*Populus tremuloides*, 6%) (Day & Pérez, 2013; Klinka et al., 2004).

Williams Lake features a warm humid continental climate according to the Köppen-Geiger climate classification system (Kottek, Grieser, Beck, Rudolf, & Rubel, 2006). It is characterized by cold winters, mild summers, and 577 mm of precipitation spread throughout the year, 195 mm (snow water equivalent) of which falls as snow (Environment and Climate Change Canada, 2019a). The climate normals for temperature and precipitation are shown in **Figure 11**.

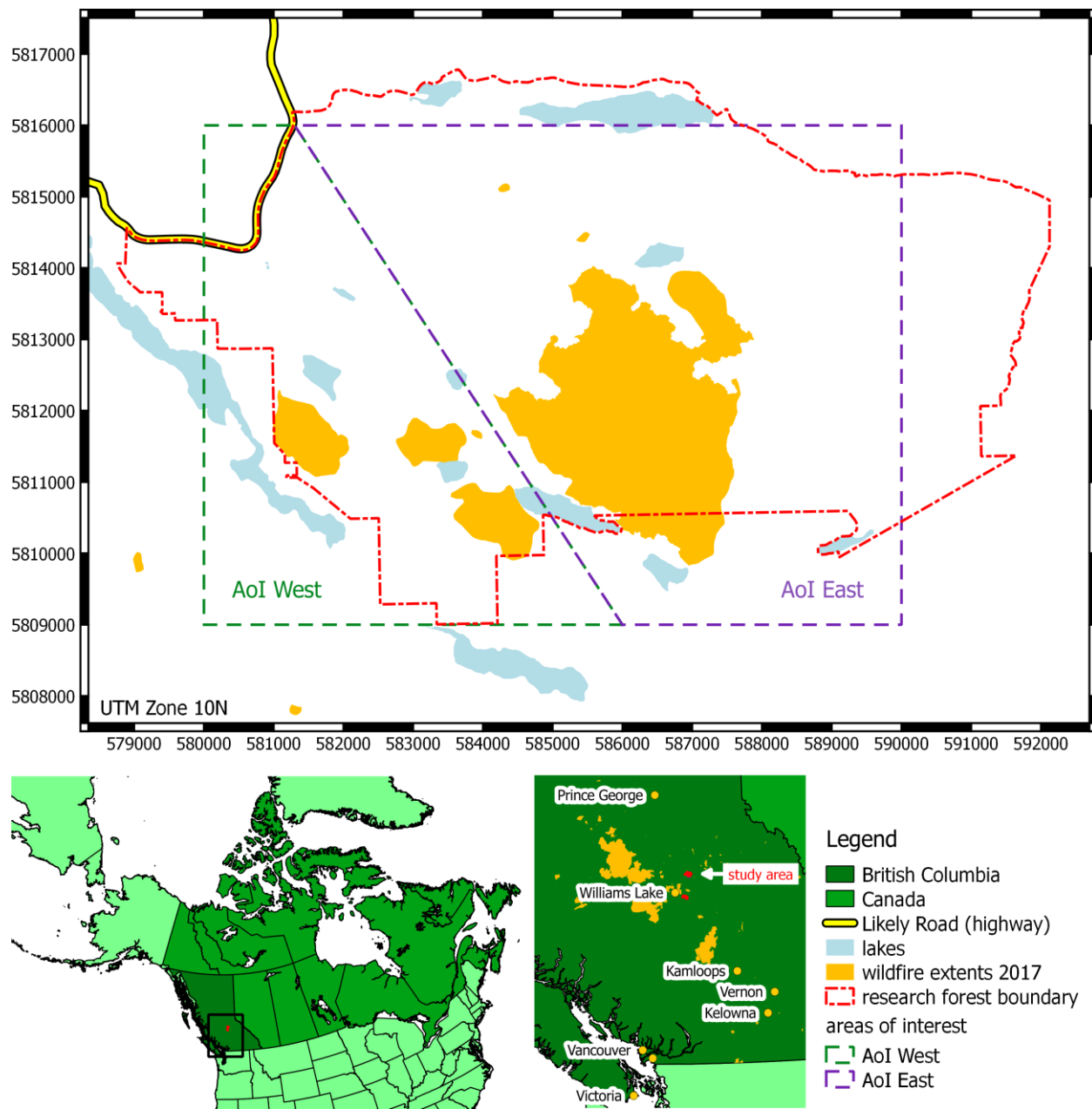


Figure 10. The subject of this study are the Prouton Lakes fires of 2017. These burned on the tenure of the University of British Columbia's research forest near Williams Lake, BC (and slightly outside that tenure). To compare feature delineation based on two types of time series composites, the study area was divided into two areas of interest (AoI), with AoI East encompassing the larger of the Prouton Lakes fires and AoI West including the extents of the other three fires.

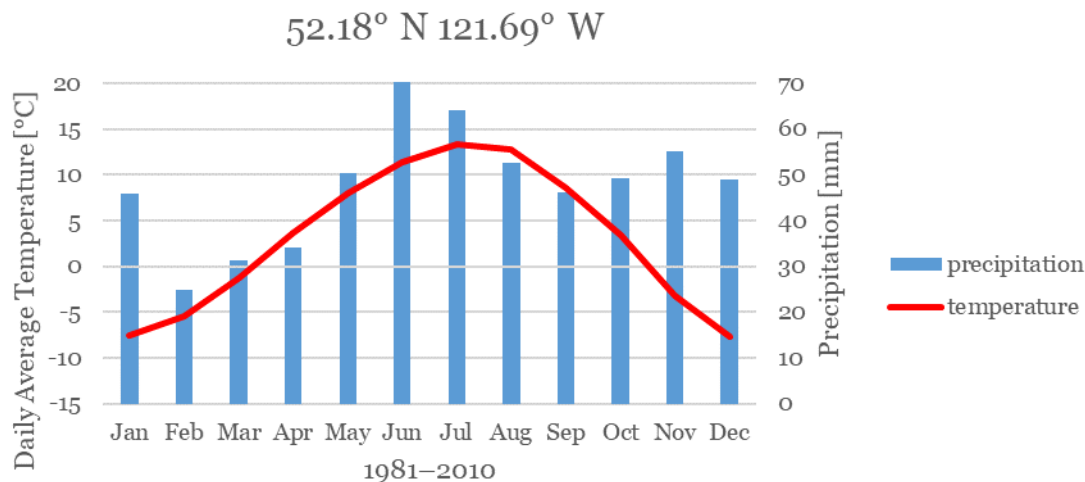


Figure 11. Climate normals for Spokin Lake weather station, about 30 km south of AFRF. Data from Environment and Climate Change Canada (2019a)

Two areas of interest (AoI) totaling 7000 hectares, which covered the approximate extent of the research forest and segregated the areas impacted by 2017 fires, were defined for this study (**Figure 10**).

The 2017 wildfire season in British Columbia broke a number of records, which were again broken the following season. 1.2 million hectares burned, necessitating firefighting efforts at a cost of C\$ 568 million, and requiring the evacuation of 65 000 people. These three figures were unprecedented (Province of British Columbia, n.d.). The fires followed an exceptionally dry period, starting with below-average precipitation in May, only 17.8 mm of rainfall in June and a mere 2.4 mm in July (See **Figure 12**) (Environment and Climate Change Canada, 2019b).

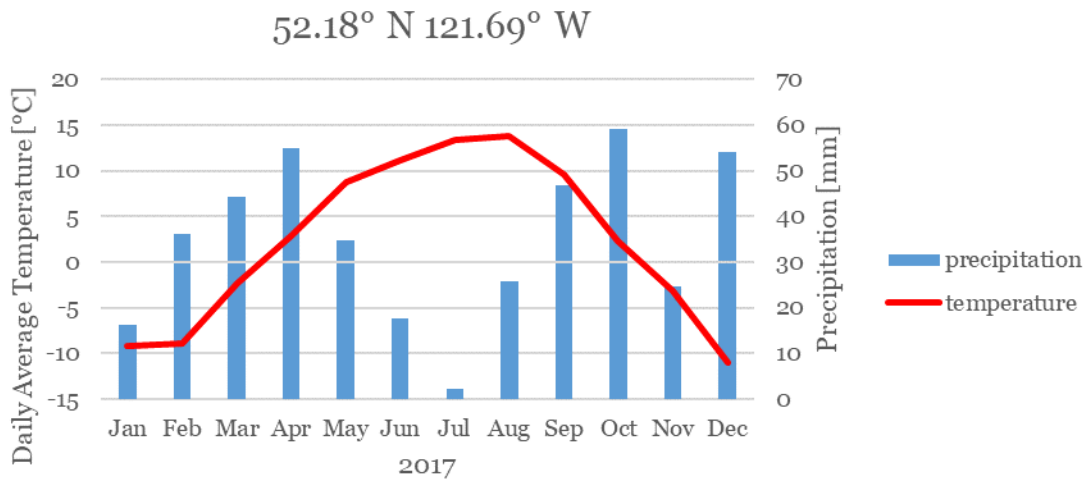


Figure 12. 2017 weather summary for Spokin Lake weather station, about 30 km south of AFRF. Data from Environment and Climate Change Canada (2019b)

Four major fires burned in Alex Fraser Research Forest (AFRF). Fire extents are shown in **Figure 10**. Lightning started these fires on July 7, 2017, and the firefighting effort commenced on the same day. On September 7, the fires were declared under control. By then they had grown to a total area of 1064 hectares (BC Wildfire Service, 2017). **Figure 13** shows snapshots of the fires' progression over the landscape. On the July 8 image, fire is readily apparent over much of the study area. On July 15 only a few fire fronts remained, and by July 30 only smoldering patches, albeit many of them remained. On August 4, the fire had flared up again or a new fire started in the eastern part of the study area. By August 17, firefighters were responding to multiple fire fronts in the northeast. On September 6, only one small fire front was visible and the next day the fires were declared under control.

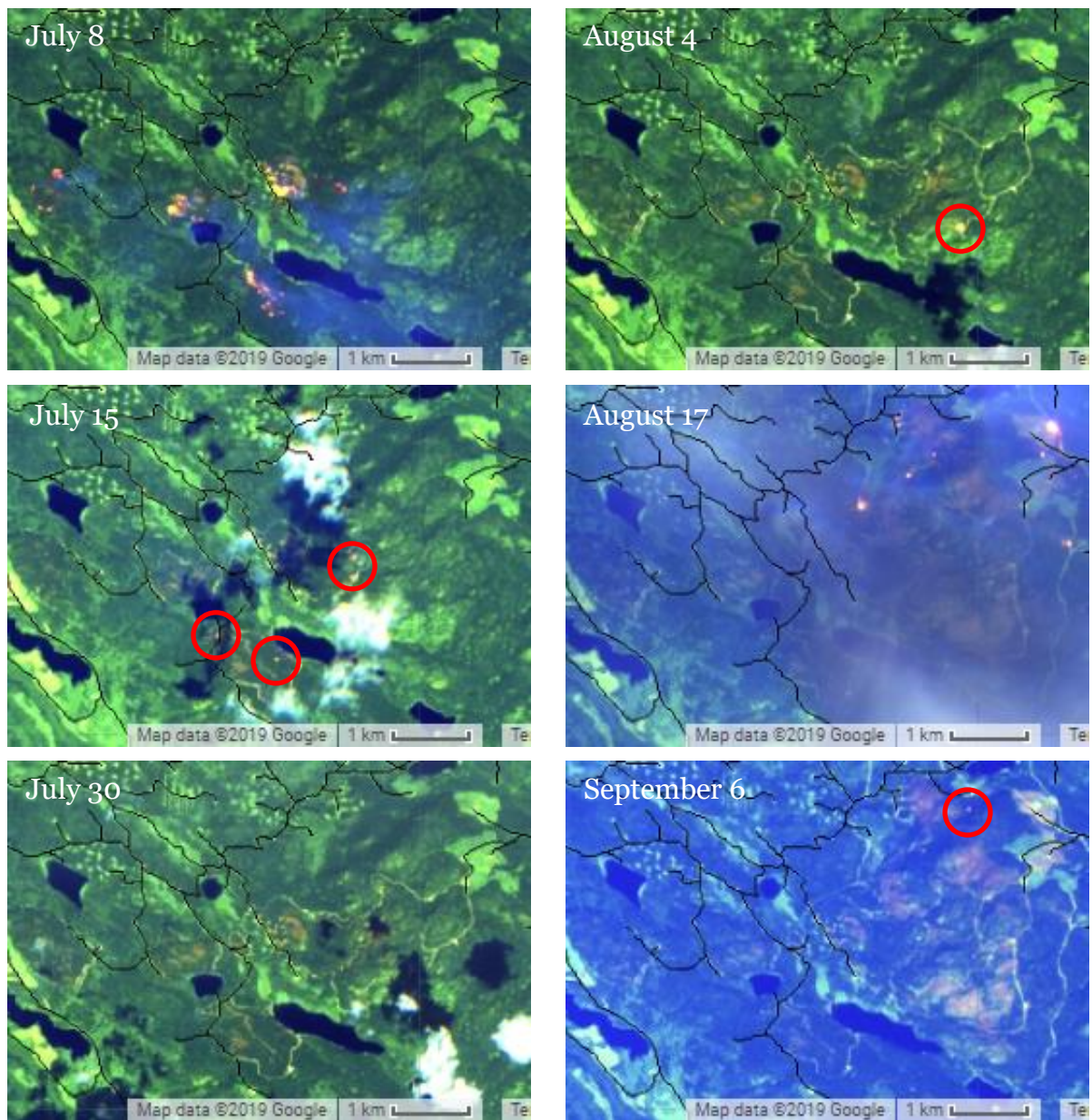


Figure 13. Progression of the Prouton Lake fires over time as seen by Sentinel-2. The images are false colour composites with bands B12 (SWIR), B11 (SWIR) and B3 (green) assigned to red, green and blue. Active fire fronts appear in yellow and orange, while smoldering regions appear in faint orange.

2.1.2 Remotely Sensed Images

In this study, I compared two manual methods to assess disturbance based on 10-m resolution multispectral imagery from Sentinel-2 and a time series of C-band SAR

imagery from Sentinel-1 (European Space Agency, n.d.-b). Furthermore, the image analysis was aided by the 30-metre digital elevation model (DEM) created by the Shuttle Radar Topography Mission (SRTM). Finally, a fire severity map based on Landsat was used for comparison.

The most common satellite data used for disturbance detection is **multispectral imagery**. Since it covers the same (and more) wavelengths as we visually perceive, it is intuitive to use. Furthermore, it has been available since 1970 and hence managers and scientists are familiar with it (Reiche et al., 2016). However, multispectral sensors' view of the landscape is often blocked by clouds or haze in the case of wildfires. For conventional disturbance detection based on optical imagery, I relied on the Sentinel-2 scenes acquired over the study area, where the ground was not entirely obscured by clouds. Specifically I used the *Sentinel-2 MSI: MultiSpectral Instrument, Level 1-C* collection in Earth Engine, where the bands represent top-of-atmosphere reflectance. In total, seven scenes were selected: five images during the burn period, one before, and one after. Sentinel-2 images have 13 spectral bands ranging from visible to short-wave-infrared. For this study only the RGB bands were used, which are collected at a spatial resolution of 10 metres. (European Space Agency, 2013)

For the **SAR**-based disturbance assessment, I created composite images from the time series of the Sentinel-1 (Torres et al., 2012) scenes available for the study area between April 25 and September 18, 2017. Some of those images covered only part of the study area. Sentinel-1 operates in the C-band of the microwave spectrum, with a center wavelength of 55.5 mm. The data are scenes with a spatial resolution of 10

metres acquired in *Interferometric Wide Swath Mode*. I relied on the Earth Engine collection named *Sentinel-1 SAR GRD: C-band Synthetic Aperture Radar Ground Range Detected, log scaling*. Most scenes had one polarization: VV. Some were dual-pol images with VV and VH but I only used the VV channel. The images included ascending and descending passes, with an orbit inclination of 98.18 degrees (**Figure 6**). (European Space Agency, n.d.-a)

The image compositing was supported by a **digital elevation model** (DEM) to optimize the viewing geometry of side-looking SAR. I used the 30-metre resolution DEM created by the Shuttle Radar Topography Mission (SRTM) in February 2000 with SAR interferometry. (Farr et al., 2007)

A **fire severity map** (Arkin, Coops, Hermosilla, Daniels, & Plowright, 2019) was used to investigate whether the output product of this study is useful for tracking fire severity. For this fire severity map, the relative differenced normalized burn ratio (RdNBR) (Soverel, Perrakis, & Coops, 2010) was calculated based on Landsat images taken before and after the fires, and divided into the four classes ‘unburned’, ‘low’, ‘moderate’, and ‘high’. RdNBR is defined by:

$$RdNBR = \frac{NBR_{\text{prefire}} - NBR_{\text{postfire}}}{\sqrt{|NBR_{\text{prefire}}/1000|}} \text{ with } NBR = \frac{B4 - B7}{B4 + B7}$$

Here, NBR is the normalized burn ratio, which is calculated from Landsat bands B4 (red) and B7 (short-wave infrared).

2.1.3 Ground Truth

As reference for the true positions of the fireguards, I used maps supplied by the AFRF staff. To create these maps, research forest staff traversed the approximate centerlines of the fireguards on foot or all-terrain-vehicle and recorded the positions with recreational GPS receivers. This method typically achieves an average accuracy of 2.3 metres (Ucar, Bettinger, Weaver, Merry, & Faw, 2014), well below the pixel size (10 m) of the remotely sensed imagery employed in this study.

In the reference Shapefile, linear features were divided in 11 categories: no description available, ‘access trail’, ‘bunched trail’, ‘existing road’, ‘existing skid trail’, ‘fire edge’, ‘fire guard’, ‘hose lay guard’, ‘safety zone’, ‘trail’, and ‘water access’. For further processing, this data was

divided into two categories: the first is ‘fire guard’ and all other labels were combined in the category ‘firefighting trails’.

Table 1. Mapping of linear feature categories in the Shapefile provided by AFRF onto the two categories used in the study.

Shapefile	study categories
N/A	
access trail	
bunched trail	
existing road	
existing skid trail	firefighting
fire edge	trails
hose lay guard	
safety zone	
trail	
water access	
fire guard	=> fireguard

2.2 Methods

2.2.1 Overview

Central to this thesis is the method of pixel-based time series compositing. This refers to the summary of a time series of images in one composite image by way of fitting a function to the time series of pixels with the same coordinates. The parameters of the function are then assigned to the RGB channels of the summary image. The aim of this procedure is to make information contained in a time series inspectable at one glance in a single composite image. **Figure 14** illustrates this process for a near-coastal area in Mozambique.

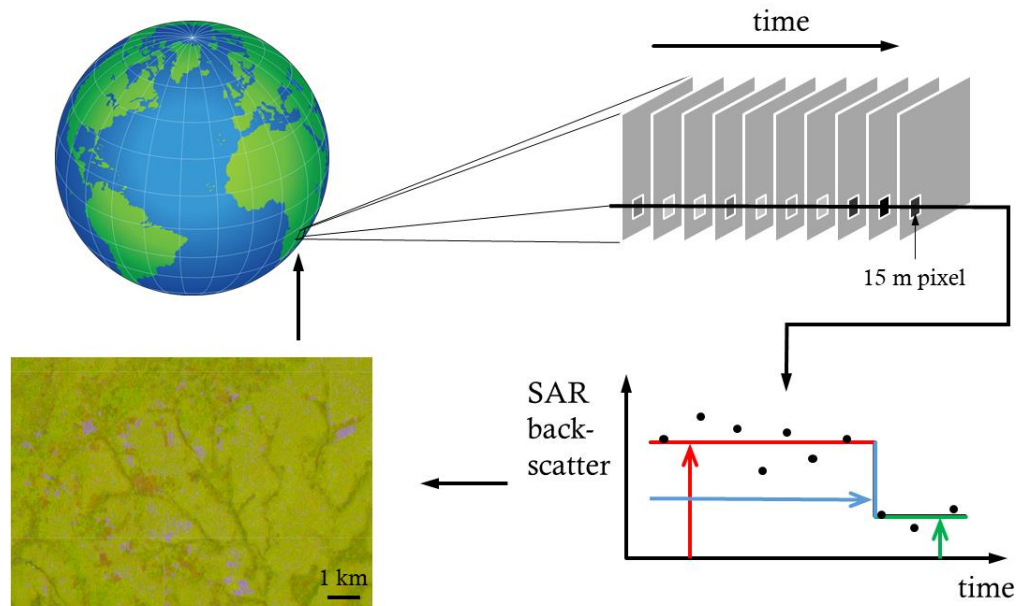


Figure 14. Pixel-based time series compositing works by fitting a function (a single-step function in this example) to the time-series of pixel values, and assigning some of the function parameters to the RGB channels of the corresponding pixel in the composite image. In this example, the value before the step was assigned to the red display band, the value after to green, and the time of change to blue. The image shows logging in coastal Mozambique.

An overview of the data flow for this thesis is given in **Figure 15**.

Pixel-based time series compositing fits functions to the underlying backscatter data and then uses those functions' parameters to fill the RGB values of a colour composite. In this thesis, I use two functions for the time series compositing: a weighted trend line and a single-step function. How these time series composites were created is described in detail in sections 2.2.4 and 2.2.5 respectively.

Prior to compositing, the SAR data required some pre-processing. Initial standard pre-processing had already been done to the data provided in Earth Engine. In addition, thermal noise on scene borders was removed and a terrain-based ascending/descending pass filter applied. See Section 2.2.2 for a full explanation of the pre-processing steps.

Next, for each observation period, the SAR images in that period were combined into a time series, which was merged into a step composite image and a trend composite image. Sections 2.2.4 and 2.2.5 explain how these time series composite images were computed. The resulting images were manually interpreted to monitor for linear features constructed in the study area. The image interpreters also had access to a multispectral image of the area for orientation. For comparison, another image interpreter was asked to detect new linear features based on a pair of multispectral images, one from before the fire, and one during/after (Section 2.2.6). How the image interpretation worked in detail is explained in Section 2.2.7. This processing and visualization was done in Earth Engine.

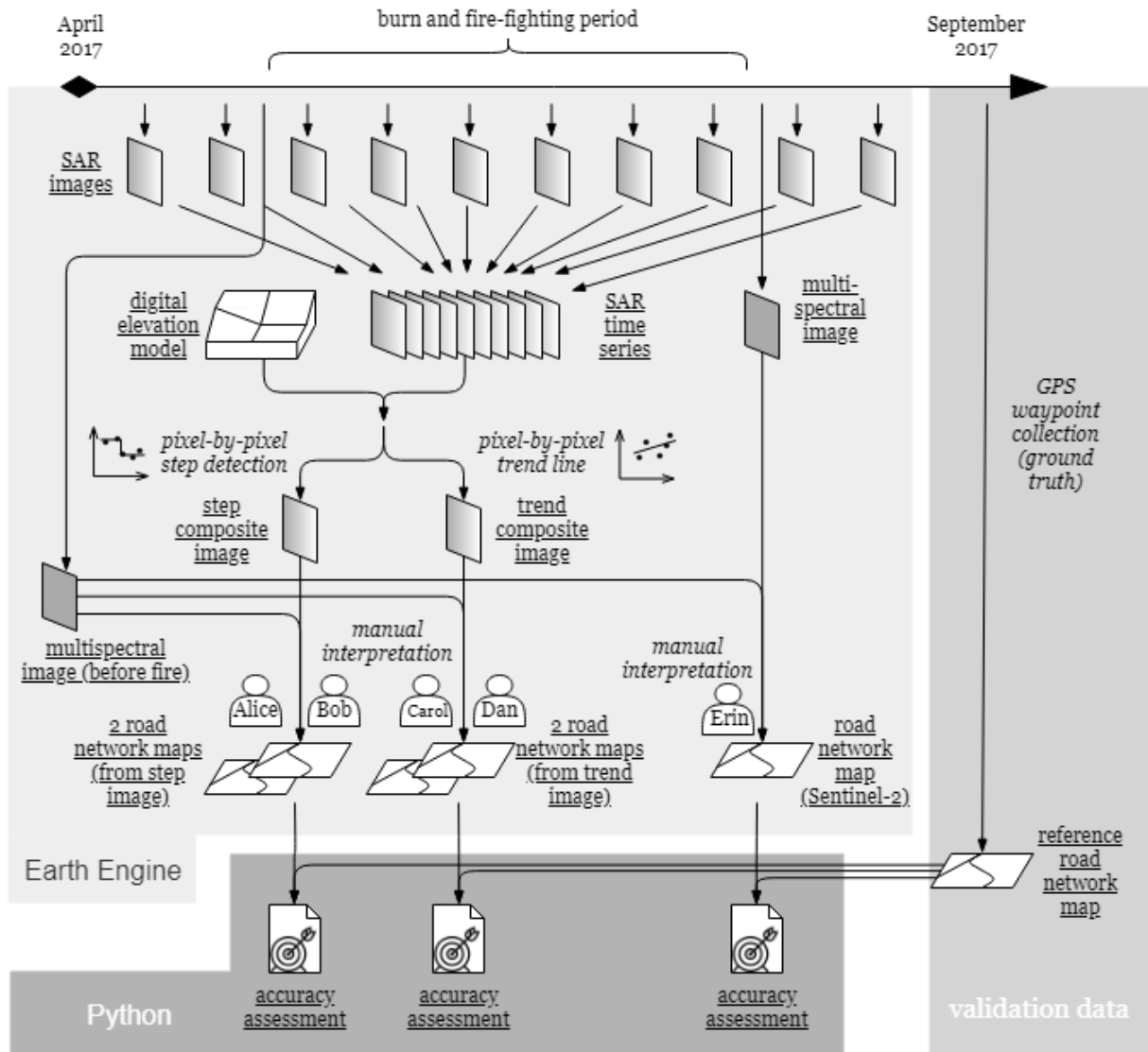


Figure 15. The flow chart shows the process for disturbance detection in AoI East at the end of the study period (September 18th). For AoI West, the image interpreters were switched as per Table 1. The same process was followed for every Monday from July 10th to September 18th using the satellite data available up to then.

A time series of Sentinel-1 data was condensed into a single composite image by two methods of pixel-based time series analysis: fitting a single-step function and fitting a trend line to the time series. Each composite was given to two image interpreters to detect new fireguards. A fifth interpreter tried to detect new fireguards based on before-after comparison of optical imagery. For validation, I relied on GPS coordinates of all fireguards collected on the ground.

As validation, a comprehensive road network map was created from GPS data collected in the eight weeks following the fire by all-terrain vehicle and on foot. I used Python to compare this reference data with the map created by the interpreters to obtain an assessment of the accuracy (Section 2.2.8).

2.2.2 Preparing the SAR time series

Sentinel-1 SAR Ground Range Detected (GRD) images were processed in Earth Engine for access to the full Sentinel-1 data archive and to facilitate large data processing (Gorelick et al., 2017). The starting point was the Sentinel-1 SAR GRD collection in Earth Engine. This collection encompasses all scenes acquired by the Sentinel-1 satellites, provided in Ground Range Detected format (i.e. without phase information). The Earth Engine team has applied the following pre-processing steps to this data (Google LLC, 2018):

- update orbit metadata
- remove noise from scene edges
- remove thermal noise
- radiometric calibration
- terrain correction based on SRTM 30 (Farr et al., 2007)

The Sentinel-1 data in Earth Engine is stored as sigma-naught backscatter ratio, log-scaled to decibels. The backscatter value in decibels is related to the backscatter ratio via (units given in square brackets):

$$\sigma_0[\text{dB}] = 10 \cdot \log_{10}(\sigma_0[1])$$

E.g., the backscatter coefficients 0.01, 0.1, and 1 are expressed as -20 dB, -10 dB and 0 dB respectively. With the data scaled to decibels, the pixel values of one scene roughly resembled a normal distribution (**Figure 16**). This is useful because common statistical methods work best with normally distributed data. In particular, a least squares fit is the same as the maximum likelihood estimate when the data is normally distributed. Therefore, I used the decibel-scaled data in all processing.

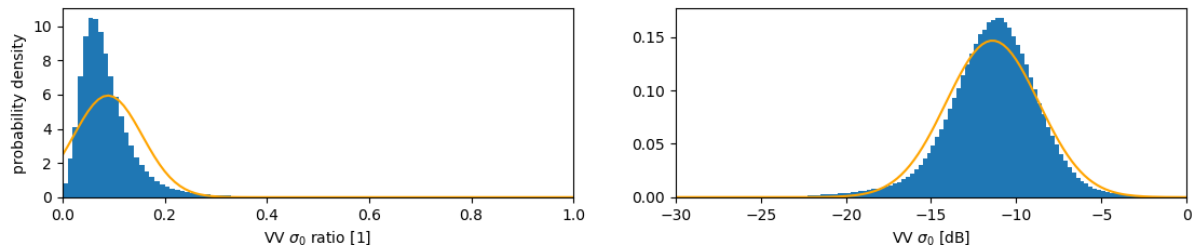


Figure 16. Histograms of one VV-image clipped to the study area (blue). The left histogram was computed from VV σ_0 values on the nominal scale, while the right histogram is based on data scaled to decibels. In the latter case, the distribution of values closely resembles a normal distribution (orange).

The SAR image analysis was limited to the VV band due to sparse availability of cross-polarized and HH data. To remove thermal noise near scene borders, I removed a 1000-metre strip from all scene borders and masked backscatter values below -21.3 dB. Finally, to account for poor SAR image quality on terrain aspects facing the satellite due to foreshortening and layover (see **Figure 5**); I masked the time-series to include only pixels from ascending-orbit images for primarily east-facing aspects and descending-orbit pixels for west aspects. This masking was based on SRTM 30. For completely flat pixels or those facing exactly north or south, only the descending-orbit images were used (**Figure 17**). **Figure 18** shows the time series composite images assembled from (a) ascending and (b) descending passes,

(c) composite images created from a time series containing a mix of ascending and descending pass images, and (d) the result of the masking method.

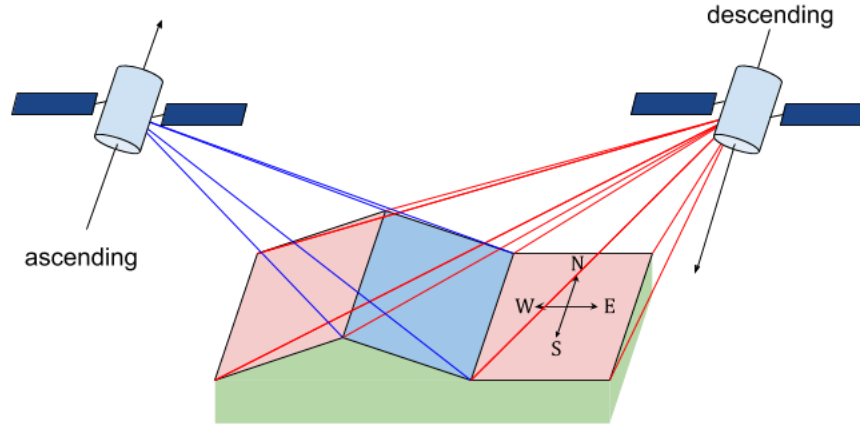


Figure 17. Each pixel in the time series composites was computed from either ascending-pass images or descending-pass images. I relied on satellite passes opposite of the terrain aspect to minimize adverse impacts of SAR-geometric effects, especially foreshortening. For the edge cases of completely level terrain and aspects facing exactly North or South, I used the descending-pass images.

Figure 18 (next page). These panels show the SAR time series composite images for different combinations of ascending and descending pass images: a) composites created from ascending pass images only; b) from descending pass images; c) ascending and descending pass images combined; d) data at each pixel computed from either ascending or descending pass data based on topography as explained in **Figure 17**. Panel e) shows the digital elevation model with 10-metre contour lines. (d) shows the method that was used for delineating the fireguards. The left half of each panel shows a step composite image, and the right half shows a trend composite (See sections 2.2.4 and 2.2.5).

Panels (a) and (b) clearly show bright, blurry regions due to foreshortening on slopes facing the satellite. This effect is abated when combining ascending and descending pass time series (c), and entirely removed when descending or ascending data is selected based on pixel aspect as explained in **Figure 17** (d). In the grainy triangular region in the center of panel (a), the 7-week time series consists of only two ascending-pass images because of missing data where adjacent Sentinel-1 scenes fail to overlap. Here the speckle interference pattern is very pronounced. In contrast, 6–9 images formed the 7-week time series used to create the region to the right.

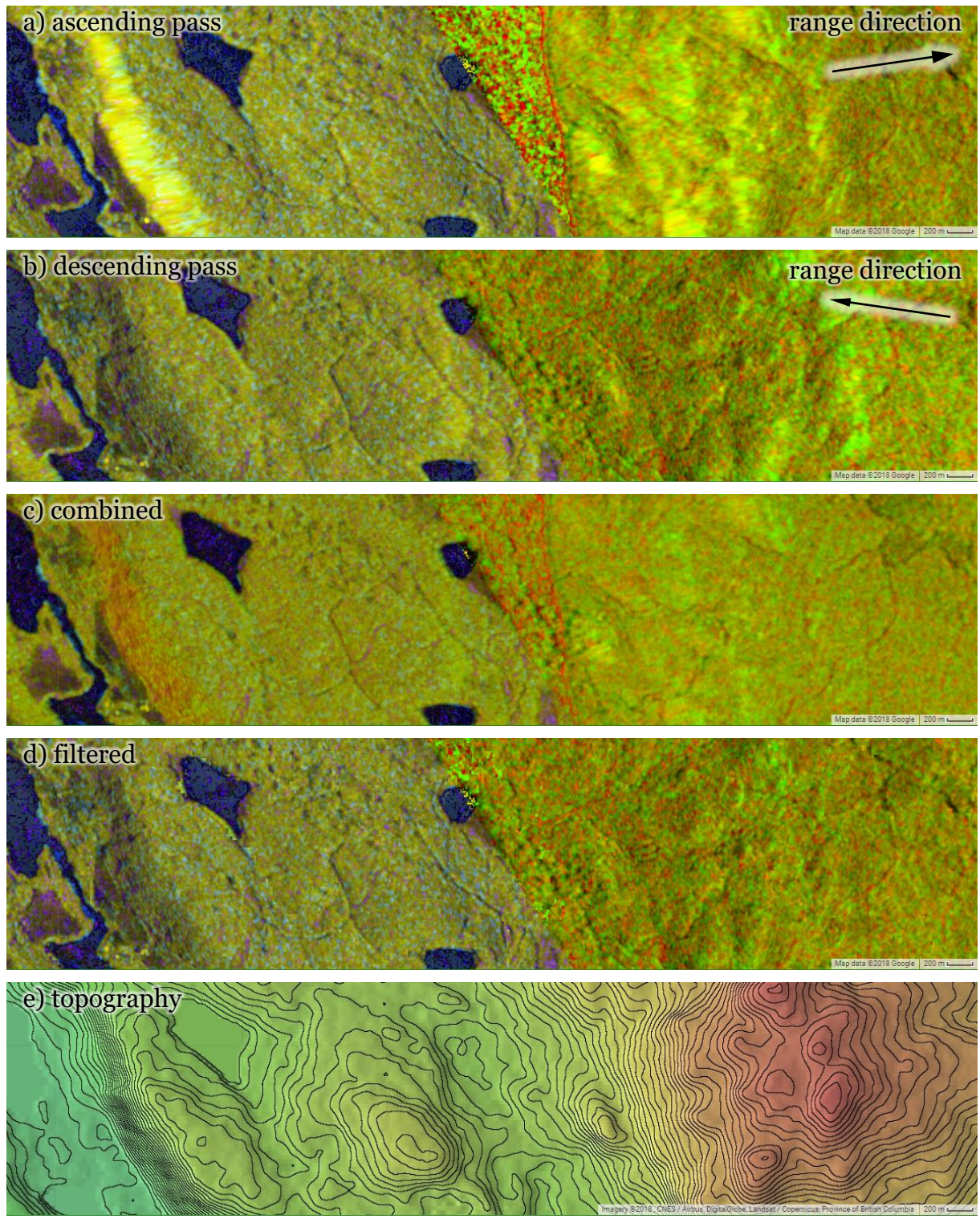


Figure 18

2.2.3 Patterns in the SAR time series

Three patterns commonly occur in time series data of landscapes: seasonal changes connected to weather patterns and plant phenology, gradual trend changes caused by growth, vegetation development and disease, and abrupt changes due to disturbance such as windthrow and logging (Verbesselt et al., 2012). Technically, many mathematical functions can be employed to model these patterns but the most straightforward are: 1) a sinusoidal with a one-year period for seasonal changes, 2) a straight line (trend line) for a gradual trend, and 3) a step function for abrupt changes. Besides these patterns, Sentinel-1 time series signals contain noise, mostly due to interference speckle.

To summarize a time series of Sentinel-1 images in a single composite image, a function that could be characterized by no more than three parameters is required, which could be represented by the RGB values of a pixel in the composite image. A sinusoidal with fixed period and a trend line are characterized by two parameters: amplitude and phase, and intercept and slope respectively. A single-step function has three parameters: its value before and after the change, and the time of change. To detect abrupt changes such as fireguard construction, fitting a single-step function is the logical method. In addition, however, I tested fitting a trend line to the last few observations of the time series, as fitting a line function is more statistically stable because it has one parameter less and is less sensitive to outliers (especially at the end of the time series).

2.2.4 Generating the trend composite image

In order to visualize changes in backscatter associated with forest disturbances, a trend line was fitted to each pixel of the backscatter time series over the 7 weeks preceding the observation date. The trend line parameters were used to summarize the time series trend in a single composite image.

To do so, I computed a least squares linear fit for each pixel with time as independent variable and decibel-scaled backscatter as dependent variable. I linearly weighted the observations based on time, giving higher weight to later observations. From the resulting trend line, I extracted the backscatter values at the start and end of the active fire period, producing a two-band composite image. I visualized these values as red and green bands respectively. Therefore, unchanged forest would appear as shades of gray, a backscatter drop associated with forest cover loss would be red, and a newly created corner reflector such as a forest edge facing the satellite would appear green. For manual interpretation, the resulting composite image was displayed with a linear stretch from -20 dB to 0 dB. The following calculations are illustrated in **Figure 19**.

That is, at each pixel straight line (on the decibel scale) is fitted with intercept α and slope β to the time series data:

$$\hat{\sigma}_{(\alpha,\beta,t_i)} = \alpha + \beta t_i$$

Note that throughout this and the following section, I use the symbol σ in place of σ_0 for the backscatter. I do this for brevity and to avoid confusion with the index i .

To compute the best fit I used least squares regression:

$$\text{minimize} \left(\sum_{i=0}^{n-1} w_i^2 (\sigma_i - \hat{\sigma}_{(\alpha, \beta, t_i)})^2 \right) \text{ with weights } w_i = \frac{t_i - t_{\text{start}}}{t_{\text{end}} - t_{\text{start}}}$$

Here, σ_i are the backscatter values for each image in the time series, and $\hat{\sigma}$ is the trend line value as a function of time. The fitting period is arbitrarily defined by t_{start} and t_{end} , 7 weeks apart; t_i refers to the acquisition time of each image within that period.

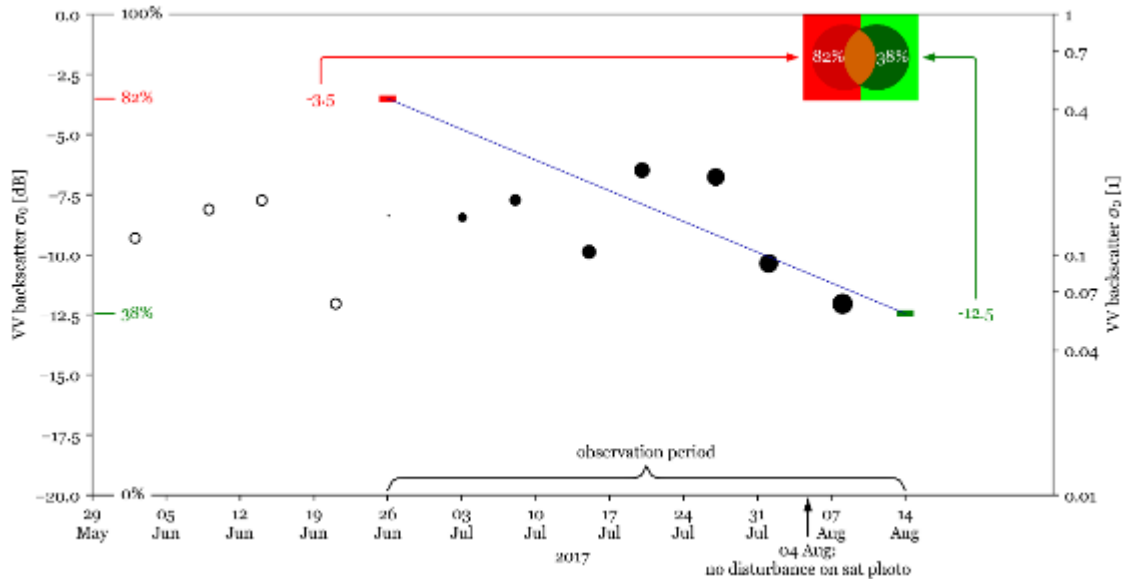


Figure 19. The pixel values for a trend composite image are calculated by fitting a straight line (shown in blue) to the weighted time series of pixel values. The time series values are indicated by the black circles. Empty circles are outside the observation period. The size of the filled circles illustrates the linear weighting. The values of the fitted line at the start and end of the observation period are assigned to red and green pixel values respectively in the trend composite image. A linear stretch is applied where -20 dB is mapped to zero brightness and 0 dB is mapped to full brightness.

After estimating the intercept α and slope β , I computed the predicted backscatter values at the start and end of the observation period (red and green bands):

$$\hat{\sigma}_{\text{start}} = \alpha + \beta t_{\text{start}}$$

$$\text{and } \hat{\sigma}_{\text{end}} = \alpha + \beta t_{\text{end}}$$

2.2.5 Generating the step composite image

As the construction of fireguards represents a sudden land cover change, a single-step function should be a more representative model of the backscatter response over time than a trend line. Therefore, I fit a single-step function to each pixel and created a composite image.

To compute the step function, I used the data during the active fire period and the scenes going back to the approximate start of the growing season (2017-04-25). I set two constraints for fitting the step function. a) The step could only occur after June 19 (the observation period) and b) two observations are required to confirm a change, ensuring a step was not detected based on the last image only. I computed the parameters of the single-step function that would minimize the squared residuals for each pixel.

In mathematical terms, this is expressed as follows:

$$\text{minimize} \left(\sum_{i=0}^{n-1} \left(\sigma_i - \hat{\sigma}_{(h_{t < t_s}, h_{t \geq t_s}, s, i)} \right)^2 \right)$$

with the single-step function: $\hat{\sigma}_{(h_{t < t_s}, h_{t \geq t_s}, s, i)} = \begin{cases} h_{t < t_s}, & i < s \\ h_{t \geq t_s}, & i \geq s \end{cases}$

and constraints: $f \leq s \leq n - 2$

This can be rewritten as:

$$\text{minimize} \left(\sum_{i=0}^{s-1} (\sigma_i - h_{t < t_s})^2 + \sum_{i=s}^{n-1} (\sigma_i - h_{t \geq t_s})^2 \right) \text{ with constraints: } f \leq s \leq n - 2$$

Here $\hat{\sigma}_{(h_{t < t_s}, h_{t \geq t_s}, s)}$ is the definition of a step function with one discontinuity before the s^{th} value in the time series and backscatter values $h_{t < t_s}$ and $h_{t \geq t_s}$ before and after the discontinuity respectively. Then, $\sigma_0 \dots \sigma_{n-1}$ are the backscatter values throughout the time series, n is the number of values in the time series, and f is the index of the first value within the observation period. Again, I every σ is short for σ_0 . These equations are illustrated in **Figure 20**.

The above equation is an optimization problem in three variables: s , $h_{t < t_s}$ and $h_{t \geq t_s}$. However, we know that the least squares fit of a simple difference is the average:

$$\text{minimize} \left(\sum_{j=1}^m (\sigma_j - h)^2 \right) = \sum_{j=1}^m (\sigma_j - \bar{\sigma})^2$$

$$\text{with the average given by } \bar{\sigma} = \frac{1}{m} \sum_{j=1}^m \sigma_j$$

Then the optimization problem becomes a problem in only one variable, s :

$$\text{minimize} \left(\sum_{i=0}^{s-1} (\sigma_i - \bar{\sigma}_{t < t_s(s)})^2 + \sum_{i=s}^{n-1} (\sigma_i - \bar{\sigma}_{t \geq t_s(s)})^2 \right) \text{ with constraints: } f \leq s \leq n-2$$

$$\text{and averages: } \bar{\sigma}_{t < t_s(s)} = h_{t < t_s} = \frac{1}{s} \sum_{i=0}^{s-1} \sigma_i \text{ and } \bar{\sigma}_{t \geq t_s(s)} = h_{t \geq t_s} = \frac{1}{n-s} \sum_{i=s}^{n-1} \sigma_i$$

Analogous to the trend image, the backscatter values of the resulting step function (the best fit) were then used as the red ($h_{t < t_s}$) and green ($h_{t \geq t_s}$) bands of the change composite image for manual interpretation.

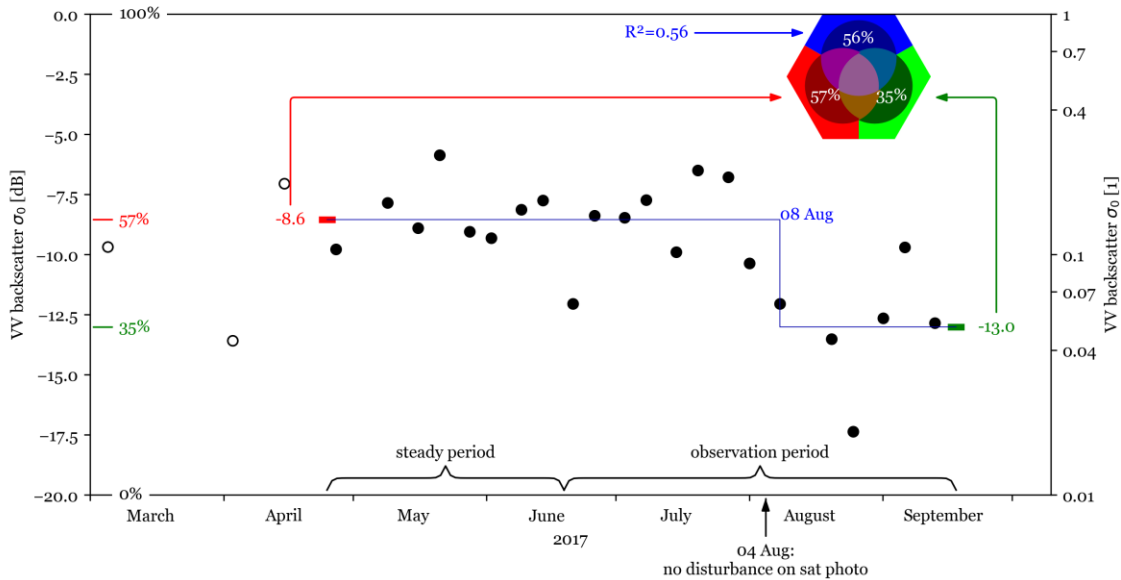


Figure 20. The pixel values for a step composite image are calculated by fitting a single-step function (shown in blue) to the time series of pixel values (black circles). The step function is constrained such that a step can only occur in the observation period and at the latest at the next-to-last data point. The RGB values of the resulting pixel in the step composite image are derived as follows. Red represents the left tail value and green the right tail value. These stretch from -20 dB (zero brightness) to 0 dB (full brightness). Blue represents the coefficient of determination R^2 of the fit.

In addition, a blue band was added that showed the R^2 value (coefficient of determination) of the step function's fit. R^2 is a measure for how much of the variance in the data is explained by the model function and is computed as follows.

$$R^2 = 1 - \frac{\sum_{i=0}^{n-1} (\sigma_i - \hat{\sigma}_i)^2}{\sum_{i=0}^{n-1} (\sigma_i - \bar{\sigma})^2}$$

with step function value $\hat{\sigma}_i = \hat{\sigma}_{(h_{t < t_s}, h_{t \geq t_s}, s, i)}$ and mean $\bar{\sigma} = \frac{1}{n} \sum_{i=0}^{n-1} \sigma_i$

2.2.6 Sentinel-2 images

For the area and period that were investigated in this study, only seven usable Sentinel-2 scenes were available, two of which were covered in almost opaque haze. To serve as a comparison to the SAR time series methods described above, I asked an interpreter familiar with the study area to conduct a conventional before-after comparison based on all available Sentinel-2 imagery.

2.2.7 Manual image interpretation

During and after the 2017 wildfires, staff at AFRF used an early version of these algorithms (unweighted linear fit) to delineate 55 km of fireguards created during the firefighting effort. While they found the method accurate and useful, not enough data was collected to allow for a rigorous analysis, especially of detection times (personal communications, Ken Day & Parabhjot Sandhu, AFRF, August–October 2017). Therefore, I simulated what an interpreter might detect if they would spend

time every Monday during wildfire season delineating disturbances based on the newest imagery.

I asked image interpreters with varying levels of experience to delineate the development of fireguards with the methods I had developed. The interpreters were asked to take a colour-blindness test based on Ishihara plates (EnChroma Inc., 2018), which showed that all five of them had normal colour vision. In this thesis their names were changed to ensure anonymity.

Interpreter	Has interpreted optical satellite images?	Has fought wildland fires?	AoI West	AoI East
Alice	yes	no	Sentinel-1 <i>trend</i> composite image	Sentinel-1 <i>step</i> composite image
Bob	yes	no	Sentinel-1 <i>trend</i> composite image	Sentinel-1 <i>step</i> composite image
Carol	yes	no	Sentinel-1 <i>step</i> composite image	Sentinel-1 <i>trend</i> composite image
Dan	yes	yes	Sentinel-1 <i>step</i> composite image	Sentinel-1 <i>trend</i> composite image
Erin	yes	yes	Sentinel-2 image pairs	Sentinel-2 image pairs

Table 2. Interpreter experience and spatial division of interpretation tasks. The first four interpreters delineated one AoI based on a trend composite image and the other AoI based on a step composite. This way I could directly compare the two methods and correct for variance in interpreter skill. Interpreter 5 delineated the fireguards by comparing two multispectral images, which is representative of conventional image interpretation.

The delineation was simulated for every Monday from July 10 (two days after the first wildfires were discovered) to September 18 (eleven days after the fire was declared ‘no longer a wildfire of note’). The two AoIs (**Figure 10**), allowed for controlling for interpreter skill differences when analyzing the results. **Table 1** shows the division of interpretation tasks and two pertinent skills.

The three different approaches I employ (and compare) to delineate fire guards rely on differing amounts of image data as shown in **Figure 21**. For the before-after comparison of multispectral images, Erin was given the six Sentinel-2 images available around the active fire period (four inside and one at either end). She compared each of the five images sensed during the burn period and the one image sensed afterwards with the image sensed before the burn period. She recorded all linear disturbances that were present in the last six images but not in the first one. For constructing the trend images every Monday, I used the Sentinel-1 images from the 7 weeks prior to that Monday. For constructing the step images, I relied on Sentinel-1 imagery from the start of the growing season up to the respective day of delineation. For fitting the step function, I constrained the function such that a drop is only expected after June 19.

Figure 21 (next page). Overview of imagery employed for fireguard delineation. Fireguards were delineated based on the imagery available every Monday (delineation day) from July 20 to September 18, 2017. I derived the trend composites from the Sentinel-1 images spanning the seven weeks before delineation day. The step composites were constructed based on all Sentinel-1 images since April 24. The period until June 19, 2017 was taken as steady. I used the five Sentinel-2 images available over the active fire period and the one image after directly and compared them to the image from June 25. *Due to a typo in the instructions, Bob and Carol set the date given by July 17 to July 14 when doing the delineation.

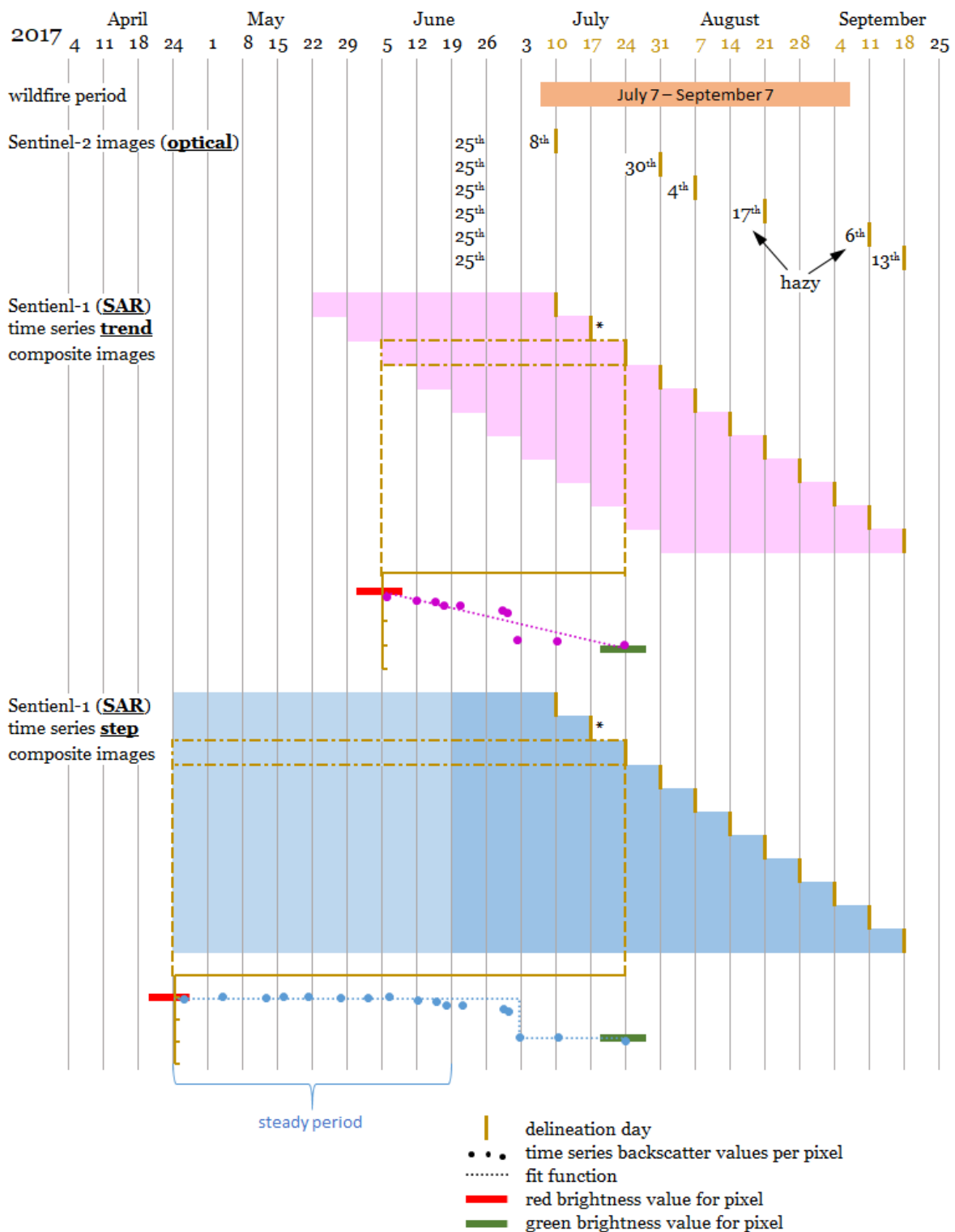


Figure 21

The interpreters viewed the composite images in Earth Engine and delineated the fireguards with the ‘draw a line’ tool. The full instruction that the interpreters received are given in Appendix B.

I did not control for interpreter differences when interpreting the Sentinel-2 images because it is 10-metre spatial resolution optical imagery and is relatively straightforward to interpret. Furthermore, the objective was to show the best result an interpreter could achieve with Sentinel-2 imagery. Therefore, and due to operational constraints, I relied on an interpreter that was familiar with both the study area and wildland firefighting.

2.2.8 Accuracy Assessment

To conduct the accuracy assessment and visualize the results, I produced Python scripts to analyze the delineation maps that the interpreters drew in Earth Engine. For numerical data processing I relied on the libraries Numpy (Oliphant, 2006) and Pandas (McKinney, 2010), for GIS processing I used Geopandas (van den Bossche & et al., 2017), Shapely (Gillies & et al., n.d.) and rasterio (Gillies & et al., 2013), and for plotting Matplotlib (Hunter, 2007) and Colormaputil (Denis, 2013).

To quantify the accuracy of the fireguard network maps produced by the image interpreters, I calculated the proportion of false positives among delineated lines (commission error), the proportion of undetected fireguards (omission error), and the average spatial deviation of correctly delineated lines from the reference fireguard locations. To check if the omission error is affected by fireguard orientation or terrain steepness, I quantized the fireguards reference into 10-metre segments,

and produced histograms binned by segment orientation or local terrain steepness.

The following paragraphs lay out the precise methods for doing these calculations.

First, an inconsistency with the way the interpreters read their instructions had to be rectified. Bob and Carol had marked all changes in each image they saw, while Alice, Dan, and Erin only marked new changes that were not present in the previous image. I had expected the interpreters to do the latter. Therefore, all instances of multi-delineations of the same features were automatically removed. This removal worked by erasing all features within a 50-metre buffer of the features already present at a set date. Unfortunately, this approach also removed some fireguards that were close to each other on the ground from the dataset.

For computing the commission error, two conditions were used to determine whether a line on the delineation map corresponds to a new feature on the ground or is a false positive. To be counted as correct, the line segment on the map a) must be within 50 metres of a line in the reference fireguard map and b) must be roughly aligned with that line. I implemented these conditions as follows. (a) I computed the intersection of the delineation map with a 50-metre radius buffer (with circular caps) around the reference map, which yielded all line segments within 50 metres of the reference. (b) Then I removed all remaining segments that touched a boundary of the buffer and were less than 200 metres long (twice the buffer width). **Figure 22** illustrates an example of how this algorithm distinguished between correctly delineated fireguards and delineated image artifacts that corresponded to no change on the ground.

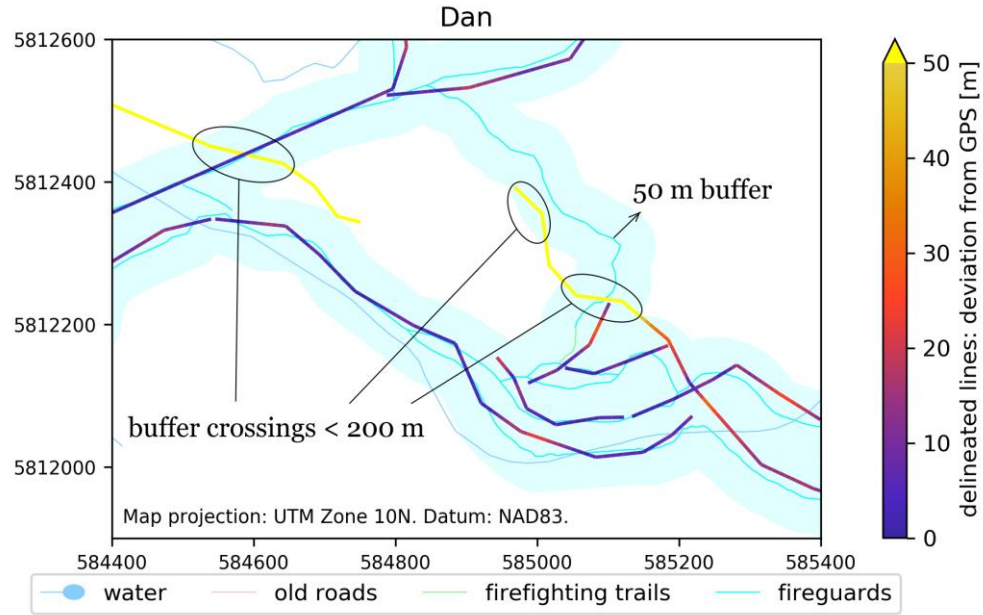


Figure 22. Example detail of how the algorithm decided which lines on the interpreters' maps corresponded to real new features on the ground and which were interpretation artefacts. Blue to orange: correct lines. Yellow: artefacts. In this example, the lines that the interpreter wrongly picked up were caused by wrong pixel values on the SAR image boundaries. Besides line segments more than 50 metres away from the reference, we considered segments as incorrect that crossed the buffer and where less than 200 metres long.

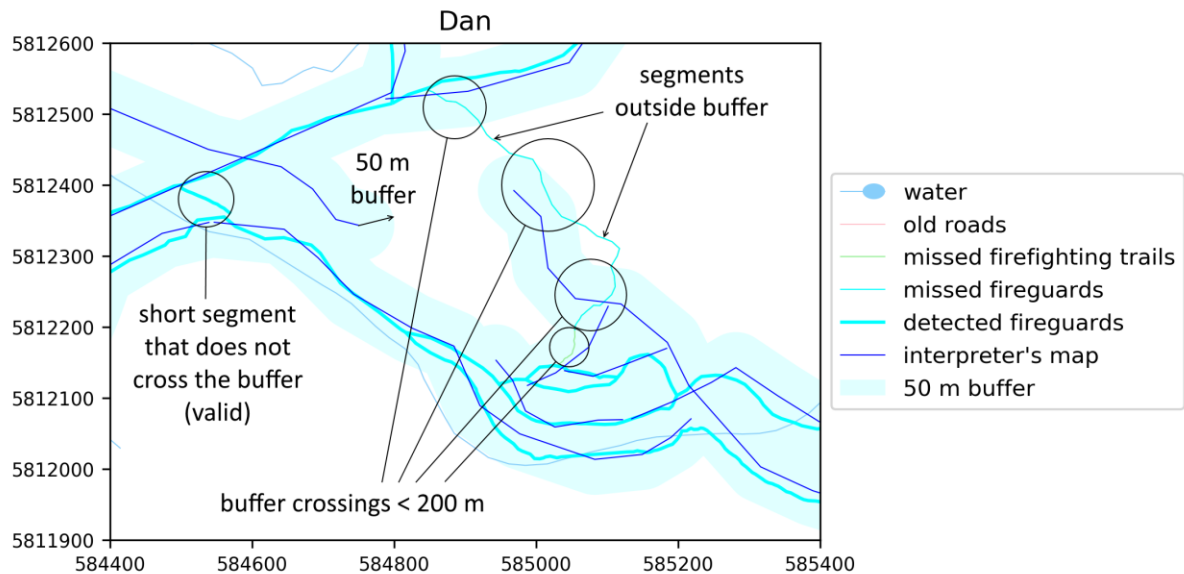


Figure 23. Example detail of how the algorithm decided what fireguard segments were delineated and what segments were missed.

To compute the omission error, I reversed the procedure described in the previous paragraph, with the buffer constructed around the lines on the interpreter's map, and applying conditions (a) and (b) to the fireguard lines. This is illustrated in

Figure 23.

I quantized the interpreters' maps into segments no longer than 10 m, which allowed me to calculate the average deviation of delineated lines from the reference fireguard locations and to compute histograms of delineation success binned by fireguard orientation and terrain steepness. Specifically, every straight segment in a line drawn by the interpreter was divided into as few segments as possible, each no longer than 10 metres. The value of 10 metres was chosen for quantization as it represents a good trade-off between computation time and precision of the results. Specifically, lowering this value to 5 metres did not lead to different results in average deviation at the precision at which I report them.

I computed the deviation vector for each ≤ 10 -metre segment by taking the vector difference between the midpoint of the segment and the closest point in the reference map (**Figure 24**). From these deviation vectors, I calculated the average deviation of delineated lines from the reference.

I examined if a directional bias existed in the way linear features were delineated which could arise through imperfect ortho-rectification in the imagery, a bias in the GPS coordinates of the reference data, accuracy errors in converting between projections, and biases created due to the side-looking geometry of SAR. To check for biases, I computed the deviation vector for each 10-m-segment of the fireguards.

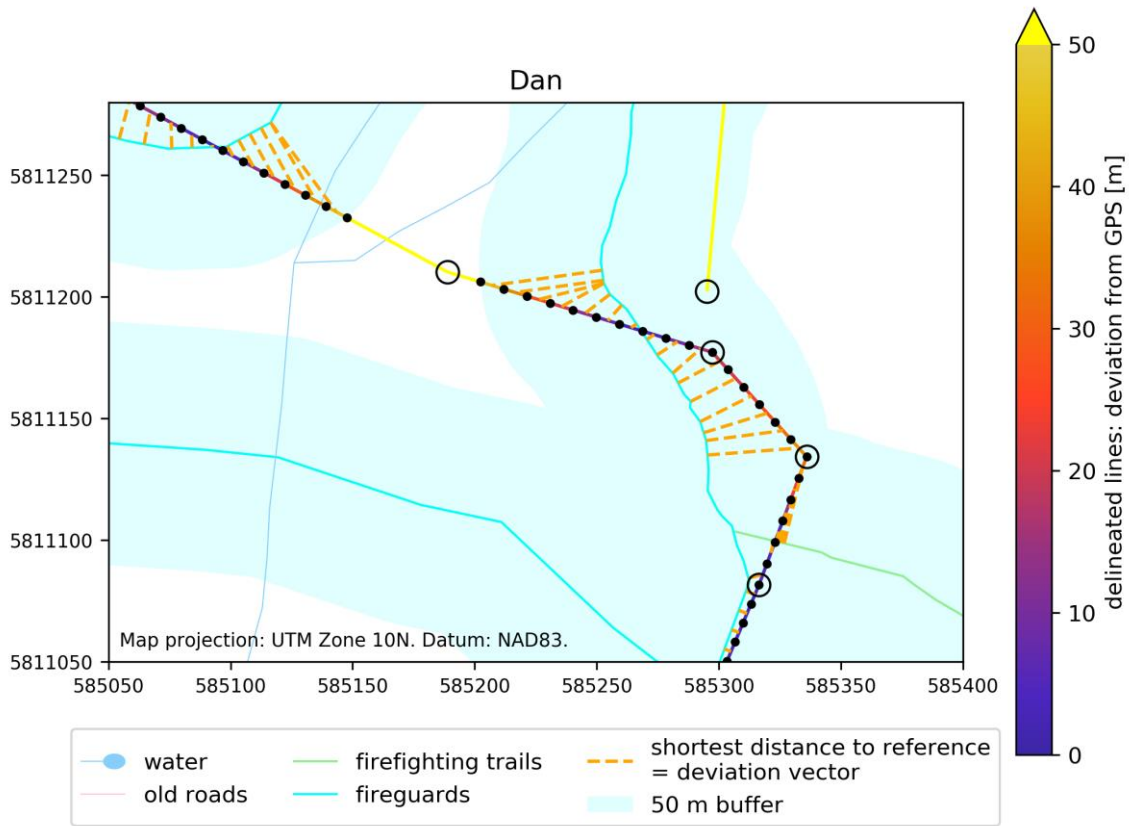


Figure 24. Example detail showing how the ‘correct’ lines were split into $\leq 10\text{ m}$ segments and how the distance to the reference fireguard map was calculated. The circles indicate the positions where the interpreter clicked on the map, as well as the intersections with the 50-metre buffer shown in light blue. Each edge inside the buffer was divided into as few segments of no more than 10m metres length as possible, separated by a dot on the map. The distance to the reference was calculated by measuring the shortest distance (indicated by dashed orange lines) from segment midpoint to any of the reference lines (the fireguards and firefighting trails).

Due to the side-looking imaging geometry, SAR imagery is more difficult to process and interpret in rugged and/or steep terrain (Lillesand & Kiefer, 2000, pp. 632). To investigate the influence of terrain steepness on the detection rate in the simulation, I stratified the fireguards by slope steepness for each of the half-maps produced by the image interpreters. The slope steepness strata are 3-degree wide bins up to 15 degrees and one stratum for all fireguard segments steeper than that.

2.3 Results

First, I demonstrate some example time series composite images and the maps produced based on them, at different levels of zoom (Section 2.3.1). Then I investigate some interesting features on those example maps that correlate with high fire severity (2.3.2). Next, I quantify the detection success for the different image types and interpreters (2.3.3) and examine what spatial accuracy was achieved with different image types, stratified by orbital pass direction (ascending or descending) (2.3.4). Furthermore, I investigate how terrain features such as slope angle, streams or clearcuts influenced detection rates (2.3.5). Then I conduct an anecdotal investigation of the time lags between fireguard construction and detection (2.3.6). Finally, I report how long it took the interpreters to delineate the images they were given (o).

2.3.1 Example maps

Eleven trend composite images and eleven step composite images were computed for the study area and different dates within the observation period (See **Figure 21**). An example of these composite images is shown in **Figure 25a**. Thin linear features such as fireguards cannot be discerned at this resolution but other landscape features as well as algorithm artefacts are visible.

The trend composite image on the left side (AoI West) is composed of red and green channels, with red representing the trend value at the beginning of the observation period and green representing the value at the end (Section 2.2.4). Some areas of the image appear grainy. Recall that parts of the image are composited from ascending

pass images and others from descending pass images (Section 2.2.2). In this case, the time series from July 31 to September 18 consisted only of a few ascending pass images, leading to noisy results when computing the trend line. Apart from that, the image shows several dark areas. Moderately dark areas include small blocks harvested in the winter 2015/2016 near the top left of the image, small blocks harvested at other times, and a steep slope at left center. This steep slope faces away from the descending satellite, which passes east of the imaged area. Very dark patches correspond to lakes.

The step composite image on the right side (AoI East) is composed of red, green and blue channels, which represent respectively the left tail, the right tail, and the R^2 value of a single-step function fit to the time series (Section 2.2.5). Hence, anything blueish indicates a potential land cover change. However, care in interpretation is needed because the red and green values scale with the brightness of the radar backscatter while R^2 does not. Therefore, areas that are dark in the SAR image appear more blueish simply because red and green are less bright. A clear backscatter decrease should appear purple because the left tail value (red) is higher than the right tail value and the R^2 value (blue) is high. Conversely, a backscatter increase appears cyan because the right tail value (green) is higher and R^2 (blue) is high.

There are a number of interesting features in AoI East:

- A. The purple region with a cyan dot in the top-right is the Mount Polley mine.
- B. Pixelated regions with lots of blue close to the right image boundary represent step composites computed from ascending pass time series, which only consisted of very few images.
- C. Darker regions with a little purple are older clearcuts.
- D. Bright regions with a little purple close to the center of the step composite were affected by fire. These are explored further in the next section.
- E. The lakes appear blue in the step composite image because even low values of R^2 stick out against very low backscatter values.
- F. Small cut blocks appear as dark spots, for instance in the top left.

Figure 25a also shows the linear features delineated by the image interpreters in various colours according to date, as well as the pre-existing road network as black lines. The delineated lines are again shown in **Figure 25b**, this time coloured according to their deviation from the GPS reference.

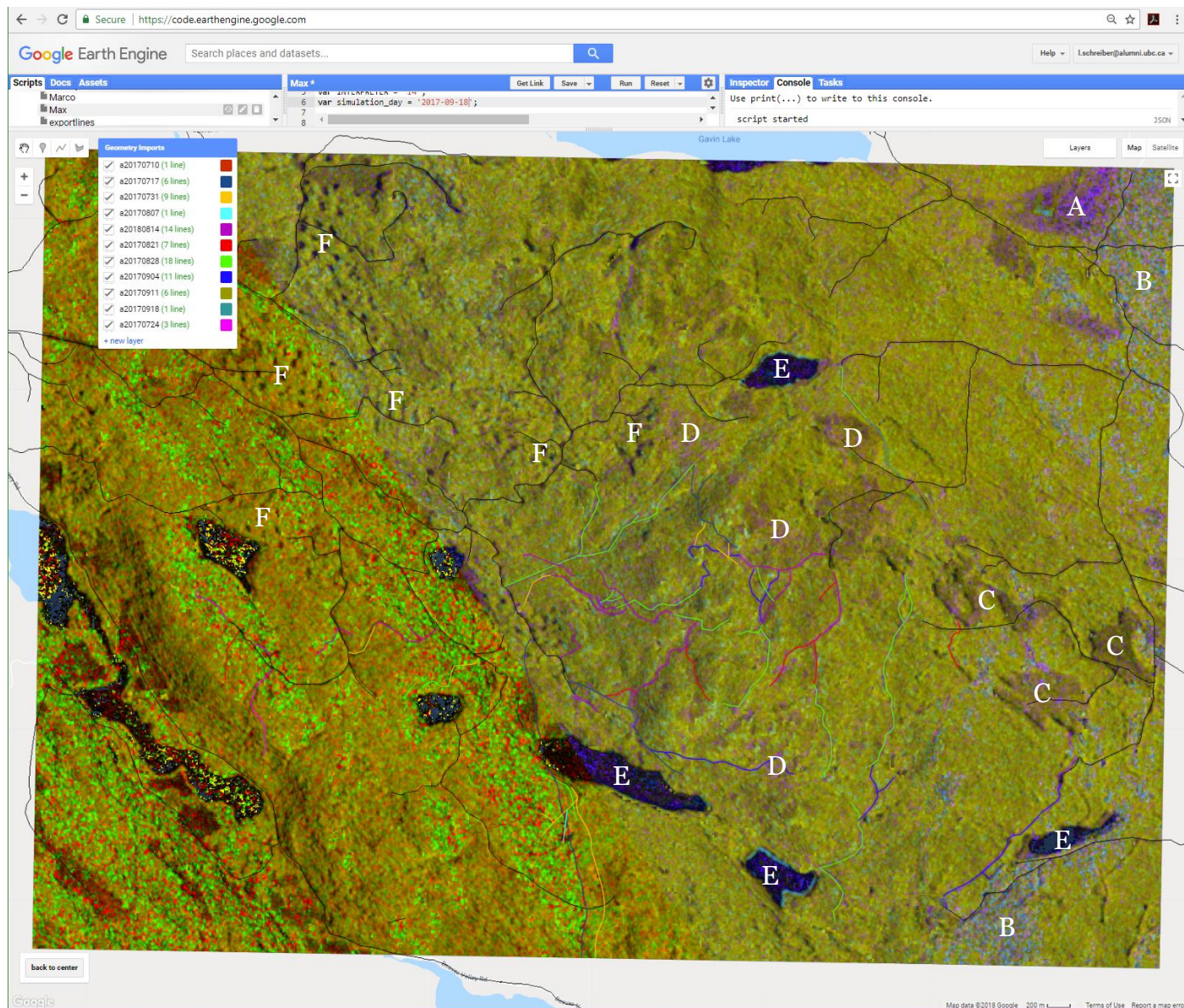


Figure 25a. For every Monday of the observation period, each interpreter was shown two composite images created from the time series up to that day. Dan in this example was shown a trend composite image for AoI West and a step composite for AoI East. The example shows the composites for the last day of the observation period, 2017-09-18. Overlaid are the linear features that he recognized, coloured by delineation date (legend in top left), as well as known pre-existing roads in black. For E-F, see text!

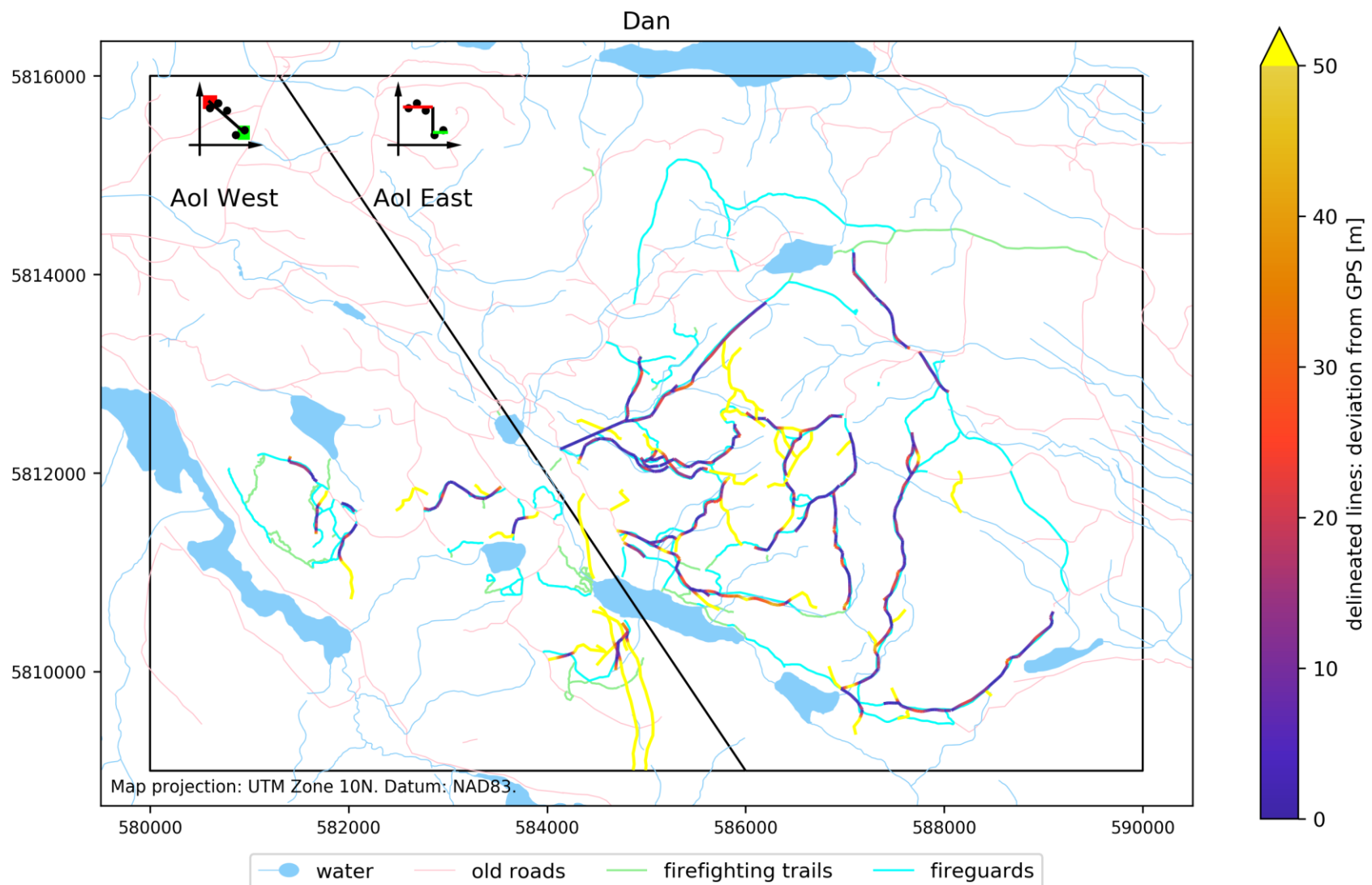


Figure 25b. The linear features delineated by Dan, coloured according to their distance from the GPS reference data.

How the different interpreters delineated linear features is shown by the example in

Figure 26. In both composite images, the fireguard north of the lake exhibits the two-line appearance predicted by the model for a north-south aligned fireguard explained in **Figure 7**, one line red/purple, and the other green/cyan (trend composite/step composite). This pattern is clearer in the trend composite image. Alice, Bob, and Erin detected that fireguard while Carol and Dan missed it.

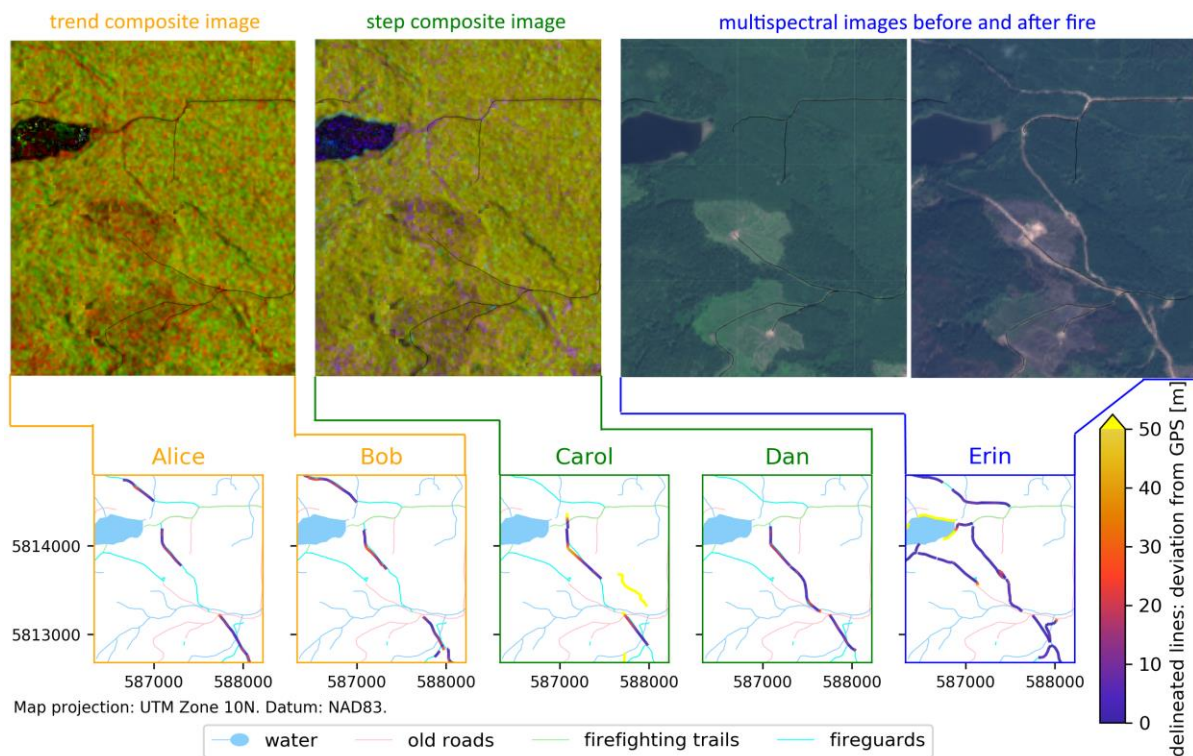


Figure 26. Example of the trend composite image, step composite image and multispectral image pair for disturbance interpretation zoomed into a small area. The black lines in the top row represent the roads mapped before the fire had started. The bottom panels show the lines detected by the image interpreters from the above or earlier images. These are coloured according to their distance from the GPS reference map, which is shown in cyan.

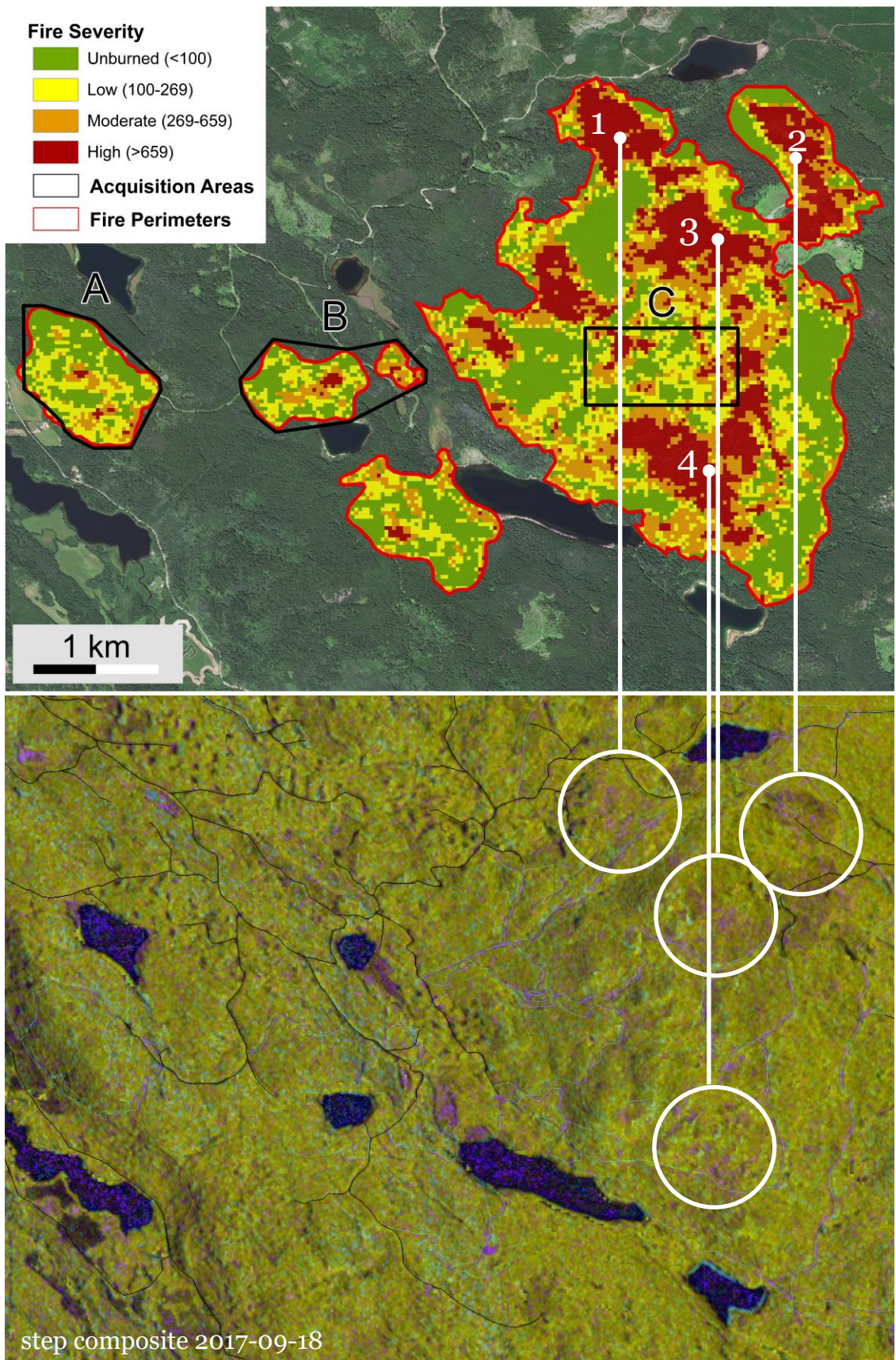
The fireguard going from the corner of the lake to the southeast corner of the image was partially delineated by Alice, Bob, and Carol while Dan and Erin delineated its

full length. In the composite images, it shows up as faint red and purple respectively. Finally, the fireguard that goes from the lake into the clearing was missed by Alice, Bob, Carol, and Dan.

2.3.2 Fire severity

In large regions of high fire severity, measured by RdNBR (Soverel et al., 2010), a backscatter drop was observed, which is evident by purple regions in the step composite images. For illustration the last step composite image, from September 18 is shown in **Figure 27**. Region 2 appears darker in the step composite because it is also the site of a pre-existing clearcut. Smaller areas of high fire severity do not have corresponding purple regions on the step composite image.

Figure 27 (next page). A fire severity map (top) (Arkin et al., 2019) compared to the step composite image from September 18 (bottom). Purple regions in the step composite correspond to the four larger areas of high fire severity. The burn severity classes in the burn severity map are based on RdNBR values from a Landsat image pair. The bottom image also shows pre-existing roads in black and the fireline reference layer in faint cyan. The trend composite image (not shown) looked similar with the high fire severity areas showing up in red. The top figure is reprinted with permission from Jeremy Arkin and Ignacio San Miguel.



2.3.3 Detection success

The detection errors are given in **Figure 28**, stratified by AoI, image interpreter, and source image type. The commission error, i.e. the proportion of features delineated by the interpreters that did not match fireguards on the ground, varied from 50% to 87% for maps based on the trend composites and from 30% to 68% for the step composites. This compares to a commission error of 2%–3% for conventional before-after comparison of multispectral images. The omission error, i.e. the proportion of fireguards that the interpreter failed to detect, ranged from 59% to 76% for the trend composites and from 43% to 76% for the step composites. Erin, who interpreted the multispectral imagery, missed 9% of the fireguards in AoI East and 16% in AoI West.

2.3.4 Spatial accuracy

For many applications, it is not only important whether new features are detected but also how accurately their location can be determined. Apart from very few exceptions, all new features were delineated within 50 metres of the reference. For the automated accuracy assessment, I had chosen this 50-metre distance as the threshold for correct/incorrect delineation.

When delineating based on a Sentinel-2 multispectral image, a mean spatial accuracy of 5–6 metres was achieved (**Figure 28c**). Based on the trend composite image, the mean deviation varied from 8 to 15 metres based on AoI/interpreter combination. For features delineated from the step composite image, the mean

deviation was between 11 and 16 metres. These values should be understood in the context of the pixel size of 10x10 metres for both Sentinel-1 and Sentinel-2.

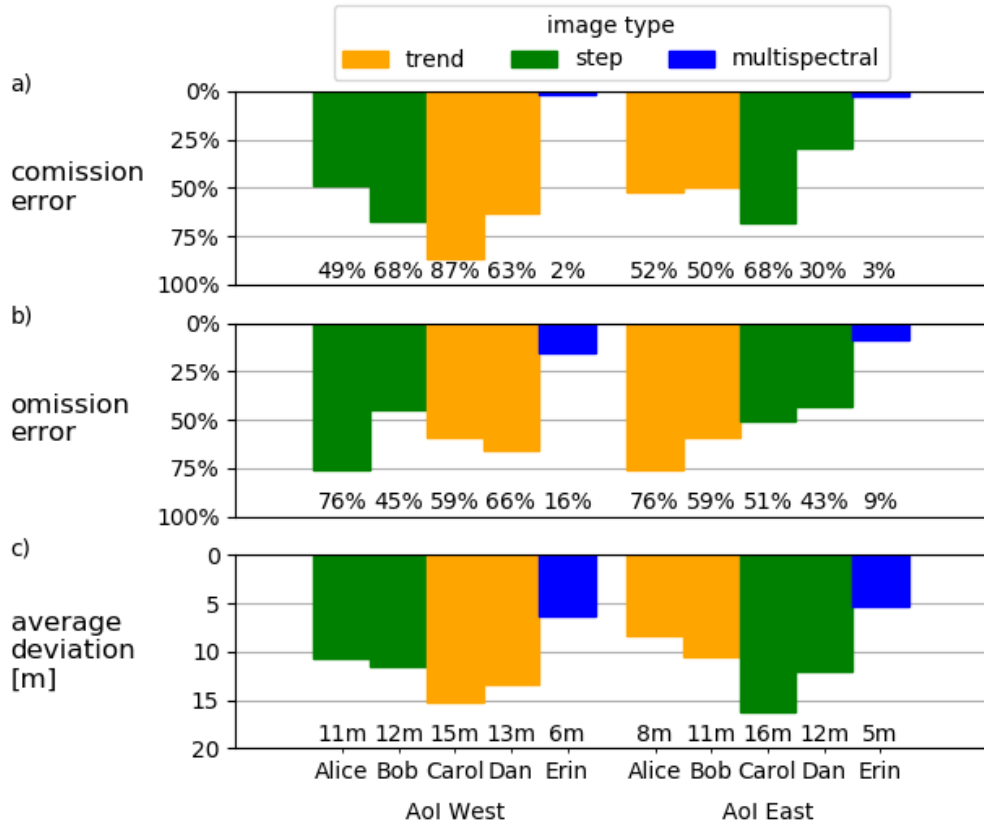
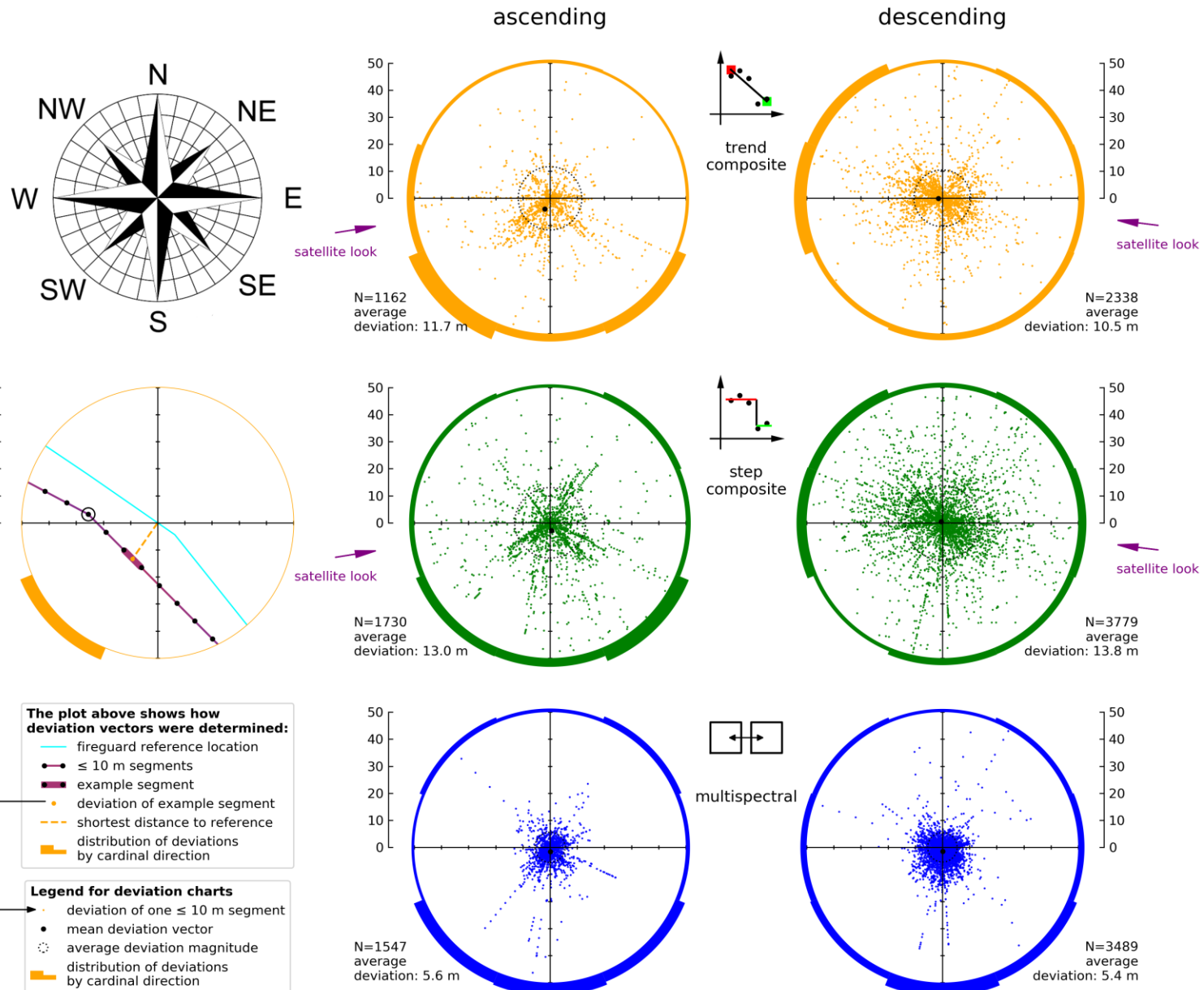


Figure 28. Detection accuracies for disturbance detection based on a linear-fit composite image derived from the SAR time series (orange), a single-step composite image (green), and before-after comparison of multispectral images (blue). Panel a) shows the commission error, i.e. the proportion of lines on the interpreter's map that did not correspond to a new linear feature on the ground. Panel b) shows the omission error, i.e. the proportion of fireguards that went undetected. Panel c) shows the average distance of the delineated features from the road centerline measured by GPS.

The results of an analysis of deviation vectors are shown in Error! Not a valid bookmark self-reference.. The poorest directional bias was 5.1 metres towards south-west for Carol/AoI West. For the same image/AoI combination, Dan's bias was 2.2 towards south. These values are well below one pixel (10 metres). Directional patterns in the deviation vectors due to relief displacement would not necessarily lead to an overall bias over one AoI but they should be visible in the scatter plots and radial histograms of Error! Not a valid bookmark self-reference.. However, all discernable patterns are consistent with only a single feature being delineated at an offset. Hence, there is no evidence of a systematic directional bias.

Figure 29 (next page). Offset of detected fireguard center geometry from reference geometry measured with GPS. The crosshairs represent the respective fireguard segment center (or firefighting trail segment center). Each dot in the scatterplots is the deviation vector (in metres) corresponding to a <10 m segment of the reference geometry. It represents the smallest distance from the midpoint of the segment to a line on the interpreter's map. The histogram on the outside of the circle shows the number of data points in the respective cardinal direction, weighted by the deviation magnitude and the segment length. The histogram buckets are the cardinal directions (E, ENE, NE, NNE, N, etc.) with respect to grid North (on UTM 10N). The black dot is the average of deviation vectors. The dotted circle and the distance printed in the corner is the average magnitude of these vectors. These averages are weighted by segment length. The scatterplots were produced for each interpreter and separated by AoI.
The scatter plots show no patterns that would be indicative of a directional bias in the images or the way they were interpreted. There are only patterns of spatial autocorrelation such as in the East-South-East sector of the bottom left scatter. These correspond to consecutive road segments, which deviate in the same direction.



2.3.5 What influenced detection rates?

In this section, I investigate the factors that influenced how readily features were detected. First, I show the situations that led to commission errors (false positives). Then, I wanted to know if the side-looking imaging geometry and the resulting relief displacement affected the detection rate. To find out, I investigated how fireguard direction and terrain steepness correlated with detection success.

Many situations can lead to the false delineation of linear features that appear in the imagery but do not correspond to new firelines on the ground. **Figure 30** illustrates two landscape features that were mistaken for fireguards. Often the interpreters mistook old clearcut edges for fireguards. Sometimes they mistook streams for new fireguards.

In addition, two types of mosaicking artefacts led to false positive delineations. One was at the boundaries between composites created from a substantially varying number of base images. The other common artefact was thermal noise at screen boundaries. Since the summer of 2018 when the delineation was done, the Earth Engine team has greatly improved the thermal noise removal algorithm. Hence, these artefacts do not occur anymore when the compositing is reproduced. Furthermore, Bob and Erin delineated lakeshores. Finally, there were many instances of false positives that cannot be attributed to the aforementioned mechanisms. See the yellow lines in Appendix D for all false positives.

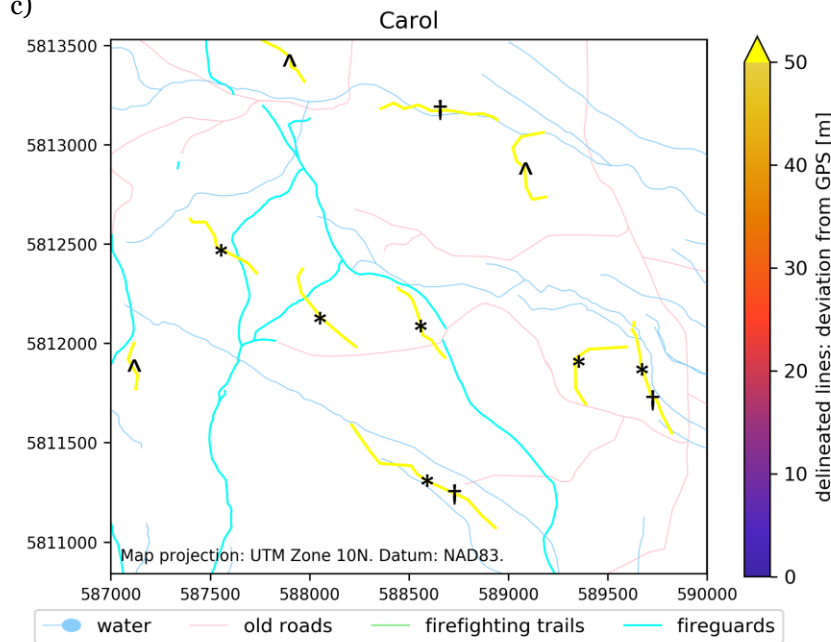
a) multispectral image from July 8



b) step composite image from July 14



c)



- * delineated clearcut edge
- † wrongly delineated stream
- ^ reason for wrong delineation unknown

Figure 30.
Examples of situations that led to delineation of

linear features that did not correspond to firelines. The images show delineation up to July 14. Image (a) is a Sentinel-2 image of the landscape on July 8. Image (b) is the step composite image that was shown to Carol assembled from data from June 19 to July 14. The white areas are pixels that did not have enough imagery to fit a step function to the time series. The dark blue lines show the lines delineated by Carol on July 10, and the light green lines show lines added based on this image from July 14. Map (c) shows the features wrongly delineated by Carol in yellow. Up to July 14, there were no fireguards in this area. The black symbols indicate the reasons for wrong delineations. These are explained on the right side.

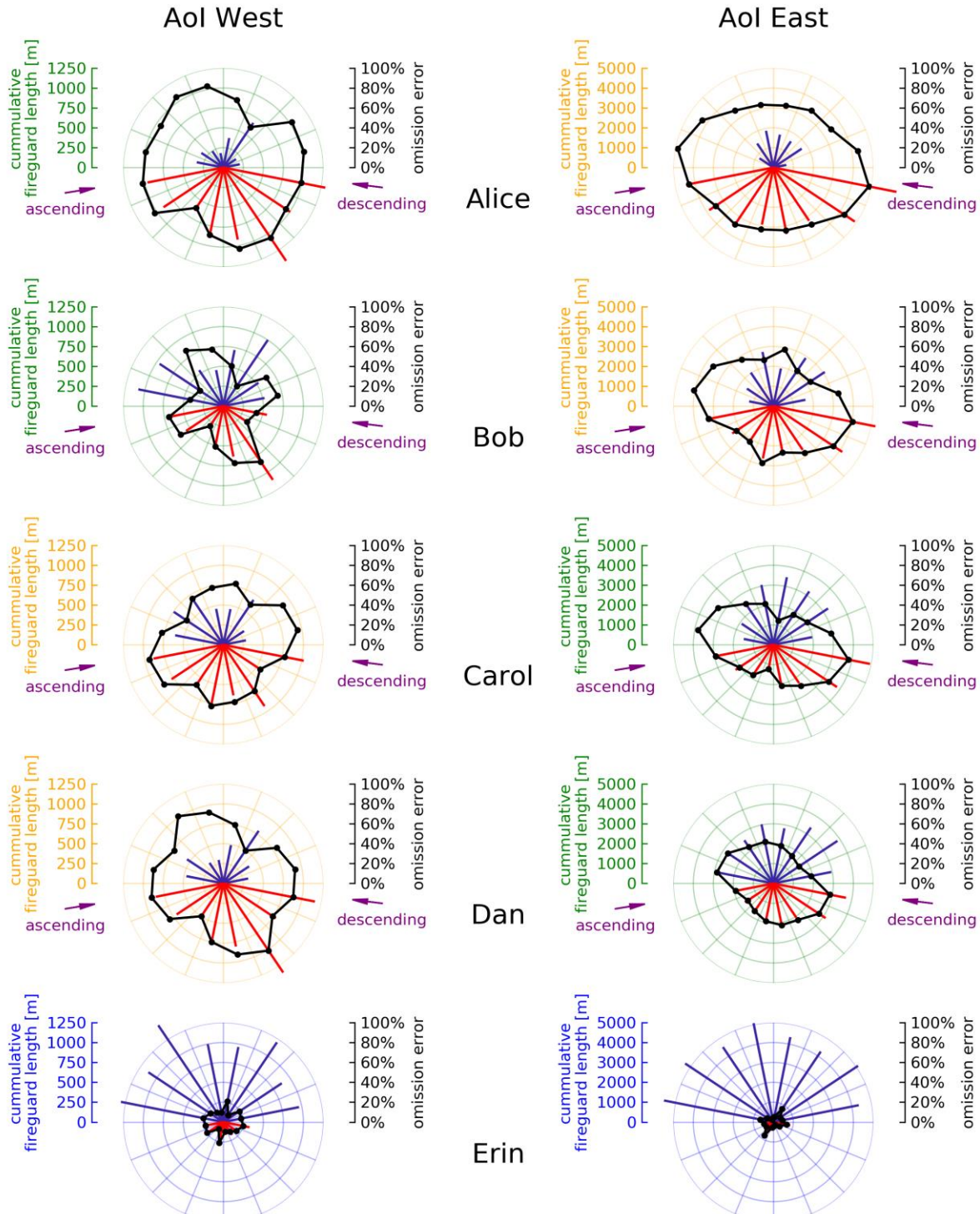
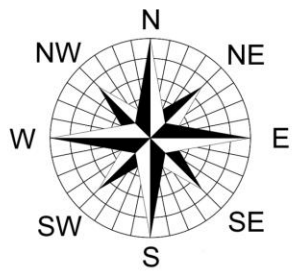
Figure 31 illustrates the omission error as a function of fireguard orientation. In AoI East, the omission error rate showed a maximum for fireguards oriented from west-northwest to east-southeast.

Figure 32 shows the detection rate as a function of slope steepness. For flat terrain up to 3 degrees, the detection rate was close to half the overall detection rate for the SAR time series composites. For the trend composite images, it decreased from 33.3% to 19.0%, while for the step composites it went from 50.4% to 28.4%. For the remaining steepness bins, the detection rate did not deviate significantly from the overall detection rate.

Figure 31 (next page). Each graph shows how many fireguards were detected as a function of the fireguards' direction. Note that the possible fireguard directions only span a semi-circle because there is no difference at all between a fireguard going from South to North and one going from North to South. Therefore, opposite blue and red lines correspond to the same direction bin, and the omission error line is point-symmetric with respect to the center. The lines show the total length of detected (blue) and undetected (red) fireguards by fireguard direction. The black lines show the omission error for each direction, i.e. the missed fireguard length as a fraction of total fireguard length. That is, the combined length of each red-blue line represents the cumulative length of the fireguards in that sector, and the black dot (omission error) indicates what proportion of that line is red. Each line represents the cumulative length of fireguard segments oriented in a specific direction. E.g., the first bin includes all segments with one end pointing towards north and up to 11.25 degrees further east (with the other end of the segment pointing towards South and up to 11.25 degrees more west). The purple arrows indicate the two possible satellite view directions. The directions are given with respect to the UTM 10N grid (as opposed to true North). The graphs are stratified by AoI and image interpreter.

● omission error
— length of delineated fireguards
— length of missed fireguards

□ image type
■ trend composite image
■ step composite image
■ multispectral image



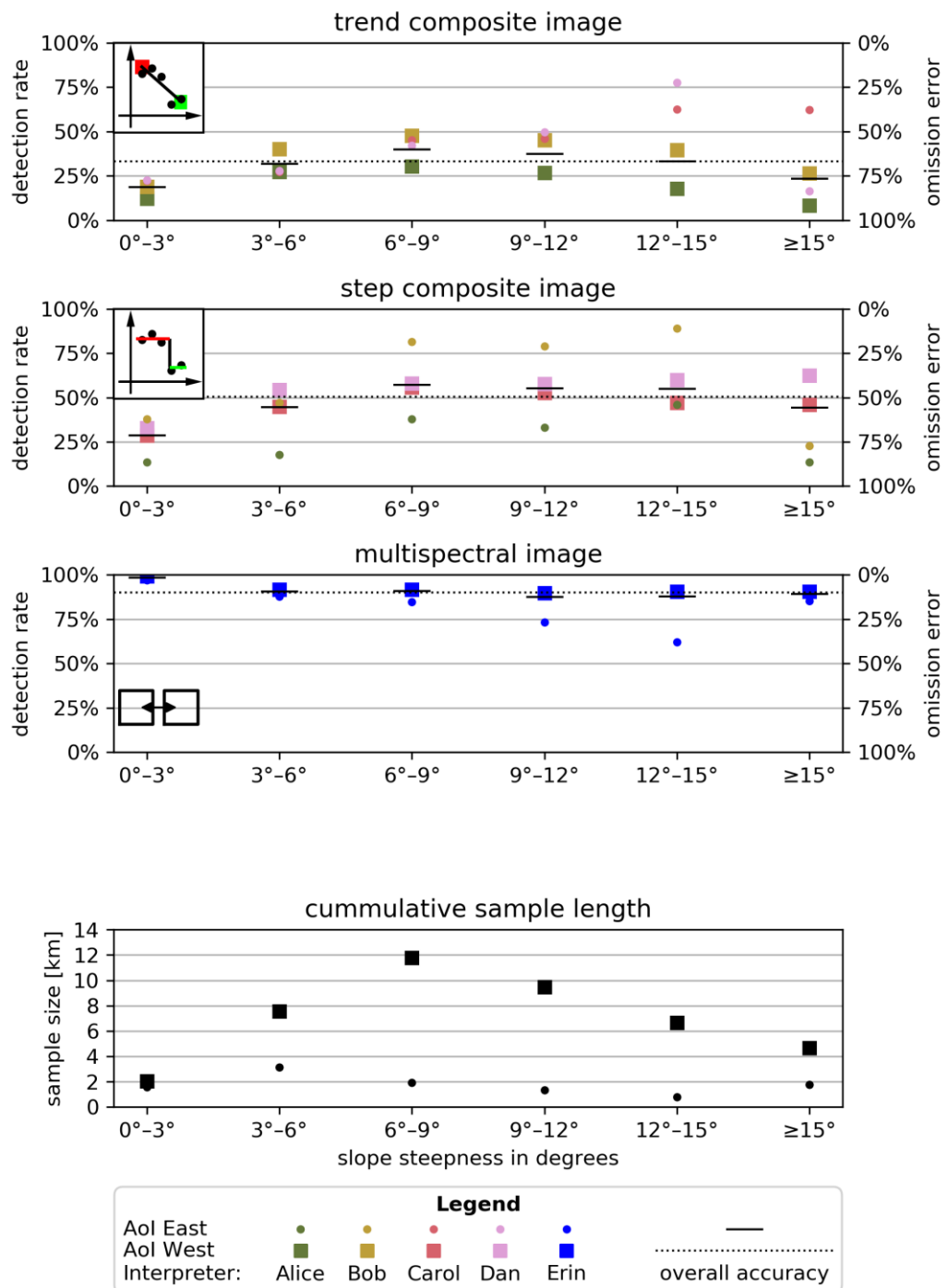


Figure 32. The top three graphs show the detection accuracy stratified by slope steepness bins for each combination of AoI and image interpreter as well as the overall detection accuracy as horizontal lines. The bottom graph shows the sample length by bin which applies to the top graphs. This data is printed in greater detail in Appendix E.

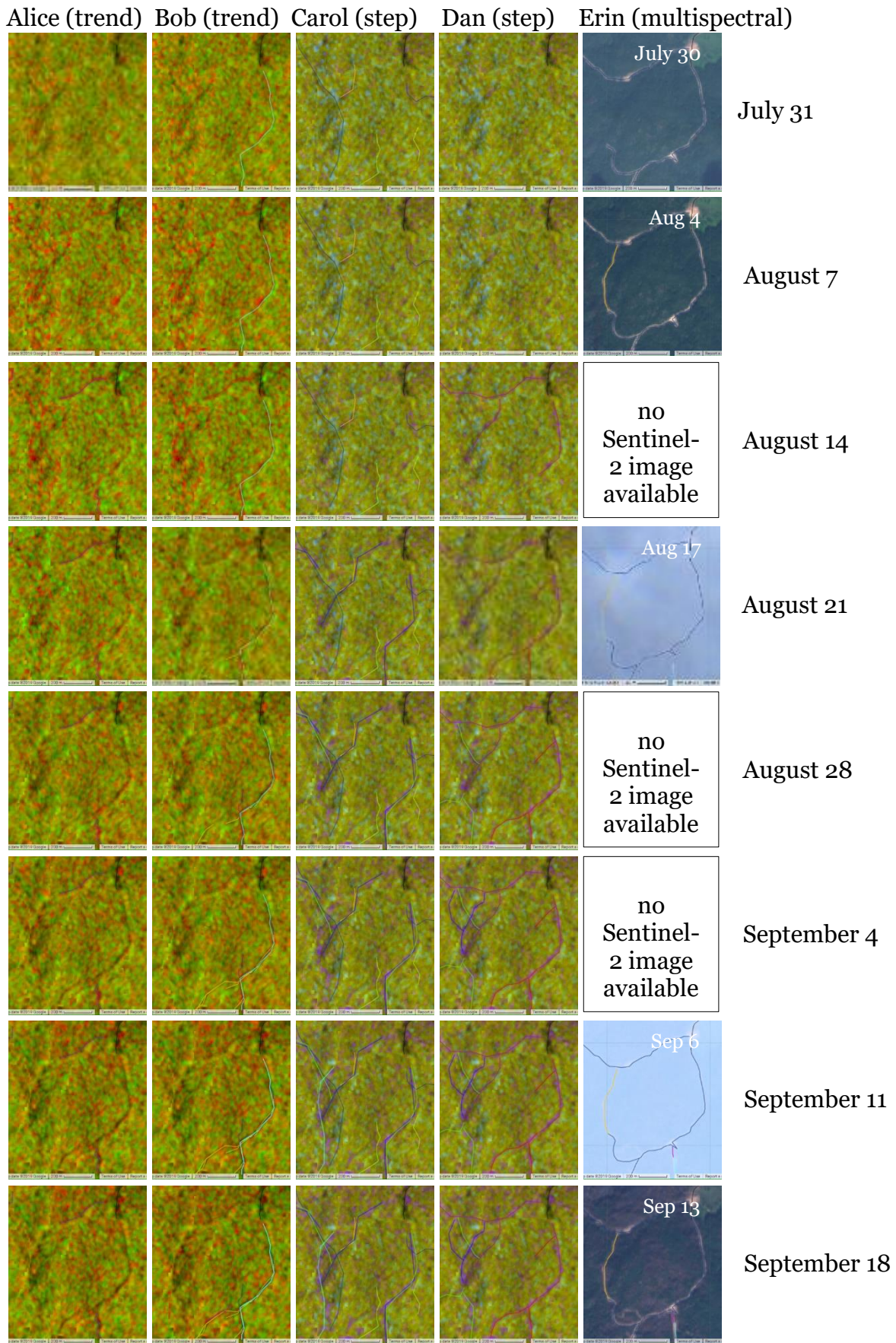
2.3.6 How quickly were fireguards detected?

Figuring out how long it took to detect fireguards was difficult because there was no reference data regarding timing available. Nevertheless, an estimate of detection lag could be derived by comparing the delineation data from the different image types. To aid in readability, in this section I use tenses as if the delineation had occurred in real-time. Note that the delineation was in fact simulated well after the wildfires took place.

There was only one fireguard for which it was possible to derive its construction time within a few days' accuracy based on the multispectral images. I investigated how long it took the interpreters to detect this specific fireguard. The composite images and multispectral images of the area for the different delineation dates are shown in

Figure 33. The interpreters who looked at trend composite images (Alice and Bob) missed this fireguard completely. They had not delineated it by the end of the observation period on September 18. Carol delineated the fireguard on September 11, 5–6 weeks after it was constructed. Dan detected it on September 4, with a 4–5 week lag since it was established.

Figure 33 (next page). Timeline analysis of the detection efforts for a small area. The fireguard in the left of the images was constructed between July 30 and August 4. This is evident when comparing the top right image and the one below, which were taken on these respective dates. The remaining images show how this fireguard and fireguards close by appeared to the interpreters over time. The coloured lines indicate what the interpreters delineated.



The two multispectral images in the bottom right (September 6 and 13) show a fireguard in the bottom center-right which was not present in the August 7 image. Erin detected this fireguard on September 11. The other interpreters were faster. Working from a trend composite image, Alice and Bob detected this fireguard on August 14, at most 10 days after it was constructed. Looking at a step composite image, Carol and Dan delineated this fireguard one week later on August 21, no more than 17 days after firefighters put in the fireguard.

A second example of quick delineation of a fireguard was also apparent. At the southwest edge of the west-most fire, a fireguard was constructed sometime after July 8. Carol already detected this fireguard on the trend composite image assembled on July 14, at most 6 days after the fireguard was established. This fireguard was not detected by the other interpreters examining the time series composite images: Alice, Bob and Dan. The images that the interpreters looked at are given in **Figure 34**.

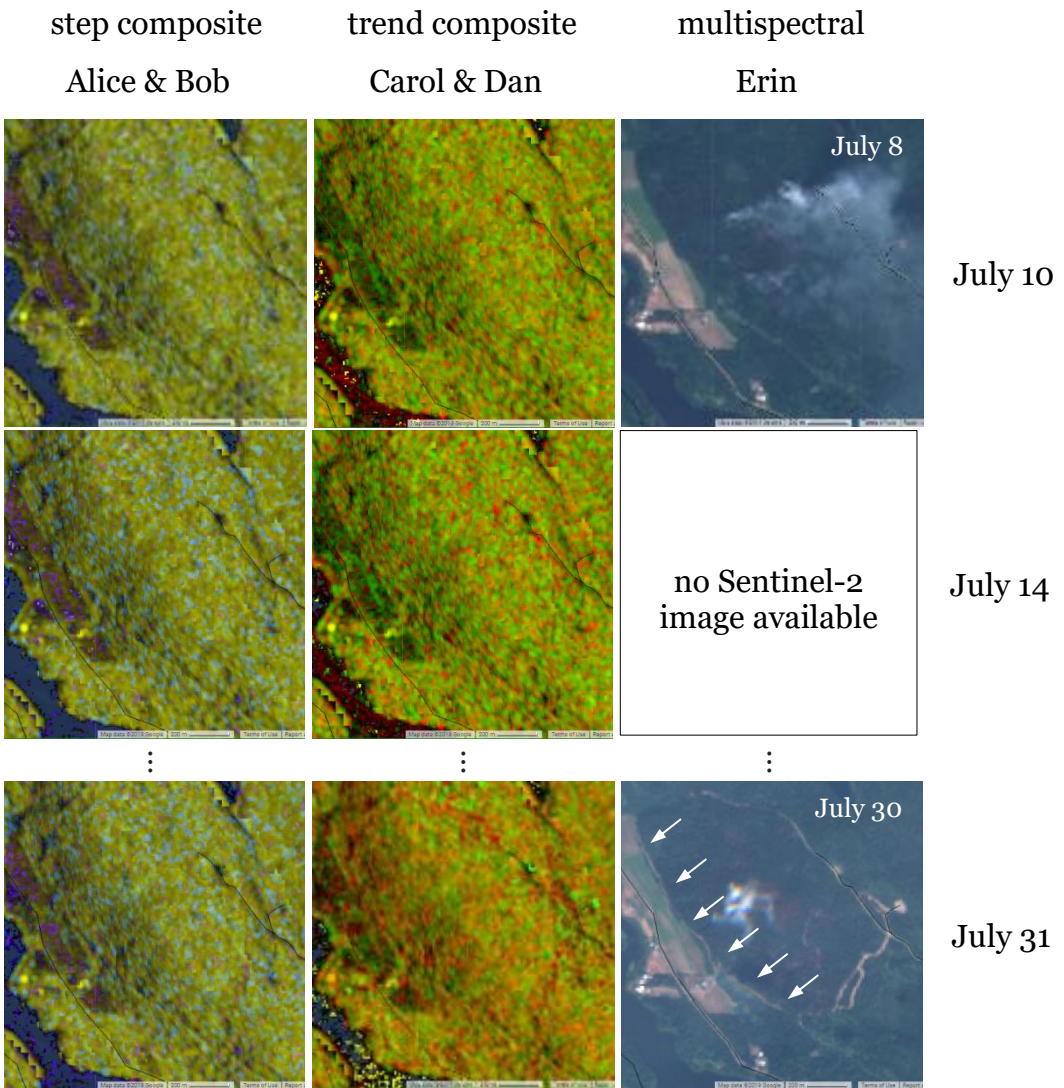


Figure 34. The fireguard highlighted in the bottom-right image from July 30 was not present on July 8. Yet, Carol already delineated it when looking at the trend composite from July 14 (the center image). Alice, Bob, and Dan did not detect this fireguard. Erin delineated it on the next available multispectral image from July 30.

2.3.7 How much time was required for delineation?

The interpretation logs (Appendix C) show that it took the interpreters between 2 and 63 minutes to create one map of new features based on one change composite image of 7000-hectare study area. The average delineation time per map ranged from 8 minutes for Carol and Erin to 23 minutes for Bob (see **Figure 35**). The average time it took to delineate one change composite image of the study area was 17 minutes.

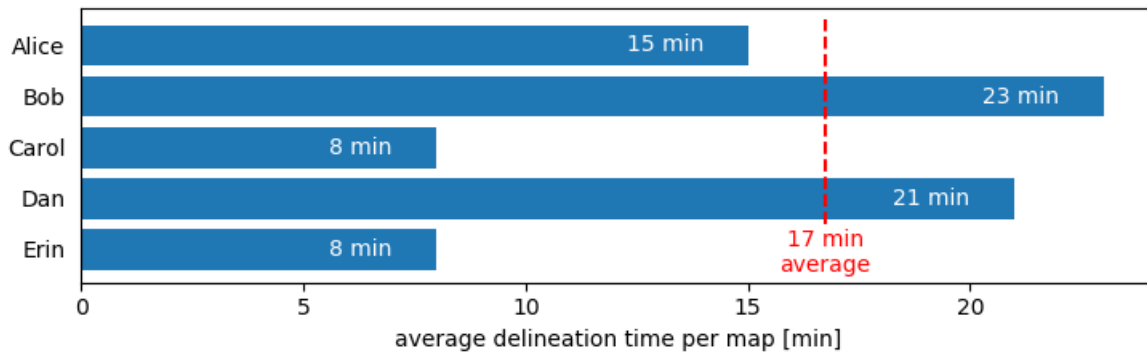


Figure 35. The bars show the average time it took an interpreter to create a map of new features from on change composite image (or before-after pair of multispectral images in the case of Erin).

2.4 Discussion

2.4.1 Accuracy

The accuracy (omission error, commission error, deviation) of maps produced by delineating SAR time series composite images was substantially worse than the accuracy of the map produced by conventional before-after comparison of multispectral images. The lowest commission error among the maps created from SAR time series composites was 43%. This was for the map that Dan produced of the fireguards in AoI East based on a step composite image. Therefore, this method is only suited for applications, where it is sufficient to get a partial view of the situation on the ground, but where it is important to get that view within a few weeks. If a cloud-free multispectral image acquired at sufficient spatial resolution is available for an area and timeframe of interest, it should be used instead, as a multispectral image is easier to interpret and more accurate.

The ratio of false positives in the best map based on delineation of SAR time series composites (the map mentioned in the previous paragraph) was 30%. It is crucial to note that the interpreter (Dan) evidently knew in which general area to expect fireguards, as he did not delineate any features far away from the fires. Carol looked at the exact same imagery and produced a map containing 68% false positives. The false positive rate of at least 30% renders the method presented in this study unsuitable for detecting disturbances that are more dispersed on the landscape. This is because the number of false positives generally correlates with the size of the study area, while the number of correctly detected features correlates with the number of

features on the landscape. Hence, if the density of target features were lower, they would be overshadowed by false positives. Second, the large difference in commission error between Carol and Dan shows the influence that subject matter knowledge has on interpretation success. While both Carol and Dan had experience with interpreting multispectral satellite imagery, Dan had wildland firefighting and extensive forest practice experience. That could have enabled him to make better sense of the processes that were changing the landscape.

2.4.2 Fire severity

Surprisingly, the widespread wildfires were barely visible in the time series composite images. That is, only the centers of large areas of high fire severity featured a backscatter drop in the time series, which is signified by purple colour on the step composite image. That means that only very high severity fire leads to a backscatter drop in SAR imagery, rendering the methods introduced in this thesis unsuitable for wildfire damage tracking.

2.4.3 What influenced detection rates?

In Section 2.3.5, I investigated, among other issues, what led to the delineation of false positives. Four mechanisms were identified that explained part of the false positives: delineation of clearcut edges, streams, lake shores, boundaries between regions with differing base image number, and scene edge thermal noise. The first could have been avoided by closer consultation of the available multispectral imagery. Indeed, Dan never made this kind of mistake. Wrong delineation of streams and lakeshores may be due to differences in water levels, which have a large

influence on SAR backscatter. This problem could possibly be alleviated by providing a streams map to the interpreters. However, linear features such as fireguards look similar to streams on SAR imagery and hence it is difficult to distinguish high water levels in a stream from a linear road feature created right next to a stream. The issue of base image numbers could be addressed by making the observation time longer. The problem of scene edge thermal noise is largely resolved by updates that have been made to Earth Engine in the meantime.

Campbell & Wynne (2011) identified three factors that make the interpretation of aerial and space imagery more difficult than the interpretation of conventional everyday photographs: 1) objects are depicted from straight above, a perspective that is seldom encountered in real life or photography; 2) other wavelengths than those in the visible spectrum are used; 3) the landscape is depicted at unfamiliar scales and resolutions. All three factors apply to this study, though all image interpreters had experience with interpreting remotely sensed imagery, limiting the adverse impact of factors (1) and (3). The most important complicating factor was the use of C-band radar (2) which none of the interpreters were familiar with.

When completing image interpretation tasks, individual image interpreters sometimes exhibit a bias towards under-delineating or over-delineating features (Chiang et al., 2007). In this study, interpreter Alice only delineated a few features on the map, effectively under-delineating the fireguard network, which led to a high omission error. On the other hand, Carol's map was over-delineated, and hence exhibited a high commission error. These biases can be seen by the large discrepancy

between omission and commission error of each individual interpreter (**Figure 28**) or by examining Alice's and Carol's map in Appendix D.

Furthermore, I explored if the combination of side-looking radar and land cover/terrain geometry affected detection success. In AoI East, fireguards oriented close to the west-Northwest (=east-Southeast) direction were missed significantly more often than those close to the north-Northeast (=south-Southwest) were. This can be explained by the lack of a corner reflector effect when the fireguard is roughly aligned with the range direction. However, this pattern was not reproduced in AoI West. It has to be noted though that AoI West was much smaller.

I also investigated the impact of slope steepness on detection success. For the maps based on SAR time series composites, I found a substantially lower detection rate (higher omission error) for flat slopes with an angle up to 3 degrees. This difference was pronounced across all interpreters and AoIs. However, for the maps based on multispectral images, the detection rate for slopes between 0 and 3 degrees was substantially higher than the average. The high error rate for SAR composite images of flat terrain is surprising. The literature (Ackermann, 2015; Reiche et al., 2016) only suggests difficulties in rugged terrain. One also has to note that only 3.5 km of fireguards were in terrain less than 3 degrees steep. Hence, this could be a chance correlation. I cannot think of a physical mechanism that would explain why fireguards in flat terrain were more difficult to detect than those on steep slopes were. To summarize, although flat terrain correlates very clearly with lower detection rates on maps created based on SAR time series composite images, it remains unclear whether this relationship is causal.

Chapter 3: Conclusion

3.1 Answers to the research questions

- 1. What spatial accuracy is achieved when delineating fireguards based on a trend composite image, step composite image or multispectral image pair?*

In summary, the accuracy of the maps produced based on before-after comparison of multispectral images were substantially more accurate than those based on time series composites. The best map produced based on a SAR time series composite was the one Dan produced of AoI East based on a step composite image. It featured a commission error of 30%, an omission error of 43%, and an average spatial deviation of 12 metres (about the same as the pixel size of the imagery). The comprehensive answer to this research question is given by **Figure 28**.

- 2. What factors influenced detection success?*

Detection was substantially dependent on the analyst undertaking the image interpretation. From my results, it remains unclear whether fireguard orientation and slope steepness influenced detection success.

- 3. How quickly could new fireguards be detected based on a trend composite image or a step composite image?*

The shortest observed detection lag for delineation based on a trend composite image was 6 days or less. The best delineation lag for step composites was up to 17

days. A typical delineation lag was 4–6 weeks. A statistical analysis of delineation lags was not possible due to lacking reference data.

Besides the answers to the three research questions, two more answers to interesting questions were found. One, the described change compositing and visualization method was found unsuitable for fire severity tracking. Two, the average time it took to delineate an area of 7000 hectares was 17 minutes.

3.2 Limitations

A number of limitations have to be considered when interpreting the results of this study. The first two concern the quality of the SAR imagery in Earth Engine. In particular, there were issues with thermal noise near scene borders, and data availability was delayed by several days. Furthermore, the GPS reference data may contain inaccuracies. Next, interpreter knowledge as well as the low number of replicates impacts my ability to draw conclusive recommendations. Furthermore, the results on detection speed are anecdotal in nature. Finally, the results for this study area do not necessarily apply to other areas.

The Sentinel-1 scenes provided in Earth Engine included a significant amount of thermal noise near scene borders. I found an ad-hoc solution to remove most border noise, but that method also removed a small amount of valid data (Section 2.2.2). Between image processing for this thesis and writing, the Earth Engine team has implemented the *GRD Border Noise Removal* step from the Sentinel-1 toolbox in preprocessing the full Sentinel-1 collection (personal communications, Simon Ilyushenko, Google Earth Engine Developers forum, S1 preprocessing, January–March 2018). This will make future work with Sentinel-1 time series easier.

After a satellite of the Sentinel-1 and Sentinel-2 constellations captures a scene, it typically takes 1–4 days to deliver it to a ground station, process the scene, and ingest it in Earth Engine. However, often satellite scenes are not ingested in Earth Engine for many days. For instance, one Sentinel-2 scene, that was sensed during the study period and that covered the study area, was only available in Earth Engine in

September 2018, so it could not be included in the near-real-time simulation conducted in August 2018. Then, for 3 out of 7 Sentinel-2 scenes used in the simulation, it is unclear whether they were available in the study period. Similarly, out of the 51 Sentinel-1 scenes used in the simulation, only 22 were certainly available in Earth Engine within 4 days of sensing. The rest could have been ingested up to 70 days after sensing. I could only find an upper bound for when a specific scene may have been ingested in Earth Engine. Therefore, I did not account for the ingestion lag in the simulation of near-real-time disturbance detection. Hence, availability of imagery in Earth Engine is a significant constraint on applying my method in near real-time.

The ground truth data was collected with recreational GPS receivers. This typically achieves a mean accuracy of 2.3 metres (Ucar et al., 2014), which has to be considered when interpreting the deviation measures computed in Section 2.3.4. Furthermore, it is possible that fireguards were missed or that features other than fireguards were included when collecting the ground truth data.

The set-up of the near real-time disturbance detection simulation made little use of the local and operational knowledge typically available to GIS analysts. Should this method be applied operationally, analysts in industry or government with experience or knowledge of firefighting and/ or knowledge of the local area who utilize this method would likely make significantly fewer commission errors than the interpreters in the simulation. In fact, out of the four interpreters who delineated based on the SAR time series composites, Dan, who had been to the research forest

after the fire, made significantly fewer commission errors than the other three who were unfamiliar with the area.

The low number of AoIs and interpreters made it difficult to establish whether differences in the results were due to differences in interpreter skill, differences in the image types, local differences between the AoIs, or random chance. For each type of time series composite, there were two image interpreters for each of the two AoIs, and a fifth interpreter for the multispectral images of the whole study area (see Section 2.2.7). Effects that repeatedly occurred over an AoI or for one image type could confidently attributed to these. In contrast, for instance effects that were found on only one of the interpreter's maps were difficult to attribute.

To determine the detection speed (Section 2.3.6), no reference data of fireguard construction dates was available. Hence, no statistical information on detection speed could be derived.

The conclusions I reached regarding the accuracy and detection speed cannot necessarily be extrapolated outside this case study. They can only serve as a benchmark for what is possible. Various attributes of the landscape and the detection system can significantly alter the success of this method. For instance, ecosystems with less pronounced phenology such as moist tropical forests may allow for easier monitoring due to lower noise in the data from seasonal variations. Second, snow cover significantly alters the SAR backscatter response. Where snow cover varies throughout the observation period, it would add additional noise. Third, high forest height and density may prevent the microwaves from reaching the fireguard or road

surface altogether. Fourth, SAR is not suitable for landscape monitoring in terrain that is steep enough to cause significant foreshortening and layover. Fifth, for different disturbance geometries different microwave reflection mechanisms are dominant leading to deviating results. For example, while corner reflector and radar shadow effects made the fireguards stand out on the SAR composite images, these effects play less of a role in clearcuts except for clearcut edges oriented in the right direction. Sixth, the revisit frequency of the Sentinel-1 satellites varies across the world (European Space Agency, 2016). While the revisit frequency for both ascending and descending passes is 12 days at the study site, it is only 6 days in Europe, the Mediterranean, and Hawai‘i, leading to faster change detection. Conversely, many parts of the world, including most of the regions with tropical rainforests, have only either ascending or descending Sentinel-1 passes, which would roughly double detection times compared to the study site. Finally, interpreter knowledge and interpreter skill play a large role in the success of any monitoring system. When applying a similar method to a different application, it is crucial to verify the accuracy for that application.

3.3 Potential applications

Due to the high observed error rates, potential applications of the methods described in this thesis are limited. However, where no other data (e.g. optical or ground-based) is available, monitoring of these change composite images may prove useful in approximately tracking the progress of crews constructing fireguards, roads, or other linear features. In doing so, one has to contend with the difficulties introduced by rugged topography and a complex forest structure, which were present in this case study.

The ability to track road building may open an avenue to detecting illegal logging, as most logging operations start with road building. That would open the possibility of detecting a logging operation early on. Naturally, it remains to be seen whether the methods described in this thesis can be transferred to tropical forests where most illegal logging takes place.

Finally, the change visualization approach using change functions fit to each pixel time series may be used for monitoring all kinds of dynamic land cover processes. Processes that come to mind because of their high contrast in SAR imagery include sea and land ice dynamics, agricultural land use, building construction, and wetland water extent variations.

3.4 Recommendations

To come up with an application for land cover detection that is robust and effective in practice, the following improvements should be made.

First, data quality is key to time series compositing, as quality issues in just one image affect the entire time series. To that end, the improvements made by the Earth Engine team towards better border noise removal are crucial. Still more efforts should be made to decrease the lag between image download from the satellite and Earth Engine ingestion described in Section 3.2.

Second, development of any change detection application should be done in close cooperation with the intended users. It is crucial to combine the SAR time series composites with other relevant datasets to provide context. For instance, when monitoring fireguard construction, important circumstantial clues could be provided to the end user by overlaying daily active fire locations from the *Fire Information for Resource Management System* (FIRMS) (NASA's Earth Science Data and Information System, n.d.) on top of the change composite.

Third, it would be beneficial to develop methods to deal with pixels where the time series only includes a few observations. This issue is apparent in **Figures 18a, 25a and 30b**.

Another potential improvement is to combine the change visualization approach presented in this thesis with Bayesian modelling for change detection. Reiche et al., 2018 demonstrated the use of Bayesian updating to achieve confident, near real-time, wall-to-wall detection of forest cover loss. They used this method to

characterize how tropical forest cover loss and wildland fires relate temporally. For instance, the backscatter value before a potential step in the time series could be assigned to the red display band, the value after the step could be shown in green, and the Bayesian change probability in blue.

Where available, use of dual-polarized SAR imagery such as VV and VH could improve differentiation of land cover types as demonstrated in Reiche et al., 2018.

3.5 Designing a landscape monitoring system based on SAR time series

I have broken down the steps for designing a future landscape monitoring system that relies on SAR time series data. Throughout this process it is crucial to stay in touch with the potential users of the system, and to document the choices made. Furthermore, it may be necessary to go through several iterations where previous steps have to be adapted to accommodate changes in the requirements, constraints, design, or implementation of the monitoring system.

The algorithms developed in this thesis are available for use at:

<https://code.earthengine.google.com/d9d6c2oda92848922b873c5104eeaf52>

To use this link, users require an Earth Engine developer's account, which is free for researchers.

3.5.1 Dialog with users

The first step is to enter into a dialogue with the potential users of the envisioned monitoring system. This way one can ascertain the data users' overall needs and goals, their operational requirements, and how they would use the monitoring system.

3.5.2 Definition of requirements

Based on the dialog with users, one can define the requirements that the monitoring system has to fulfill. Example requirements for a windthrow visualization system could include:

- **Roo1:** The system shall flag the locations of new windthrow clearings larger than 0.5 hectares.
- **Roo2:** The delineation should have an omission rate of no more than 20%.
- **Roo3:** The delineation should have a commission error rate of no more than 40%.
- **Roo4:** The system shall flag the locations of clearings in under 4 weeks 90% of the time.
- **Roo5:** The system shall work in temperate conifer forests of the European Union with a terrain ruggedness index (Shawn Riley, Stephen D. DeGloria, & Robert Elliot, 1999) of less than 300 metres.
- **Roo6:** The visualization shall load within 2 minutes.

It is helpful to formulate requirements that conform to NASA's systems engineering checklist for requirements (Hirshorn, 2007).

3.5.3 Concept design of the monitoring system

Next, the parameters and setup of the monitoring system have to be chosen. In doing so, the requirements should be taken into account.

First, the time series data has to be selected. That includes the sensor, pass direction, and polarization. While Sentinel-1 is a good choice because it is free and incorporated in Earth Engine, other spaceborne or airborne sensors may be more suited for a specific task. For instance Airbus is successfully using TerraSAR-X data to monitor deforestation in the tropics (Airbus, 2019). If data from other sensors is used, it would have to be pre-processed and ingested in Earth Engine. To reduce the

salt-and pepper appearance that is typical for SAR imagery, one could apply a speckle filter. The choice of pass direction and polarization depends on what imagery is available in the monitoring area. Where both ascending and descending images are available, one can choose between combining them and filtering them as explained in **Figure 18**. While combining them doubles the density of the time series, it leads to very bright values in steep terrain. Where two polarizations are available, one can choose the one that is best able to differentiate the land covers of interest, or one can combine the two e.g. by adding them. If the function for summarizing the time series can deal with multivariate inputs (Bayesian modelling can do this), one can retain both polarizations, as opposed to combining them.

Second, one has to select a function that summarizes the time series at each pixel in no more than three values, to be assigned to red, green and blue respectively in the output summary composite image. For a continuous change such as growth, a line function is appropriate, while for sudden changes such as windthrow or logging, a single-step function or Bayesian updating (Reiche, Bruin, et al., 2015) is applicable. Other functions may be considered too.

Third, one has to choose the training (where applicable) and observation periods based on snow cover periods, phenology, data availability, and Earth Engine capacity (multi-year periods will exceed the memory limit in Earth Engine).

Fourth, ancillary data may be incorporated in the monitoring system. This can include maps of road networks, cutblock locations, forest extents, streams, et cetera, as well as remote sensing data such as active fire alerts or multispectral images.

Fifth, the mode of interpretation has to be set. For delineation in a complex landscape characterized by multiple change mechanisms, manual interpretation is the method of choice. In this case one has to select the image interpreter(s). Ideally, the interpreter would have full colour-vision, and be familiar with the type of landscape being monitored and with SAR imagery. Alternatively one could rely on an automatic approach to translate the summary image into a map. In this case the summary image may have more than three bands. An automatic delineation algorithm would have to be taken from the literature or developed in-house, and implemented in Earth Engine.

Sixth, innovations may be incorporated in the monitoring system. Perhaps a better way to deal with ascending and descending pass directions could be devised. One could account for seasonality when processing the time series (Reiche et al., 2018) (see link at the start of Section 3.53.3).

Seventh, one has to choose suitable validation data to assess the accuracy of any maps produced by the monitoring system. In the example of a windthrow monitoring system, this could be wind-thrown areas that are manually delineated from multispectral images in regions not obscured by clouds.

3.5.4 Building the monitoring system

After the monitoring system has been conceptualized, it has to be implemented as an Earth Engine application. The code linked to at the start of Section 3.5 is the basis for this. The code supports the creation of time series composites from Sentinel-1 data in VV or VH polarization, normalizing the time series data by season, filtering or

combining of ascending and descending pass directions, and the fitting of an unweighted trend function, single-step function, or impulse function to the data. Features that remain to be implemented include: other SAR data sources than Sentinel-1, other polarizations or combined polarizations, speckle filtering, Bayesian modelling or other summarizing functions than the three mentioned, visualization of ancillary data, and automatic delineation algorithms.

In addition, validation data has to be collected in the field or from multispectral imagery. Furthermore, in the case of manual delineation of the summary images, a delineation manual for the image interpreter(s) has to be written which should include multiple example of summary images of features of interest.

3.5.5 Testing

After implementation in Earth Engine, the visualization system should be tested in the area of interest or a similar region. Testing can already commence during implementation to allow for fine-tuning of some parameters of the monitoring system.

3.5.6 Delineation

Once all parameters are set and the monitoring system has been tested, the delineation effort can begin. During delineation it is helpful to keep a log with screenshots of interesting or anomalous features in the summary composite images. This is crucial in tracking the reasons for errors in the delineation and addressing them.

To speed up the delineation effort and avoid inefficiencies caused by the long loading times in Earth Engines, it may be best to download the summary composite images from Earth Engine and view them in a GIS software such as ArcMap or QGIS. This function is implemented with a button in the code linked at the start of Section 3.5. However, exporting of large areas is not possible due to memory constraints in Earth Engine, and exporting limits the ability to zoom. Hence, it depends on the application at hand whether image analysis directly in Earth Engine or offline is ideal.

3.5.7 Accuracy assessment

Finally, the maps produced by the interpreters have to be compared to the validation data to create an accuracy assessment report. Such a report should at least contain the omission and commission error rates. This allows users of the created maps to judge their quality.

References

- Ackermann, N. (2015). *Growing stock volume estimation in temperate forested areas using a fusion approach with SAR satellites imagery*. Cham: Springer International Publishing. <https://doi.org/10.1007/978-3-319-13138-2>
- Airbus. (2019). Starling verification. Retrieved April 11, 2019, from <http://www.starling-verification.com/#ourService>
- Arkin, J., Coops, N. C., Hermosilla, T., Daniels, L., & Plowright, A. (2019). Integrated fire severity-land cover mapping using very high spatial resolution aerial imagery and point clouds.
- Aronoff, S., & Petrie, G. (2005). Active sensors: radar and lidar. In *Remote sensing for GIS managers* (First Edit, pp. 245–258). Redlands, CA, USA: ESRI Press.
- Barsi, J., Lee, K., Kvaran, G., Markham, B., Pedelty, J., Barsi, J. A., ... Pedelty, J. A. (2014). The Spectral Response of the Landsat-8 Operational Land Imager. *Remote Sensing*, 6(10), 10232–10251. <https://doi.org/10.3390/rs61010232>
- BC Wildfire Service. (2017). Wildfires of Note - Prouton Lakes. Retrieved April 12, 2019, from <http://bcfireinfo.for.gov.bc.ca/hprScripts/WildfireNews/OneFire.asp?ID=662>
- Beckett, K. D. R., & Tyc, G. (2016). Systems and methods for enhancing synthetic aperture radar imagery. World Intellectual Property Organization. Retrieved from <https://patentscope.wipo.int/search/en/detail.jsf?docId=WO2016205406>
- Bey, A., Sánchez-Paus Díaz, A., Maniatis, D., Marchi, G., Mollicone, D., Ricci, S., ... Miceli, G. (2016). Collect Earth: land use and land cover assessment through augmented visual interpretation. *Remote Sensing*, 8(10), 807. <https://doi.org/10.3390/rs8100807>
- British Columbia Ministry of Forests. (2000). *S-100 (BC), basic fire suppression & safety, student workbook*. Victoria, BC: British Columbia Ministry of Forests.
- Bruzzone, L., Marconcini, M., Wegmüller, U., & Wiesmann, A. (2004). An advanced system for the automatic classification of multitemporal SAR images. *IEEE*

Transactions on Geoscience and Remote Sensing.

<https://doi.org/10.1109/TGRS.2004.826821>

Campbell, J. B., & Wynne, R. H. (2011). *Introduction to Remote Sensing FIFTH EDITION. Uma ética para quantos?* <https://doi.org/10.1007/s13398-014-0173-7.2>

Chiang, M. F., Gelman, R., Jiang, L., Martinez-Perez, M. E., Du, Y. E., & Flynn, J. T. (2007). Plus disease in retinopathy of prematurity: an analysis of diagnostic performance. *Transactions of the American Ophthalmological Society, 105*, 73-84-5. Retrieved from <http://www.ncbi.nlm.nih.gov/pubmed/18427596>

Christensen, E. L., Skou, N., Dall, J., Woelders, K. W., Jorgensen, J. H., Granholm, J., & Madsen, S. N. (1998). EMISAR: an absolutely calibrated polarimetric L- and C-band SAR. *IEEE Transactions on Geoscience and Remote Sensing, 36*(6), 1852-1865. <https://doi.org/10.1109/36.729356>

Crowley, M. A., Cardille, J. A., White, J. C., & Wulder, M. A. (2019). Multi-sensor, multi-scale, Bayesian data synthesis for mapping within-year wildfire progression. *Remote Sensing Letters, 10*(3), 302-311.
<https://doi.org/10.1080/2150704X.2018.1536300>

Day, J. K., & Pérez, D. M. (2013). Reducing uncertainty and risk through forest management planning in British Columbia. *Forest Ecology and Management, 300*, 117-124. <https://doi.org/10.1016/J.FORECO.2012.11.035>

Delgado-Aguilar, M. J., Fassnacht, F. E., Peralvo, M., Gross, C. P., & Schmitt, C. B. (2017). Potential of TerraSAR-X and Sentinel 1 imagery to map deforested areas and derive degradation status in complex rain forests of Ecuador. *International Forestry Review, 19*(1), 102-118.
<https://doi.org/10.1505/146554817820888636>

Denis. (2013). Colormaputil. GitHubGist. Retrieved from
<https://gist.github.com/denis-bz/8052855>

Dostálová, A., Milenkovi, M., Hollaus, M., & Wagner, W. (2016). Influence of forest structure on the Sentinel-1 backscatter variation – analysis with full-waveform

lidar data (Vol. 2016, pp. 9–13).

Earthworm. (2018). Solution to cocoa-driven deforestation. Retrieved May 7, 2019, from <https://www.earthworm.org/pt/news-stories/solution-to-cocoa-driven-deforestation>

EnChroma Inc. (2018). EnChroma® Color Blind Test. Retrieved May 2, 2019, from <https://enchroma.com/pages/color-blindness-test>

Environment and Climate Change Canada. (2019a). Canadian Climate Normals 1981-2010 Station Data. Retrieved May 7, 2019, from http://climate.weather.gc.ca/climate_normals/results_1981_2010_e.html?stnID=650&autofwd=1

Environment and Climate Change Canada. (2019b). Daily Data Report for January 2017. Retrieved May 7, 2019, from http://climate.weather.gc.ca/climate_data/daily_data_e.html?StationID=650&Prov=BC&Year=2017&Month=1

European Space Agency. (n.d.-a). Sentinel-1 - Instrument Payload - Sentinel Online. Retrieved December 7, 2017, from <https://sentinel.esa.int/web/sentinel/missions/sentinel-1/instrument-payload>

European Space Agency. (n.d.-b). Sentinel-1 SAR User Guide. Retrieved January 8, 2019, from <https://sentinel.esa.int/web/sentinel/user-guides/sentinel-1-sar>

European Space Agency. (2013). *Sentinel-2 User Handbook, Issue 1 Revision 2*. Retrieved from https://sentinel.esa.int/documents/247904/685211/sentinel-2_user_handbook

European Space Agency. (2016). Sentinel-1 Observation Scenario. Retrieved February 2, 2017, from <https://sentinel.esa.int/web/sentinel/missions/sentinel-1/observation-scenario>

European Space Agency. (2018). ESA SNAP 6.0 built-in help [Computer Software].
Farr, T. G., Rosen, P. A., Caro, E., Crippen, R., Duren, R., Hensley, S., ... Alsdorf, D. (2007). The Shuttle Radar Topography Mission. *Reviews of Geophysics*, 45(2). <https://doi.org/10.1029/2005RG000183>

- Ferrero Corporate. (2017). Ferreros sixth palm oil progress report. Retrieved May 7, 2019, from <https://www.ferrero.com/group-news/Ferreros-sixth-palm-oil-progress-report?lang=EN>
- Gillies, S., & et al. (n.d.). Shapely: manipulation and analysis of geometric objects. [toblerity.org](https://github.com/Toblerity/Shapely). Retrieved from <https://github.com/Toblerity/Shapely>
- Gillies, S., & et al. (2013). Rasterio: geospatial raster I/O for {Python} programmers. Mapbox. Retrieved from <https://github.com/mapbox/rasterio>
- Google LLC. (2018). Sentinel-1 Algorithms—Google Earth Engine API. Retrieved October 17, 2018, from <https://developers.google.com/earth-engine/sentinel1>
- Gorelick, N., Hancher, M., Dixon, M., Ilyushchenko, S., Thau, D., & Moore, R. (2017). Google Earth Engine: Planetary-scale geospatial analysis for everyone. *Remote Sensing of Environment*. <https://doi.org/10.1016/j.rse.2017.06.031>
- Hansen, M. C., Potapov, P. V., Moore, R., Hancher, M., Turubanova, S. A., Tyukavina, A., ... Townshend, J. R. G. (2013). High-resolution global maps of 21st-century forest cover change. *Science*, 342(6160), 850–853. <https://doi.org/10.1126/science.1244693>
- Hirshorn, S. R. (2007). How to write a good requirement—checklist. In *NASA systems engineering handbook* (Rev2, pp. 197–200). Washington, DC: NASA Headquarters.
- Hunter, J. D. (2007). Matplotlib: a 2D graphics environment. *Computing in Science & Engineering*, 9, 90–95. <https://doi.org/10.1109/MCSE.2007.55>
- Klinka, K., Varga, P., Trethewey, C., Koot, C., Rau, M., Macku, J., & Kusbach, T. (2004). *Site units of the University of British Columbia Alex Fraser Research Forest*. Retrieved from http://afrf-forestry.sites.olt.ubc.ca/files/2018/11/SiteUnitsUBCAFRF_2018update_LowRes.pdf
- Kottek, M., Grieser, J., Beck, C., Rudolf, B., & Rubel, F. (2006). World Maps of Köppen-Geiger climate classification updated. *Meteorologische Zeitschrift*. <https://doi.org/10.1127/0941-2948/2006/0130>

Lillesand, T. M., & Kiefer, R. W. (2000). *Remote sensing and image interpretation* (fourth edi). John Wiley & Sons Inc.

Lynch, J., Maslin, M., Balzter, H., & Sweeting, M. (2013). Choose satellites to monitor deforestation. *Nature*, 496(7445), 293–294.
<https://doi.org/10.1038/496293a>

McKinney, W. (2010). Data structures for statistical computing in python. In *Proceedings of the 9th Python in Science Conference* (pp. 51–56).

Muro, J., Canty, M., Conradsen, K., Hüttich, C., Nielsen, A., Skriver, H., ... Menz, G. (2016). Short-term change detection in wetlands using Sentinel-1 time series. *Remote Sensing*, 8(10), 795. <https://doi.org/10.3390/rs8100795>

NASA's Earth Science Data and Information System. (n.d.). MODIS Collection 6 NRT Hotspot / Active Fire Detections MCD14DL.
<https://doi.org/10.5067/FIRMS/MODIS/MCD14DL.NRT.006>

Nestlé Global. (2018). Nestlé accellerates No Deforestation commitment by implementing 100% satellite monitoring coverage of its global palm oil supply chains. Retrieved May 7, 2019, from
<https://www.nestle.com/media/pressreleases/allpressreleases/no-deforestation-satellite-monitoring-coverage-palm-oil-supply-chains>

Nielsen, A. A., Conradsen, K., Skriver, H., & Canty, M. J. (2017). Visualization of and software for Omnibus test-based change detected in a time series of polarimetric SAR data. *Canadian Journal of Remote Sensing*, 43(6), 582–592.
<https://doi.org/10.1080/07038992.2017.1394182>

Oliphant, T. E. (2006). *A guide to NumPy*. USA: Trelgol Publishing.

Oliver, C., & Quegan, S. (1998). *Understanding synthetic aperture radar images. SciTech radar and defense series* (1st ed.). Scitech Publishing.

Ouchi, K., Ouchi, & Kazuo. (2013). Recent trend and advance of synthetic aperture radar with selected topics. *Remote Sensing*, 5(2), 716–807.
<https://doi.org/10.3390/rs5020716>

Pojar, J., Klinka, K., & Meidinger, D. V. (1987). Biogeoclimatic ecosystem

classification in British Columbia. *Forest Ecology and Management*, 22(1–2), 119–154. [https://doi.org/10.1016/0378-1127\(87\)90100-9](https://doi.org/10.1016/0378-1127(87)90100-9)

Potapov, P. V., Turubanova, S. A., Hansen, M. C., Adusei, B., Broich, M., Altstatt, A., ... Justice, C. O. (2012). Quantifying forest cover loss in Democratic Republic of the Congo, 2000–2010, with Landsat ETM+ data. *Remote Sensing of Environment*, 122, 106–116. <https://doi.org/10.1016/j.rse.2011.08.027>

Province of British Columbia. (n.d.). Wildfire Season Summary. Retrieved April 10, 2019, from <https://www2.gov.bc.ca/gov/content/safety/wildfire-status/about-bcws/wildfire-history/wildfire-season-summary>

Reiche, J., Bruin, S. De, Hoekman, D., Verbesselt, J., Herold, M., Reiche, J., ... Herold, M. (2015). A Bayesian approach to combine Landsat and ALOS PALSAR time series for near real-time deforestation detection. *Remote Sensing 2015, Vol. 7, Pages 4973-4996*, 7(5), 4973–4996.
<https://doi.org/10.3390/RS70504973>

Reiche, J., Lucas, R., Mitchell, A. L., Verbesselt, J., Hoekman, D. H., Haarpaintner, J., ... Herold, M. (2016). Combining satellite data for better tropical forest monitoring. *Nature Climate Change*, 6(2), 120–122.
<https://doi.org/10.1038/nclimate2919>

Reiche, J., Verbesselt, J., Hoekman, D., & Herold, M. (2015). Fusing Landsat and SAR time series to detect deforestation in the tropics. *Remote Sensing of Environment*, 156, 276–293. <https://doi.org/10.1016/j.rse.2014.10.001>

Reiche, J., Verhoeven, R., Verbesselt, J., Hamunyela, E., Wielaard, N., & Herold, M. (2018). Characterizing tropical forest cover loss using dense Sentinel-1 data and active fire alerts. *Remote Sensing*. <https://doi.org/10.3390/rs10050777>

Sannier, C., McRoberts, R. E., Fichet, L. V., & Makaga, E. M. K. (2014). Using the regression estimator with landsat data to estimate proportion forest cover and net proportion deforestation in gabon. *Remote Sensing of Environment*, 151, 138–148. <https://doi.org/10.1016/j.rse.2013.09.015>

Satellite Imaging Corporation. (n.d.-a). SPOT-6 Satellite Sensor. Retrieved May 12,

- 2019, from <https://www.satimagingcorp.com/satellite-sensors/spot-6/>
- Satellite Imaging Corporation. (n.d.-b). SPOT-7 Satellite Sensor. Retrieved May 12, 2019, from <https://www.satimagingcorp.com/satellite-sensors/spot-7/>
- Shawn Riley, Stephen D. DeGloria, & Robert Elliot. (1999). A terrain ruggedness index that quantifies topographic heterogeneity. *Intermountain Journal of Sciences*. <https://doi.org/citeulike-article-id:8858430>
- Soverel, N. O., Perrakis, D. D. B., & Coops, N. C. (2010). Estimating burn severity from Landsat dNBR and RdNBR indices across western Canada. *Remote Sensing of Environment*, 114(9), 1896–1909.
<https://doi.org/10.1016/J.RSE.2010.03.013>
- Suneela Mishra, J. V. D., & Misra, T. (2016). Thermal noise removal in hybrid polarimetry SAR data. In X. J. Xiong, S. A. Kuriakose, & T. Kimura (Eds.) (Vol. 9881, p. 98811P). International Society for Optics and Photonics.
<https://doi.org/10.1117/12.2223309>
- Torres, R., Snoeij, P., Geudtner, D., Bibby, D., Davidson, M., Attema, E., ... Rostan, F. (2012). GMES Sentinel-1 mission. *Remote Sensing of Environment*, 120, 9–24.
<https://doi.org/10.1016/J.RSE.2011.05.028>
- Ucar, Z., Bettinger, P., Weaver, S., Merry, K. L., & Faw, K. (2014). Dynamic accuracy of recreation-grade GPS receivers in oak-hickory forests. *Forestry: An International Journal of Forest Research*, 87(4), 504–511.
<https://doi.org/10.1093/forestry/cpu019>
- van den Bossche, J., & et al. (2017). Geopandas: Python tools for geographic data. Retrieved from <https://github.com/geopandas/geopandas>
- Verbesselt, J., Zeileis, A., & Herold, M. (2012). Near real-time disturbance detection using satellite image time series. *Remote Sensing of Environment*, 123, 98–108.
<https://doi.org/10.1016/j.rse.2012.02.022>

Appendices

Appendix A Literature table

This appendix includes a selection of background literature for this thesis.

Title	Citation	Why is this interesting?	Technology	Data source
Combining satellite data for better tropical forest monitoring	Reiche et al., 2016	journal commentary about state of the art of tropical forest change detection	SAR & multispectral	ALOS-2, PALSAR-2, Sentinel-1; Landsat 8, Sentinel 2
Influence of forest structure on the Sentinel-1 backscatter variation - analysis with full-waveform lidar data	Dostálková, Milenkovi, Hollaus, & Wagner, 2016	combining SAR with LiDAR	C SAR (VV, VH) calibrated with ALS	Sentinel-1 time series; ALS: LMS-Q560, LMS-Q680
Fusing Landsat and SAR time series to detect deforestation in the tropics	Reiche, Verbesselt, Hoekman, & Herold, 2015	fusion for deforestation monitoring in tropics	multispectral & L-band SAR	Landsat NDVI; ALOS PALSAR
High-Resolution Global Maps of 21st-Century Forest Cover Change	Hansen et al., 2013	using Google Earth Engine for large-scale server-based data processing	multispectral	Landsat

Study area	Research question	Conclusion	Research gaps
tropical global	not applicable	Imagery need to be freely available and easy to access. Optical and SAR groups should work together more or be merged. Shift from downloading of data for local storage and processing to centralized storage and remote processing.	Utilize Sentinel-1 for change detection.
temperate lake Neusiedl, Austria	study of seasonal variability of C-band SAR backscatter	Differences in seasonality between deciduous and coniferous forests. Forest height has little influence. 5-year gap between ALS & SAR may have influenced results	test the validity of results in different climatic conditions such as Sweden and Finland
tropical Fiji	1. How do Landsat NDVI and SAR correlate? 2. How does fusion improve accuracy? 3. How do degrading factors influence analysis?	better forest monitoring with fusion and time series	use algorithm for different data sources. near-real-time fusion.
global	Create global maps of forest cover extent and change	Forest cover dynamics maps created at 30-metre resolution from 2000 to 2012 Globally, 2.3 million km ² of forest cover gain and 0.8 million km ² of loss. The forest loss rate in the tropics increased.	None mentioned

Title	Citation	Why is this interesting?	Technology	Data source
Recent trend and advance of synthetic aperture radar with selected topics	Ouchi, Ouchi, & Kazuo, 2013	review journal article that gives an overview of the state of the art in SAR	SAR	not applicable
Systems and Methods for Enhancing Synthetic Aperture Radar Imagery	WO 2016/2054 06 A1, 2016	patent describing the OptiSar algorithm	multispectral & SAR fusion	any
Near real-time disturbance detection using satellite image time series	Verbesselt et al., 2012	Explains the BFAST monitor algorithm for time series analysis.	multispectral imaging, time series analysis	simulated NDVI time series, 16-day MODIS NDVI composites
A Bayesian Approach to Combine Landsat and ALOS PALSAR Time Series for Near Real-Time Deforestation Detection	Reiche et al., 2015	Similar research question and approach to my own.	multispectral & L-band SAR fusion	Landsat, ALOS PALSAR

Study area	Research question	Conclusion	Research gaps
not applicable	not applicable	Amplitude: many applications including oceanic internal waves. InSAR: New, higher resolution DEM is being created with TerraSAR-X and TanDEM-X data. PolInSAR: enables the characterization of scattering mechanisms.	developing and validating new SAR technologies; applications for geoscience.
any	not applicable	not applicable	not applicable
tropical Somalia	1. Can a period of normal (stable) data be identified in a time series? 2. Can this model be used to differentiate between normal and abnormal changes?	BFAST... 1. ... runs fast. 2 ... needs no pre-defined thresholds. 3. ... can analyze time series with data gaps. 4. ... analyzes the full temporal detail of a time series.	apply BFAST to ESA Sentinel data
subtropical Fiji	detecting logging in near real-time	Fusion was spatially and temporally more accurate than NDVI or HVHH alone. Better overall accuracy with MulTiFuse than this study but MulTiFuse uses future data. Bayesian approach best for near real-time disturbance detection.	application in more complex forests with more complicated harvesting practices

Title	Citation	Why is this interesting?	Technology	Data source
Sustainability: Choose satellites to monitor deforestation	Lynch et al., 2013	Journal commentary on what's needed for monitoring logging in near real-time	SAR	not applicable
An advanced system for the automatic classification of multitemporal SAR images	Bruzzone et al., 2004	feature extraction and neural networks to interpret multitemporal SAR image stack	C-band SAR. Feature extraction. Neural network (radial basis functions)	ERS-1
Characterizing Tropical Forest Cover Loss Using Dense Sentinel-1 Data and Active Fire Alerts	Reiche et al., 2018	Sentinel-1 time series analysis in the tropics. Similar to my research question.	multispectral & C-band SAR. Bayesian modelling	Sentinel-1
Short-Term Change Detection in Wetlands Using Sentinel-1 Time Series	Muro et al., 2016	Sentinel-1 near real-time change detection. Crucial technology for my research question.	C-band SAR (VV, VH) S1-omnibus time series algorithm	Sentinel-1

Study area	Research question	Conclusion	Research gaps
tropical global	detecting logging in near real-time	The international community should commit to funding and operating a constellation of 5 tropical-orbiting SAR satellites to monitor logging.	1. There is a need for a tropical orbiting SAR mission. 2. Need a plan to monitor carbon stocks several times a year.
temperate Switzerland	land cover classification	“Features of temporal variability of backscattering and long-term coherence are very effective in modelling [...]” RBF neural networks are a very effective classification methodology.	None mentioned.
tropical Riau, Indonesia	temporally relating forest cover loss to fire alerts	“confident, timely, and gap-free forest-cover-loss detection” Most forest cover loss pre-dated or post-dated fires.	fully integrated near real-time system based on active fire alerts and Sentinel-1 data
temperate wetlands Spain & France	detect short-term changes in wetlands	S1-omnibus could capture land-cover-land-use changes accurately in space and time. Achieved 6-day cadence at 30-metre spatial resolution	Figure out whether this approach works with single-pol data.

Title	Citation	Why is this interesting?	Technology	Data source
Collect Earth: Land Use and Land Cover Assessment through Augmented Visual Interpretation	Bey et al., 2016	Example of how to write a paper about a computer application	Google Earth Engine, Bing maps	various
Visualization of and Software for Omnibus TestBased Change Detected in a Time Series of Polarimetric SAR Data	Nielsen, Conradsen, Skriver, & Cantz, 2017	pixel-based time-of-change detection	C-band & L-band SAR (VV, HH, VH, HV)	EMISAR, RADARSAT-2
Multi-sensor, multi-scale, Bayesian data synthesis for mapping within-year wildfire progression	Crowley, Cardille, White, & Wulder, 2019	fusion of multispectral imagery from different sensors with a Bayesian method for wildfire monitoring	multispectral; multi-sensor-fusion	Landsat-8, Sentinel-2, MODIS
Potential of TerraSAR-X and Sentinel 1 Imagery to Map Deforested Areas and Derive Degradation Status in Complex Rain Forests of Ecuador	Delgado-Aguilar, Fassnacht, Peralvo, Gross, & Schmitt, 2017	state of the art in disturbance detection	X- and C-band SAR	SPOT, Sentinel-1, TerraSAR-X

Study area	Research question	Conclusion	Research gaps
tropical Papua New Guinea	Speeding up manual interpretation of land use and land cover change	With this tool, anyone can do a robust land use and land cover classification.	None mentioned.
multiple	Create time-of-change images	First change, most recent change and change frequency maps produced. The software is useful for processing time series of polarimetric images.	None mentioned.
temperate British Columbia, Canada	monitor wildfire progression in near real-time	The authors achieved a highly automated approach for wildfire monitoring	reconstruct the entire British Columbia fire season of 2017 with this algorithm
tropical Ecuador	1. Define thresholds to define degraded forest. 2. Compare results from multiple sensors. 3. Map degraded forest by combining maps with field-derived thresholds	SPOT great but expensive and clouds are an issue. Information from SAR is limited. Can be improved by interferometry, polarimetry or using dense time series. Sentinel-1 is free and hence good where topography is less pronounced.	Integrate this approach in an operational forest monitoring system

Appendix B **Image interpreter's instructions**

Preface

Many thanks for your help!

If you have any questions about the below instructions, don't hesitate to come to my desk, e-mail me at xxxxxxxxxx@xxxxxx.xxx or call me at #####. From August 7-14 only e-mail works.

Background

We are trying to answer the research question:

How quickly and accurately can we detect the location of new linear features from Sentinel-1 SAR image time series compared to before-and-after comparison of optical images?

As a case study we are looking at the fireguards that fire fighters created at Alex Fraser Research Forest (Williams Lake, BC) during the wildfires in July, August and September 2017.

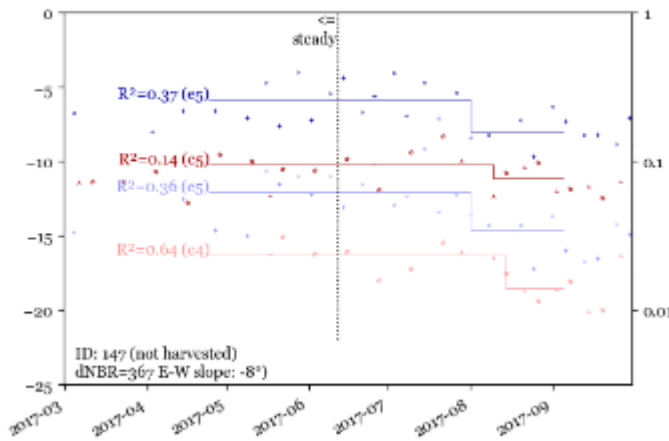
For 11 consecutive Mondays during and after the fire period, Earth Engine will create SAR summary images that summarize the information of a time series of images in one image. I'll ask you to find the fire guards in them. Then I'll compare with GPS ground truth how well y'all found the fire guards. That way we compare three types of data one can look at to detect forest change: the SAR time series trend composite, the SAR time series step composite (both explained in the next section), and Sentinel-2 multispectral images.

The composite images

I created two types of change composites, one based on fitting a linear trend to the time series at each pixel, and one based on fitting a single-step function to the time series. I computed the least squares fit for these functions, i.e. the function that would minimize the sum of the squared deviations of the data from the function. The linear fit is a weighted fit, with recent observations weighted more heavily than older ones.

The trend composite image consists of two bands. I assigned 'red' to the value of the trend line at the start of the observation period, and 'green' to the trend line value at the end of the observation period.

In the step composite, ‘red’ and ‘green’ correspond to the average backscatter values before and after the detected drop, i.e. the left and right values of the step function. In addition, I have assigned the ‘blue’ band to the R^2 value of the fit, which is a measure for how well a step model explains the variation in the data compared to the steady case. Here’s an example of fitting the single-step function to a time series at one pixel:



Note that the resulting composites often have funny edges. This is for a number of reasons:
1. Many image scene boundaries cross the study area. Hence, the number of values from which the step and trend fits are computed, vary. If they are computed from just 3 or 4 values, for instance, that part of the image will look grainy.
2. There are sometimes wrong values at the scene boundaries. I’ve tried my best to remove them but a few remain.
3. We use west-looking (descending) satellite images for west-facing terrain and east-looking (‘ascending’) satellite images for easterly aspects because SAR images provide little information about terrain facing the satellite. For this, all terrain was divided into east or west, even when facing almost exactly north or when almost flat. For these reasons, the image will show distinct regions with a slightly different colour mix.

I’m not going into what features look like on a SAR image. You’ll get a feel for it yourself. Just keep three things in mind. a) High backscatter represents high land cover roughness on the centimeter scale (like a canopy) while smooth land cover appears dark (like lakes). b) SAR is side-looking with incidence angles ranging from 18.3 to 46.8 degrees measured from vertical. Therefore a 3-D feature like a fireguard can appear quite complex in the image depending on the illumination direction. c) In the composites the red channel represents the landscape before the fire and the green channel represents the landscape after the fire.

Preparation

1. Open **Chrome**.
2. Go to <https://code.earthengine.google.com>
3. Login with xxxxxxxxxxxx@xxxxxx.xxx and password: xxxxxxxxxxx

4. On the *Scripts* tab on the left, find the group *users/lschreiber/delineate* (This can take several seconds.)
5. Hover over one of the scripts named I#, click the pencil, and rename it to your name.

The screenshot shows the Google Earth Engine interface with the 'Scripts' tab selected. On the left, there's a tree view of scripts under 'users/lschreiber'. A script named 'Lukas' is selected and highlighted with a blue border. On the right, the code for 'Lukas' is displayed in a code editor window. The code includes several comments starting with '===== // bringing it =====' and a function definition 'function main_:'.

```

    78     });
    79 }
    80
    81
    82 // =====
    83 // bringing it
    84 // =====
    85
    86 function main_:
    87
  
```

6. Double-click the script. The source code will appear in the top middle of your window. (This can take several seconds.)
7. E-mail me a short description of your experience with manual image interpretation and SAR image interpretation (if any) to lschreiber@urthecast.com. In addition, include line 5 of the source code. Use the subject line "image interpretation experience". I will summarize what experience you listed in the journal article. Make this short, since I will condense it to about half a sentence.

Delineating

As you delineate the lines, please use the following Google doc to log anything interesting or worrying you notice, what's on your mind, and to log your progress every time you work on this.

<https://docs.google.com/document/d/1KNYHBdZ1L41KqTYuFObY39OJ2jLxyPj5zKRGoDG-uZw/edit?usp=sharing>

You can also find this document by navigating to drive.google.com while logged in with my e-mail.

Repeat the steps below for the following dates, in that order:

- 2017-07-10
- 2017-07-17
- 2017-07-24
- 2017-07-31
- 2017-08-07
- 2017-08-14
- 2017-08-21
- 2017-08-28

- 2017-09-04
- 2017-09-11
- 2017-09-18

One of you is assigned the multispectral images. There are fewer of them than one image a week. If you see the same one again, make a note of it in the Google Doc and move on.

Don't go "back in time" to a previous date and make changes to your delineation for that date. You can go back to take a look though.

1. Set a timer to record how long you take for each of the eleven dates above. This doesn't need to be very accurate. Just make sure not to count your lunch break ;)
2. Change the date in line 6 to one of the dates above (start with the first).
3. On the top left of the code window, press *Save* and *Run*.



4. Pull up the code window by dragging the separation line until only the blue bar is left.

There's usually no need to zoom the map (except possibly to zoom out 1 level at the start to make things easier. You do need to pan though.

To restore the original zoom level, press the *back to center* button in the bottom left.

There are 4 layers on the map, extending over a rectangular study area:

- In the background, a multispectral image from June 25 (before the fire). You can use this to get an idea of what the landscape looked like before the fire.
- A SAR step composite (predominantly green) and a SAR trend composite (pixely red-green), covering different areas of the screen. You will use these to delineate changes. If you're I5, you get a multispectral image instead of these two.
- Overlaid in black, a map of all roads known to exist in the area until June 2017.

On the top right of the map window, you can hover over *Layers*. Then you can use the sliders on the right to hide the top layers and see what's underneath. **Leave the checkmarks alone!**

The layers will take a while to load.

5. Pan around the entire study area (Wait for the imagery to load. The area is roughly double the size of a screen.) and identify new linear features (such as trails, fireguards and roads). There are some artefacts from the scene boundaries. Don't delineate these.
To figure out what is new:

To understand, look at the old roads shown in black. They are darker than the rest of the landscape. For new roads, only the green channel will be darker.

Anything that you've delineated before, is not new.

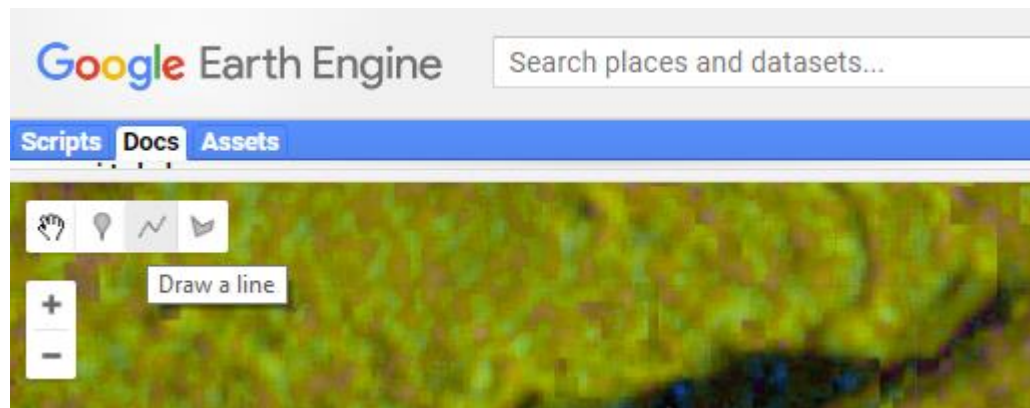
- a) On the trend composite new stuff will be a strong red, sometimes accompanied by

- a strong green edge (depending on the orientation of the linear feature with respect to the satellite).
- b) On the step composite new linear features are purple (a mix of red for backscatter drop, and blue for a high R^2), again sometimes accompanied by a cyan edge (green for backscatter increase, and blue for high R^2).
- c) On the multispectral image, compare to the one from June 25 to find new linear features.

To figure out if a feature is linear: If it's more than about five times longer than wide, we call it linear. It can be straight or winding.

Hint: There will be images that don't expose any new linear features. Don't worry about this but make a note in the Google Doc.

6. Use the geometry tools in the top left to delineate all new linear features:
 - a. *[Skip this step the very first time]* Hover over the *Geometry Imports* in the top left and press *+ new layer*.
 - b. Click on the line tool.



- c. Set the first point at the start of the linear feature.

Do not stop delineating or press Esc when you have only one point. Earth Engine gets very confused about lines that contain only one point. And they become invisible. This will create extra work for me later.

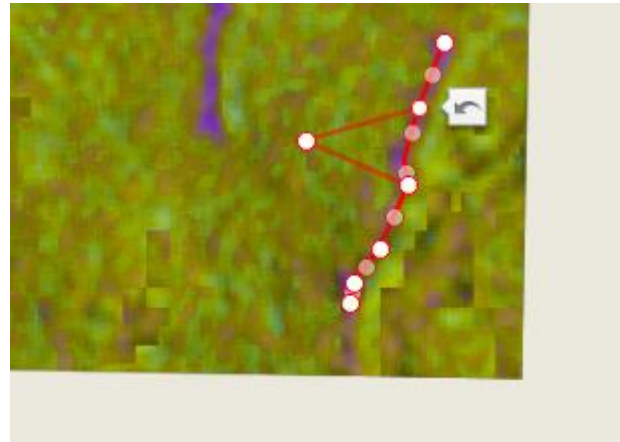
- d. Keep adding points, following the center of the linear feature.



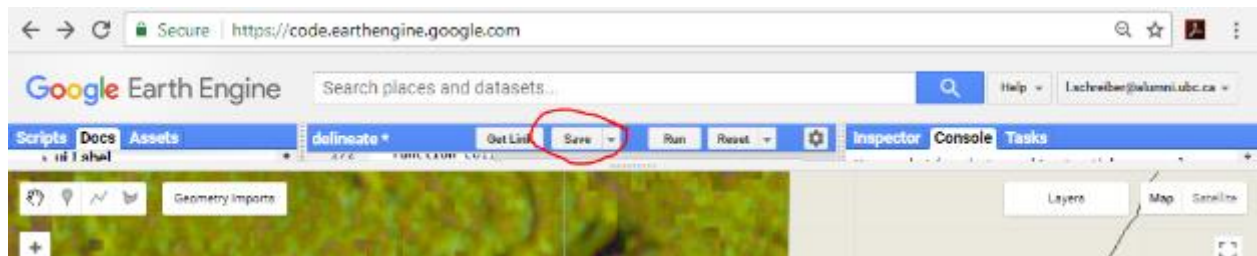
- e. When you are done with one line, press Esc.

- f. Now and at any time later, you can adjust any line by clicking on it and pulling the vertices.

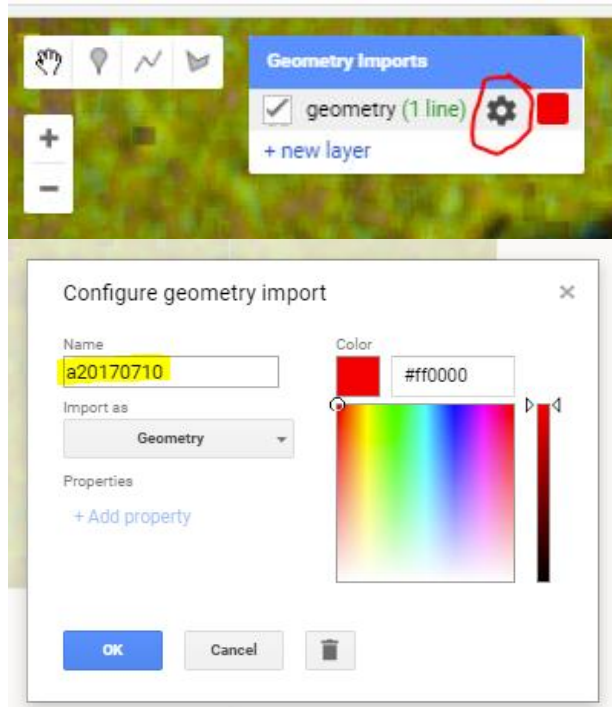
However, do not change lines marked with a different date than the ‘current’ date. If you think you’ve made a mistake, make a note in the Google Doc.



- g. Press *Save* in the middle of the blue bar. If you can’t see the blue bar, pull down the separation.



- h. Hover over the *Geometry Imports* in the top left, hover over the last list item (*geometry#*), click the gear and change its name to the date in line 6 of the code panel in the format yyyy-mm-dd preceded by an ‘a’.



- i. Repeat steps b-g until you have delineated all new linear features across the study area.
 7. Check your timer and record in a spreadsheet how long you took.
- Repeat steps 1-7 for the other dates mentioned at the start of this section.

Tips

How your work is saved

By pressing *Save* all changes to the script (should be only line 6) and the delineated fireguards will be saved to Git. You can restore an earlier version by clicking on *Revision history* next to the script but you should not ever need to do that. Whenever you close the browser tab or script and open it again (by double-clicking the script), it should be back to the state it was in when you last pressed *Save*. I. e. you can lose one line at most if you follow the instructions.

Appendix C **Image interpreter's logs**

I asked the image interpreters to log their work.

Bob's log

Experience e-mail:

"I have basic manual image interpretation experience, specifically of aerial imagery (from FRST 443 course & working on a photogrammetric project in the lab), and no SAR image interpretation experience."

2018-08-01:

- Interpretation of 2017-07-10
 - Wasn't sure when the images loaded because I didn't realize it would be so small & where to look on the world map
 - Delineated roads that appear in the Sentinel-2 2017-06-25 layer but are not the pre-existing roads layer (couldn't explicitly find if I was supposed to do that in the instructions)
 - Deleted these later
 - Total time for 2017-07-10 = 1hr 3min
- Interpretation of 2017-07-14
 - Delineated roads that appear in the Sentinel-2 2017-06-25 layer but are not the pre-existing roads layer (couldn't explicitly find if I was supposed to do that in the instructions)
 - Deleted these later
 - Total time for 2017-07-14 = 11 min
- Interpretation of 2017-07-24
 - Total time for 2017-07-24 = 13 min
- Interpretation of 2017-07-31
 - Total time for 2017-07-31 = 14 min
- Interpretation of 2017-08-07
 - Total time for 2017-08-07 = 53 min
- Interpretation of 2017-08-14

- Total time for 2017-08-14 = 59 min
- Interpretation of 2017-08-21
 - Total time for 2017-08-21 = 19 min
- Interpretation of 2017-08-28
 - Total time for 2017-08-28 = 23 min
- Interpretation of 2017-09-04
 - Total time for 2017-09-04 = 14 min

2018-08-01:

- Lost several geometry imports (a20170817, a20170821, a20170828, a20170904). Only geometry imports saved include:
 - a20170710
 - a20170714
 - a20170724
 - a20170731
 - a20170807
 - Geometry (unnamed)
- Interpretation of 2017-08-14
 - Total time for 2017-08-14 = 11 min
- Interpretation of 2017-08-21
 - Total time for 2017-08-21 = 15 min
- Interpretation of 2017-08-28
 - Total time for 2017-08-28 = 11 min
- Interpretation of 2017-09-04
 - Total time for 2017-09-04 = 11 min
- Interpretation of 2017-09-11
 - Total time for 2017-09-11 = 16 min
- Interpretation of 2017-09-18
 - Total time for 2017-09-18 = 12 min
- Finished all interpretations: 5 hours 45 minutes

Alice's log

No experience e-mail received.

- Interpretation of 2017-07-10
 - Total time = 14 min No linear features found
- Interpretation of 2017-07-17
 - Total time for 2017-07-17 = 16 min
- Interpretation of 2017-07-24
 - Total time for 2017-07-17 = 17 min
- Interpretation of 2017-07-31
 - Total time for 2017-07-17 = 9 min
- Interpretation of 2017-08-07
 - Total time for 2017-07-17 = 17 min
- Interpretation of 2017-08-14
 - Total time for 2017-07-17 = 12 min
- Interpretation of 2017-08-21
 - Total time for 2017-07-17 = 21 min
- Interpretation of 2017-08-28
 - Total time for 2017-07-17 = 18 min
- Interpretation of 2017-09-04
 - Total time for 2017-07-17 = 12 min
- Interpretation of 2017-09-11
 - Total time for 2017-07-17 = min
- Interpretation of 2017-09-18
 - Total time for 2017-09-18 = min

Overall comments: the delineation process is a bit subjective. The process itself does not take too much time, but waiting for images fully loaded takes some time.

Carol's log

No experience e-mail received.

- Interpretation of 2017-07-10
 - Total time = 19 min

- Notes: eastern boundary is very pixelated
- Interpretation of 2017-07-14
 - Total time = 14 min
 - Notes: eastern boundary is very pixelated
- Interpretation of 2017-07-24
 - Total time = 11 min
 - Notes: difficult to differentiate old roads from new
- Interpretation of 2017-07-31
 - Total time = 9 min
 - Notes: found potential large fire guards
- Interpretation of 2017-08-07
 - Total time = 6 min
 - Notes: less new roads
- Interpretation of 2017-08-14
 - Total time = 8 min
- Interpretation of 2017-08-21
 - Total time = 8 min
- Interpretation of 2017-08-28
 - Total time = 7 min
 - Notes: large number of roads/fire guards showed up, especially in the trend composite scene
- Interpretation of 2017-09-04
 - Total time = 4 min
- Interpretation of 2018-09-11
 - Total time = 4 min
- Interpretation of 2018-09-18
 - Total time = 2 min

Final time for the interpretation of 11 scenes: 92 min / 1hr 32min

Final notes: It was challenging to remember which roads/fire guards had already been delineated in the past. Because of this, several roads were likely delineated over and over again.

Dan's log

Experience e-mail:

“I left pretty lengthy comments in the Google Doc so I will keep this short.

We needed more information about previously established linear features on the landscape (both natural and man-made) to do this delineation as accurately as possible. Second, I found the step composite easier to work with than the trend composite.”

- Interpretation of 2017-07-10
 - Total time = 35 min
- Interpretation of 2017-07-17
 - Total time = 10 min
- Interpretation of 2017-07-24
 - Total time = 19 min
- Interpretation of 2017-07-31
 - Total time = 36 min
- Interpretation of 2017-08-07
 - Total time = 30 min
- Interpretation of 2017-08-14
 - Total time = 15 min
- Interpretation of 2017-08-21
 - Total time = 18 minutes
- Interpretation of 2017-08-28
 - Total time = 20 min
- Interpretation of 2017-09-04
 - Total time = 10 min
- Interpretation of 2018-09-11
 - Total time = 23 minutes
- Interpretation of 2018-09-18

- Total time = 11 minutes

Notes: First off, the description of what “change” will look like in each of the SAR images was helpful, but seeing an example of what that would look like for both the step and trend composites would have been even more helpful. It was not until I saw dramatic changes in the imagery was I confident in the work I was doing. Second, I feel as though just using the “known roads” layer and the Sentinel images was completely inadequate for ensuring that we were not delineating old features. There were numerous linear features which repeatedly showed up as “change” but in-fact were not fire guards or new roads. Having features such as utilities ROW, linear wetland features, as well as including as many old logging ‘skid trails’ as possible would be very important to ensure that the images were not “over-delineated”. Additionally, it became apparent that the edges of harvest units also appear as “change” in the images -- so, including recent harvest units would also have been useful. There were also numerous errors in the images that looked similar to the linear features that we were supposed to be identifying. Also, Google Earth Engine was painfully slow. If the project was hosted on a local Geodatabase I could have completed the task in probably $\frac{1}{5}$ of the time.

On a side note, I found the step composite image far easier to use for this task than the trend composite.

Erin’s log

No experience e-mail received.

- Interpretation of 2017-07-10
 - Total time = 5 min
- Interpretation of 2017-07-17
 - Total time = 1 min
 - Notes - same image as prior
- Interpretation of 2017-07-24
 - Total time = 1 min
 - Notes - same image as prior

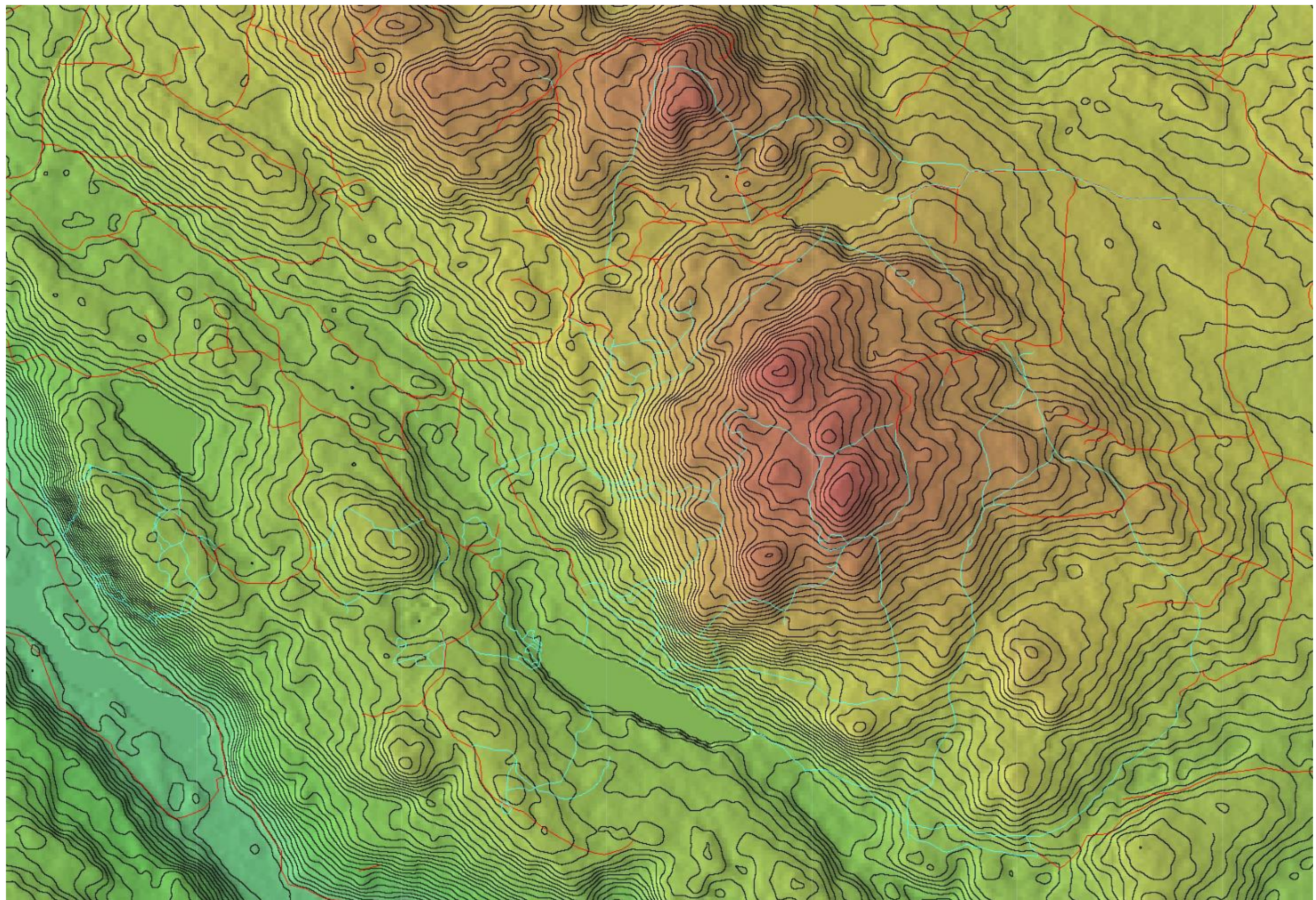
- Interpretation of 2017-07-31
 - Total time = 20 min
 - Notes: some areas obscured by clouds and shadows
- Interpretation of 2017-08-07
 - Total time = 3 min
 - Notes: 2 new line segments were added that were probably there in 7/31, but not visible due to clouds and shadows
- Interpretation of 2017-08-14
 - Total time = 1 min
 - Notes: no new lines
- Interpretation of 2017-08-21
 - Total time = 7 minutes
 - Notes: entire image extremely smokey, lots of new guards visible though, middles of some guards not visible
- Interpretation of 2017-08-28
 - Total time = 1 min
 - Notes: same image as 8/21
- Interpretation of 2017-09-04
 - Total time = 1 min
 - Notes: same image as 8/21
- Interpretation of 2018-09-11
 - Total time = 7 minutes
 - Notes: Still very smokey
- Interpretation of 2018-09-18
 - Total time = 6 minutes
 - Notes: Smoke cleared, much clearer image

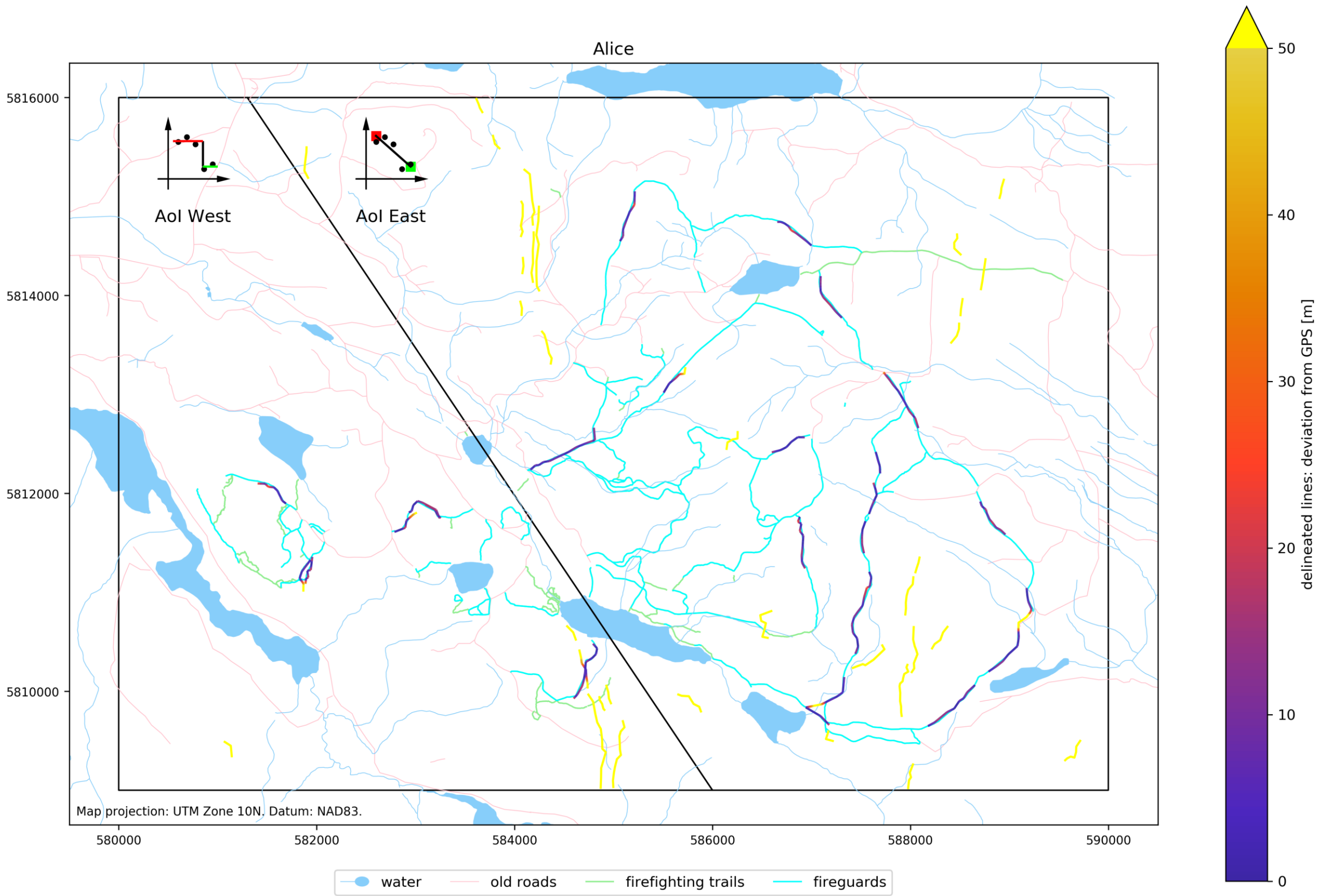
Appendix D **Image interpreter's maps**

1. *A Sentinel-2 image from September 13 to show the burned areas and fireguards. Overlaid are the pre-existing roads in black.....p. 121*
2. *A contour map as reference of the terrain. The distance between the contours is 10 vertical metres. The map also shows pre-existing roads in red and fireline locations in cyan.....p. 122*
- 3.-7. *The interpreters' maps.pp. 123–127*



Sentinel-2 scene from 2017-09-13



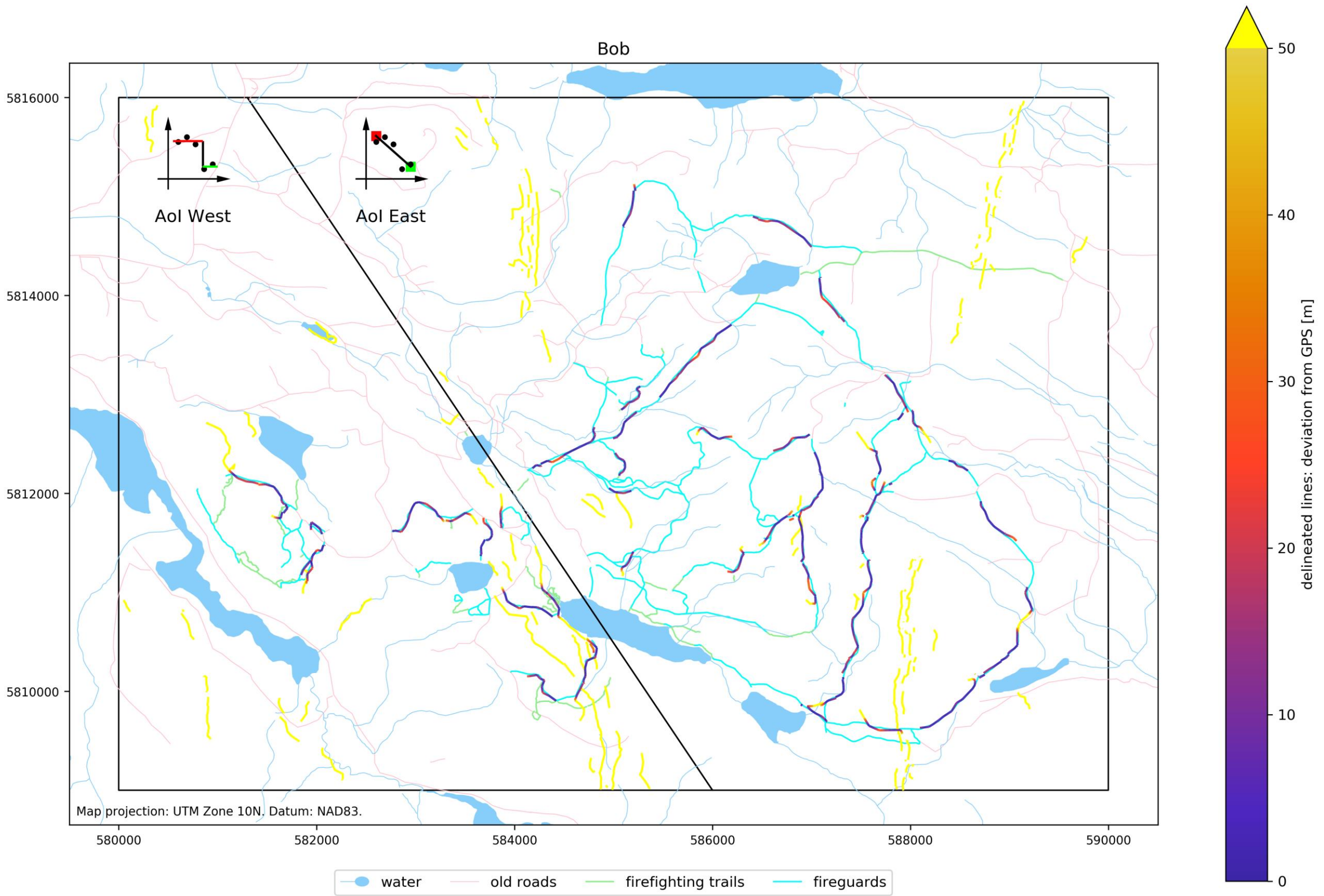


step image:

Out of 5.6 km of delineated features, 2.9 km were firelines. That is 51.1%
Out of 10.6 km of fireguards, 2.6 km were detected. That is 24.2%
10.7 m average deviation from GPS derived location

trend image:

Out of 18.3 km of delineated features, 8.8 km were firelines. That is 47.8%
Out of 42.2 km of fireguards, 10.0 km were detected. That is 23.6%
8.4 m average deviation from GPS derived location

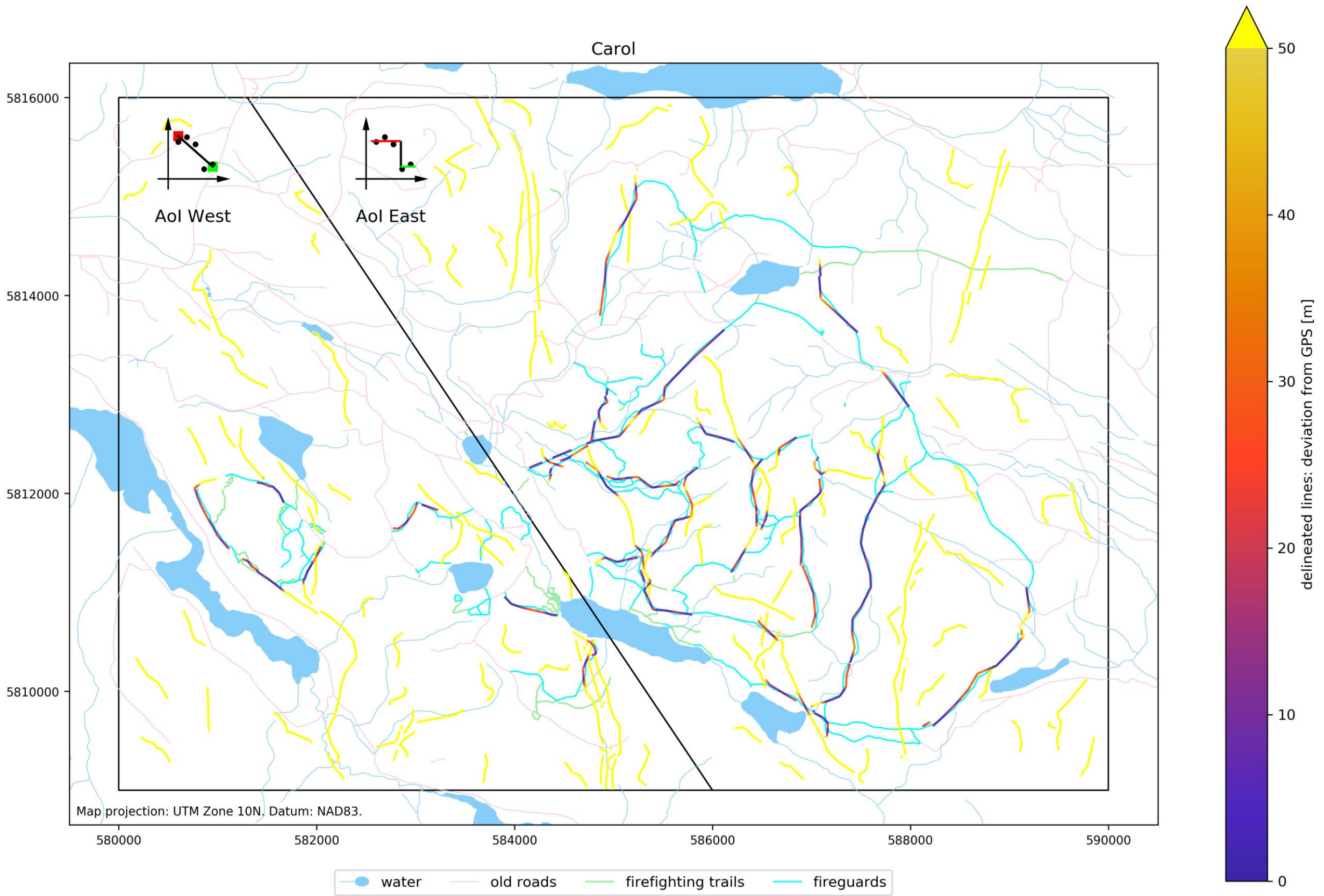


step image:

Out of 18.8 km of delineated features, 6.1 km were firelines. That is 32.5%
Out of 10.6 km of fireguards, 5.8 km were detected. That is 55.2%
11.5 m average deviation from GPS derived location

trend image:

Out of 31.7 km of delineated features, 15.9 km were firelines. That is 50.1%
Out of 42.2 km of fireguards, 17.2 km were detected. That is 40.8%
10.5 m average deviation from GPS derived location

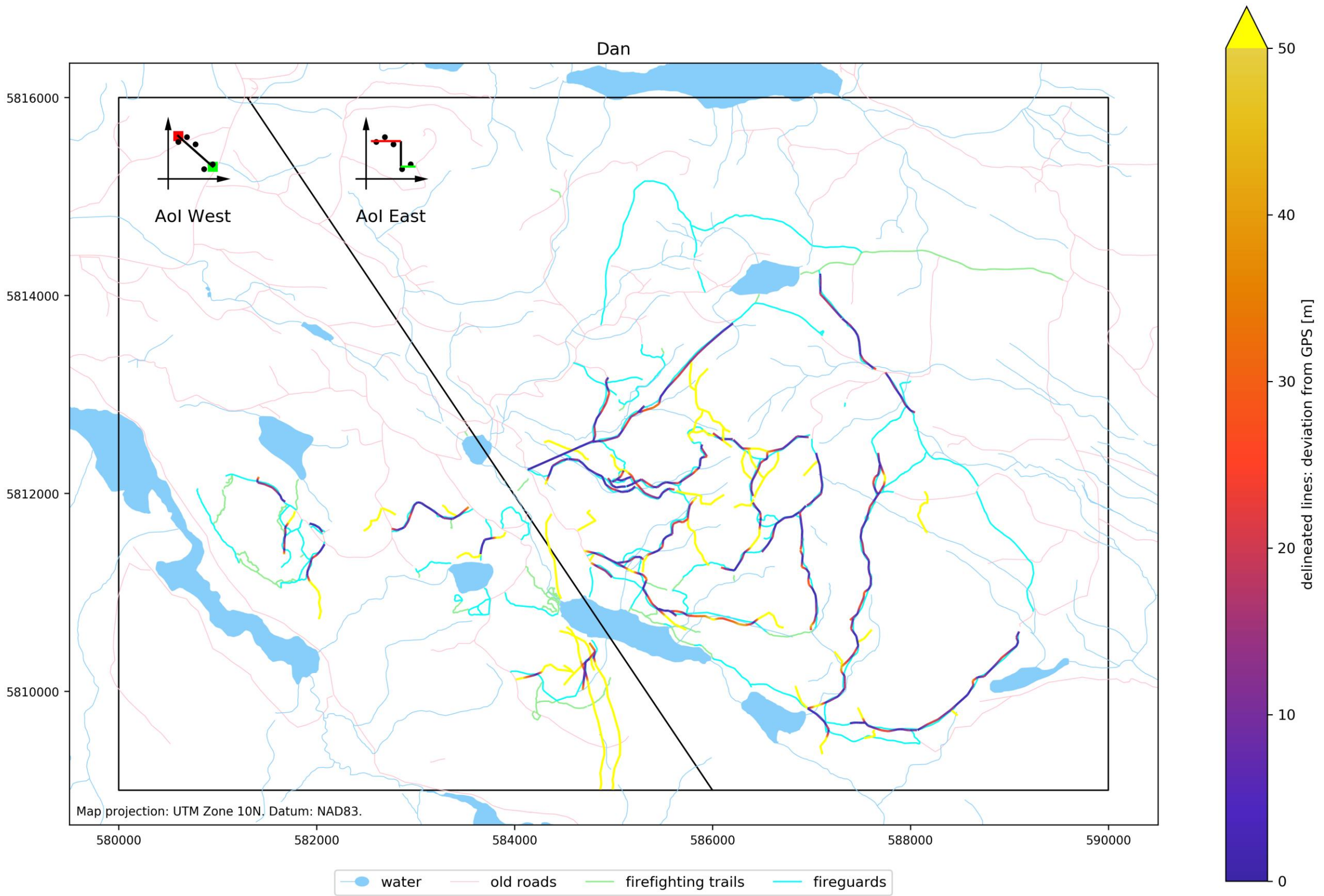


trend image:

Out of 29.6 km of delineated features, 3.9 km were firelines. That is 13.1%
 Out of 10.6 km of fireguards, 4.3 km were detected. That is 40.6%
 15.3 m average deviation from GPS derived location

step image:

Out of 62.0 km of delineated features, 20.0 km were firelines. That is 32.3%
 Out of 42.2 km of fireguards, 20.8 km were detected. That is 49.3%
 16.2 m average deviation from GPS derived location

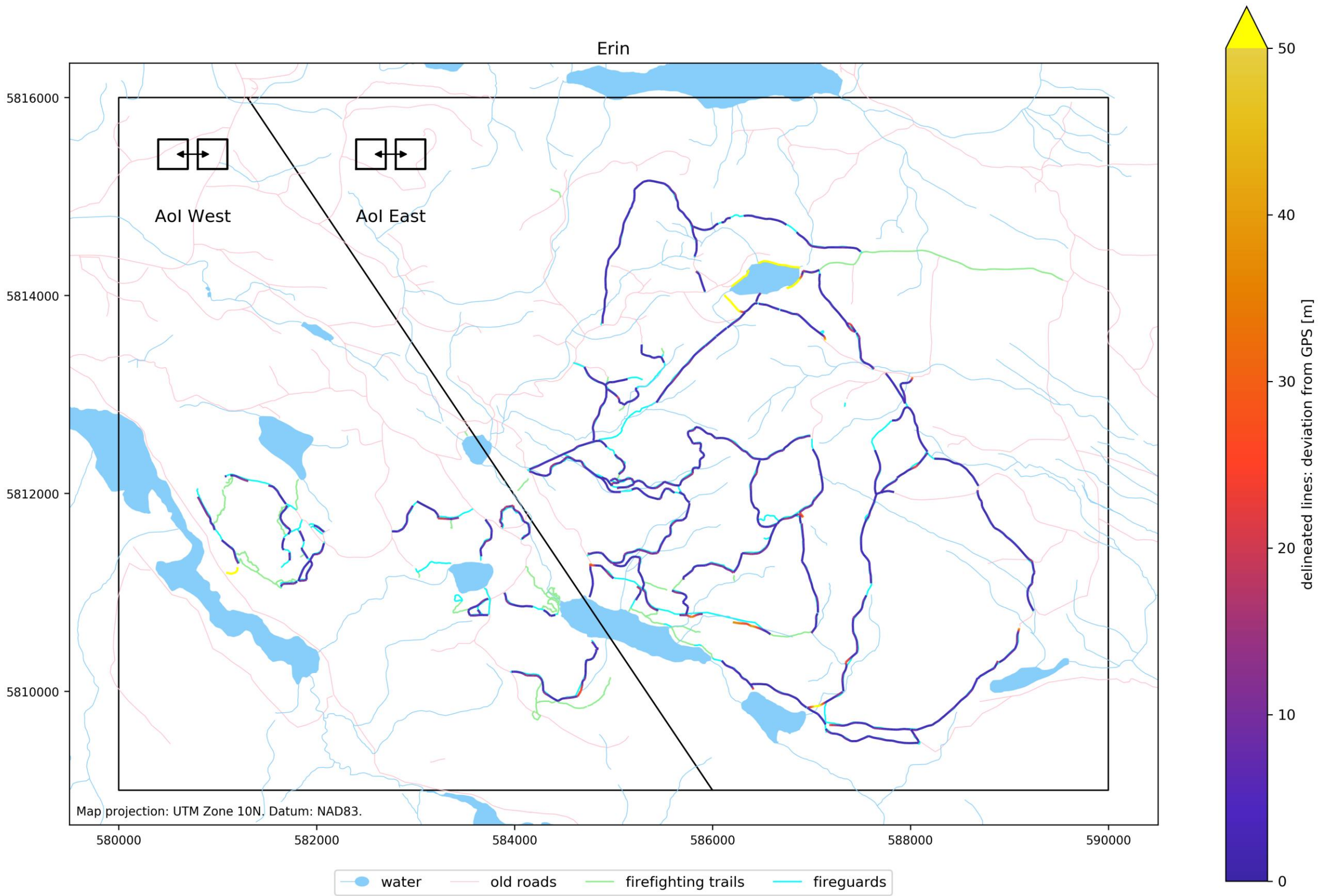


trend image:

Out of 10.2 km of delineated features, 3.8 km were firelines. That is 37.0%
 Out of 10.6 km of fireguards, 3.6 km were detected. That is 34.3%
 13.5 m average deviation from GPS derived location

step image:

Out of 32.5 km of delineated features, 22.8 km were firelines. That is 70.3%
 Out of 42.2 km of fireguards, 24.0 km were detected. That is 56.8%
 12.0 m average deviation from GPS derived location



multispectral image:

Out of 46.8 km of delineated features, 45.5 km were firelines. That is 97.2%

Out of 52.8 km of fireguards, 47.5 km were detected. That is 90.0%

5.5 m average deviation from GPS derived location

Appendix E Slope steepness data

Next page. The graphs show the fireguard detection success as a function of terrain steepness. The bars show histograms of detected fireguard length (blue) and undetected fireguards (red) by terrain steepness. The black bars show the producer's accuracy for each direction, i.e. the fraction of fireguards that were detected by each interpreter. Each bar represents the cumulative length of fireguard segments in a slope steepness bin. E.g., for AoI West, the first red bar represents the total length of missed fireguards on terrain that is no steeper than 2.5 degrees. The histograms are stratified by AoI and image interpreter.

